Neuron

Article

General anesthesia globally synchronizes activity selectively in layer 5 cortical pyramidal neurons

Graphical abstract

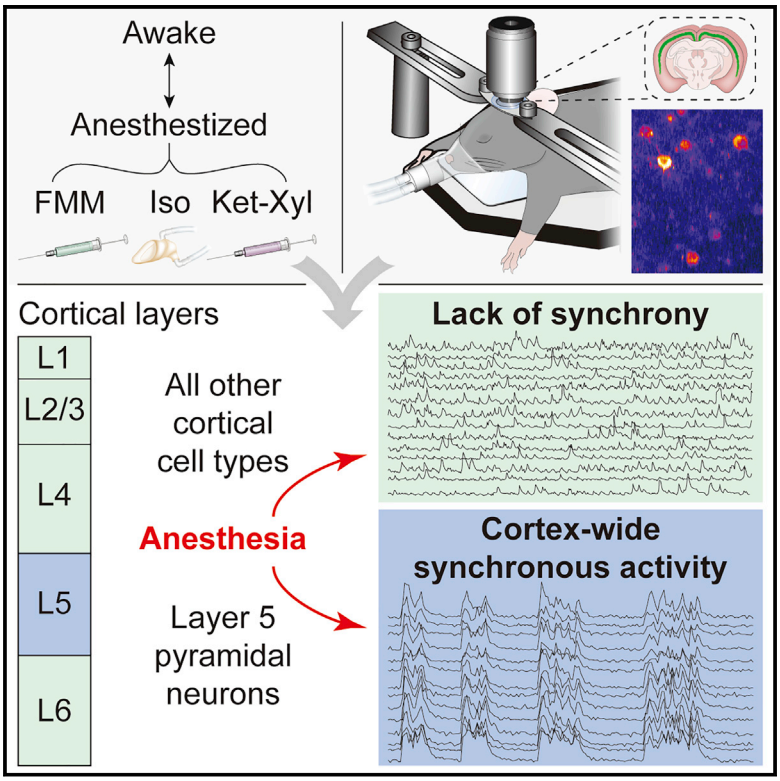

Authors

Arjun Bharioke, Martin Munz, Alexandra Brignall, ..., Karl-Klaus Conzelmann, Emilie Macé, Botond Roska

Correspondence

botond.roska@iob.ch

In brief

Bharioke, Munz et al. discovered that different general anesthetics consistently synchronize spontaneous activity of mouse layer 5 pyramidal neurons, but of no other cortical cell type, *in vivo*. Strikingly, changes in synchrony across layer 5 pyramidal neurons, during transitions to and from anesthesia, coincide with loss and recovery of consciousness.

Highlights

- Activity of layer 5 PNs synchronizes globally in different anesthetics
- Other mouse cortical cell types show no consistent increase in synchrony
- Changes in layer 5 synchrony coincide with the loss and recovery of consciousness
- Basal, but not apical, layer 5 dendrites are in synchrony with somas

Bharioke et al., 2022, Neuron *110*, 2024–2040
June 15, 2022
https://doi.org/10.1016/j.neuron.2022.03.032

CellPress

CellPress
OPEN ACCESS

Neuron

Article

General anesthesia globally synchronizes activity selectively in layer 5 cortical pyramidal neurons

Arjun Bharioke,[1,2,3,7] Martin Munz,[1,2,3,7] Alexandra Brignall,[1,2,7] Georg Kosche,[1,2,3] Max Ferdinand Eizinger,[4] Nicole Ledergerber,[1,2,3] Daniel Hillier,[1,2,3,6] Brigitte Gross-Scherf,[1,2,3] Karl-Klaus Conzelmann,[4] Emilie Macé,[5] and Botond Roska[1,2,3,8,*]

[1]Institute of Molecular and Clinical Ophthalmology Basel, Basel, Switzerland
[2]Department of Ophthalmology, University of Basel, Basel, Switzerland
[3]Friedrich Miescher Institute for Biomedical Research, Basel, Switzerland
[4]Max von Pettenkofer-Institute, Virology, Medical Faculty and Gene Center, Ludwig Maximilians University, Munich, Germany
[5]Brain-Wide Circuits for Behavior Research Group, Max Planck Institute of Neurobiology, Martinsried, Germany
[6]Institute of Cognitive Neuroscience and Psychology, Research Centre for Natural Sciences, Budapest, Hungary
[7]These authors contributed equally
[8]Lead contact
*Correspondence: botond.roska@iob.ch
https://doi.org/10.1016/j.neuron.2022.03.032

SUMMARY

General anesthetics induce loss of consciousness, a global change in behavior. However, a corresponding global change in activity in the context of defined cortical cell types has not been identified. Here, we show that spontaneous activity of mouse layer 5 pyramidal neurons, but of no other cortical cell type, becomes consistently synchronized *in vivo* by different general anesthetics. This heightened neuronal synchrony is aperiodic, present across large distances, and absent in cortical neurons presynaptic to layer 5 pyramidal neurons. During the transition to and from anesthesia, changes in synchrony in layer 5 coincide with the loss and recovery of consciousness. Activity within both apical and basal dendrites is synchronous, but only basal dendrites' activity is temporally locked to somatic activity. Given that layer 5 is a major cortical output, our results suggest that brain-wide synchrony in layer 5 pyramidal neurons may contribute to the loss of consciousness during general anesthesia.

INTRODUCTION

Conscious processing is thought to rely on activity within the cerebral cortex (Brown et al., 2019; Koch et al., 2016; Mashour et al., 2020; Tononi et al., 2016). The cortex is organized into six layers, which are composed of distinct neuronal cell types (Tasic et al., 2016). Cell types within each layer participate in cortical microcircuits (Harris and Shepherd, 2015). In the microcircuits of the sensory cortex, information flows from the thalamus (TH) into layer (L) 4, through L2/3, to the output L5 and L6. Excitatory cell types within each layer receive input from other excitatory cells in the same layer and from inhibitory cells. L1 consists of dendrites of excitatory neurons with cell bodies in L2/3–L6, long-range axons, and inhibitory neurons. Excitatory pyramidal neurons (PNs) in L5 divide into three types, differing in their outputs (Kim et al., 2015): intratelencephalic (IT) neurons provide long-range outputs to other cortical areas; pyramidal tract (PT) neurons connect to the TH and other subcortical areas; near-projecting (NP) neurons predominantly show local recurrent connectivity with other L5 PNs.

All general anesthetics induce loss of consciousness (Hudetz and Mashour, 2016; Mashour, 2014). However, their molecular modes of action vary. Comparing three common anesthetics—isoflurane (Iso), Fentanyl-Medetomidine-Midazolam (FMM), and Ketamine-Xylazine (Ket-Xyl)—Iso has been shown to bind the γ-aminobutyric acid type A receptors ($GABA_A$-Rs) (Hemmings et al., 2019) and to act on potassium channels through effects on the lipid bilayer (Pavel et al., 2020). In FMM, fentanyl acts on opioid receptors (Boas and Villiger, 1985); medetomidine is an alpha-2 adrenergic receptor agonist (Savola et al., 1986); and midazolam potentiates the $GABA_A$-R (Olkkola and Ahonen, 2008). In Ket-Xyl, ketamine is an antagonist of the N-methyl-d-aspartate (NMDA) receptor (Zorumski et al., 2016) and the hyperpolarization activated cyclic nucleotide gated potassium channel 1 (HCN1) (Chen et al., 2009), while xylazine is an agonist of the alpha-2 adrenergic receptor (Schwartz and Clark, 1998).

Despite the different molecular actions of individual general anesthetics, anesthesia-induced unconsciousness is accompanied by common changes in cortical activity. Recordings using electroencephalography (EEG), electrocorticography (ECoG), and intracortical extracellular electrodes show a shift in the power spectrum of cortical activity to lower frequencies (Hagihira, 2015; Lee et al., 2013; Murphy et al., 2011;

Purdon et al., 2015; Steriade et al., 1993). This shift is thought to be due to an increase in cortical synchrony, appears with loss of consciousness, and reverses with recovery of consciousness (Akeju et al., 2014a; Civillico and Contreras, 2012; Dasilva et al., 2021; Harvey et al., 2012; Hudetz, 2002; Lee et al., 2020; Purdon et al., 2013). Other effects on cortical neurons common to several general anesthetics include burst suppression (Akrawi et al., 1996; Clark and Rosner, 1973), fragmentation (Erchova et al., 2002; Lewis et al., 2012; Vizuete et al., 2014), decreases in activity (Bastos et al., 2021; Hudetz et al., 2009; Kajiwara et al., 2020; Redinbaugh et al., 2020), and increases in correlation with the average local activity (Aasebø et al., 2017; Lee et al., 2021). In addition to these effects, both cortico-cortical and cortico-thalamic disconnections of the resting state network have also been observed using functional magnetic resonance imaging (fMRI) during states of unconsciousness (Akeju et al., 2014b; Mashour and Hudetz, 2018; Uhrig et al., 2018).

Effects common to different general anesthetics have also been observed in specific cortical layers. During general anesthesia, neurons electrically characterized as being long-range projection neurons, including L5 and L6 neurons, show changes in activity correlated with the frequency changes observed through EEG and ECoG (Steriade et al., 1993). Multielectrode recordings within L5 and L6 display increases in low frequency power of the average local activity during anesthesia (Bastos et al., 2021). L5 neurons have reduced stimulus-evoked responses during anesthesia, both to external stimuli (Angel, 1993) and to artificial stimuli applied to their apical dendrites (Suzuki and Larkum, 2020). Additionally, L5 neurons are implicated in other altered states of consciousness: in non-REM sleep, they have increased recurrent connectivity strength and decreased inputs from L2/3 (Senzai et al., 2019), and their stimulation in the retrosplenial (RSP) cortex induces a dissociative state (Vesuna et al., 2020).

As detailed above, a wealth of knowledge has been accumulated about the effect of general anesthesia on the cortex either by recording from a single neuron or from neuronal populations using EEG, ECoG, fMRI, and intracortical electrodes. However, these methods provide limited spatial resolution within the populations of neurons or lack cell type specificity. Because different cell types have distinct functional roles in controlling information flow within cortical microcircuits, measuring the activity within individual cell types would provide insight into the neuronal correlates of the unconscious state. Additionally, information about the behavioral state of an organism can be contained within the spatiotemporal correlations of activity across neurons of the same cell type. Recordings from many neurons of a specific type across an extended area of cortex would reveal these correlations. In the context of anesthesia, this has not yet been performed.

RESULTS

Anesthetics induce neuronal synchrony in L5 PNs

To understand the effect of general anesthesia on spontaneous population activity of specific cortical cell types, we performed *in vivo* two-photon calcium imaging from neurons in the visual cortex of different mouse lines, in both awake and anesthetized states, in darkness (Figure 1A). To target L5 PNs throughout cortex, we used Rbp4-Cre KL100 mice (Gerfen et al., 2013; Gong et al., 2007) and systemically administered conditional adeno-associated virus (AAV) of PHP.eB serotype (Chan et al., 2017) expressing GCaMP7s (AAV-CAG-FLEX-GCaMP7s) (Dana et al., 2019).

To identify a common effect of general anesthesia, we compared the activity of L5 PNs at surgical anesthetic depth, induced by FMM, Iso, and Ket-Xyl (Figure 1A). In the EEG power spectrum, all three anesthetics reduced the ratio of the power between the θ (3.5–10 Hz) and δ (0.5–3 Hz) bands (θ-δ EEG ratio) (Figure 1B). L5 PNs in visual cortex showed spontaneous calcium activity in both awake and anesthetized states. While awake, the relative timing of individual calcium fluctuations, which we term events, differed between neurons (Figure 1C; Video S1). In contrast, each of the anesthetics induced a marked alignment of calcium events across neurons (Figure 1C; Video S1). To quantify the alignment, we computed the correlation of each neuron's activity with the mean population activity of all other neurons within each recording and defined this as the "neuronal synchrony." Importantly, for all three anesthetics, the neuronal synchrony was significantly higher compared with that when awake (Figure 1D). In addition, two other quantifications of the synchrony of neuronal activity—the correlation of activity between pairs of neurons and the normalized temporal variance of the mean population activity—both showed significantly higher values in anesthesia compared with those when awake, independent of the specific anesthetic used (Figure S1).

Despite the precise temporal alignment of calcium events across the neurons, inter-event intervals were variable and, therefore, between 0 and 2 Hz, recorded activity showed a range of frequencies under all three anesthetics (Figures 2A and 2B). Furthermore, the mean event frequency within this range did not show a consistent change from that when awake (Figure 2C): Iso had lower mean event frequency, whereas FMM and Ket-Xyl had higher mean event frequency. To control for the possible effect of anesthetic depth in generating this difference in event frequency, we varied the Iso concentration from 1% to 2.5%, resulting in the depth of anesthesia varying from light, through surgical, to deep. At all Iso concentrations, the mean event frequency was lower than that while awake (Figure S2). Similarly, varying the blood concentration of FMM did not result in a change in the mean event frequency (Figure S2). To understand if the presence of alpha 2 adrenergic receptor agonists in both FMM and Ket-Xyl mixtures may result in higher event frequencies, we added medetomidine prior to Iso anesthesia and found that medetomidine did not result in a significant increase in mean event frequency compared with that when awake, when administered either alone or at any of the Iso concentrations tested (Figure S2).

In addition to the change in mean event frequency, the change in mean event amplitude was also inconsistent across the three anesthetics. FMM and Iso led to higher mean event amplitudes than those when awake, whereas Ket-Xyl induced no significant difference (Figure 2D). Taken together, among different properties of neuronal activity of L5 PNs, only neuronal

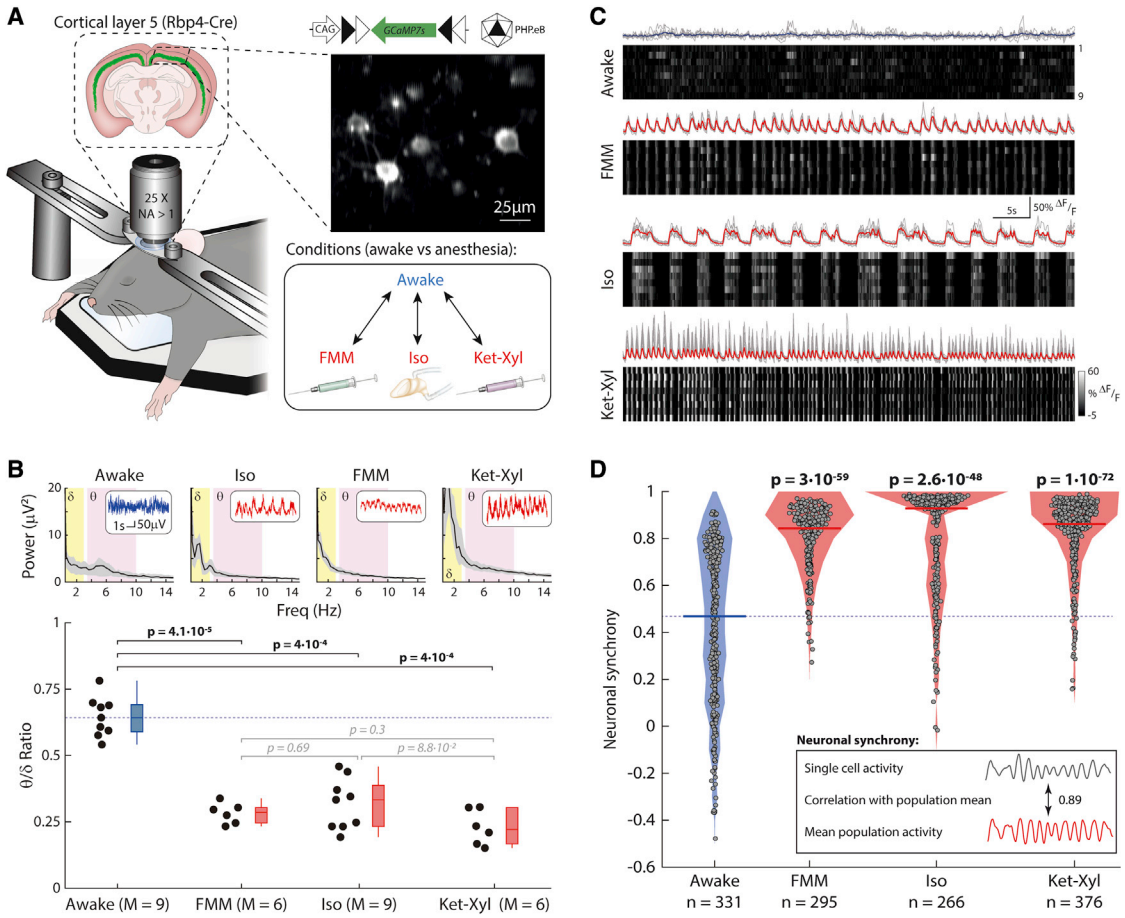

Figure 1. Synchronous activity in L5 cortical neurons during anesthesia

(A) Rbp4-Cre mice, injected with PHP.eB AAV-CAG-FLEX-GCaMP7s, imaged in darkness.

(B) Upper: EEG power spectrum. Inset: example traces. Lower: θ-δ EEG ratio across mice. Box: 25 percentile–75 percentile; whisker: 5 percentile–95 percentile; line: median; blue: awake; red: anesthetized; dashed line: awake median. Wilcoxon rank-sum ($p < 0.003$, prior to Bonferroni correction for 6 comparisons) (bold: significant; italic: not significant).

(C) Calcium activity of example neurons (upper: gray lines; lower: grayscale). Mean: blue (awake), red (anesthetized). See Video S1.

(D) Filled circles: neuronal synchrony per cell; solid line: median; shading: distribution; dashed line: awake median. Wilcoxon rank-sum ($p < 0.003$, prior to Bonferroni correction for 3 comparisons). See Figures S1 and S3. (B) M = mice. (C and D) n = cells from 9 (awake) and 8 (each anesthetic) mice. See Figure S6.

synchrony showed a consistent change across all three anesthetics.

Medetomidine decreases Iso concentration required to induce neuronal synchrony

Medetomidine is known to reduce the concentration of an anesthetic required to maintain a desired depth of anesthesia (Albrecht et al., 2014; Bekker and Sturaitis, 2005; Khan et al., 1999). Therefore, we asked if medetomidine would similarly reduce the concentration of anesthetic required to induce neuronal synchrony of L5 PNs (Figure S3). Whereas 1% Iso alone did not significantly increase neuronal synchrony compared with that when awake, 1% Iso in the presence of medetomidine resulted in a significant increase in neuronal synchrony. Additionally, whereas 1% Iso alone resulted in light anesthesia, 1% Iso together with medetomidine evoked surgical anesthesia. The combined effect of Iso and medetomidine was also reflected in the EEG spectral power, with 1% Iso together with medetomidine showing a significant decrease in EEG spectral power compared with 1% Iso or medetomidine alone. Therefore, the decrease in anesthetic concentration required to evoke a specific depth of anesthesia in the presence of medetomidine is paralleled by a similar decrease in the concentration required to evoke neuronal synchrony in L5 PNs.

Synchronization of L5 PNs coincides with loss of consciousness

We explored the relative timing of the increase in neuronal synchrony and the loss of consciousness during the induction of anesthesia in the posterior cortex within visual cortex.

To determine the timing of the transition from awake-like to anesthesia-like neuronal synchrony, we compared the

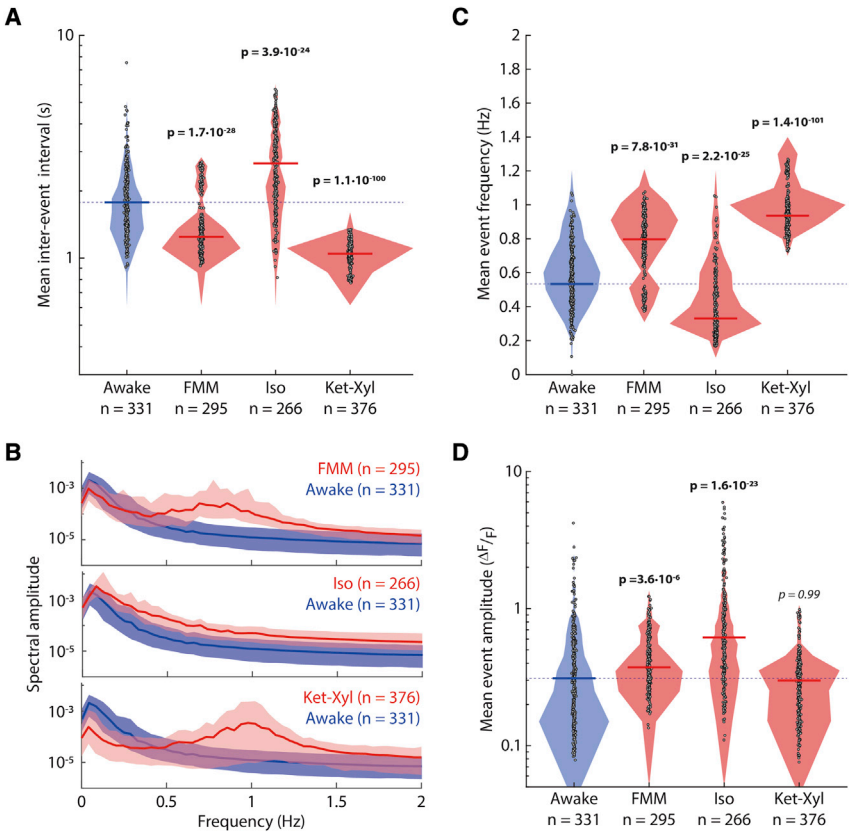

Figure 2. Mean inter-event interval, frequency, and mean event amplitude in L5 neurons

(A) Filled circles: mean of inter-event intervals per neuron; solid line: median; shading: distribution; dashed line: awake median.

(B) Amplitude of frequency spectrum. Line: median across neurons; shading: 25 percentile–75 percentile.

(C) Filled circles: mean event frequency per neuron. See Figure S2.

(D) Filled circles: mean event amplitude per neuron.

(A, C, and D) Lines and shading as in (A). Wilcoxon rank-sum ($p < 0.003$, prior to Bonferroni correction for 3 comparisons) (bold: significant; italic: not significant). (A–D) n = cells from 9 (awake) and 8 (each anesthetic) mice.

"instantaneous" distribution of neuronal synchrony every 3 s following the exposure of Rbp4-Cre mice to Iso (Figure 3A) with the previously determined steady-state distributions of neuronal synchrony in awake and anesthetized mice (data from Figure 1D). We then obtained two curves describing the probability that the median instantaneous neuronal synchrony is drawn from the awake ("awake-probability curve") or the anesthetized steady-state distributions ("anesthetized-probability curve") (Figure 3A). Following the onset of Iso, the awake-probability curve decreased, whereas the anesthetized-probability curve increased. At 82.5 ± 7.5 s, the curves crossed, and we defined this time point as the transition time from awake-like to anesthetized-like neuronal synchrony.

We then estimated the timing of the loss of consciousness in two ways. First, we measured the loss of eye, whisker, and body movements (Figure 3B). It took between 68 and 118 s for 25%–75% of mice to stop moving their eyes, whiskers, and body, following the exposure to Iso. Second, we measured instantaneous θ-δ EEG ratios in 15-s intervals (Figure 3C). To quantify the closeness of the instantaneous θ-δ EEG ratios to the previously determined steady-state θ-δ EEG ratio distributions in awake and anesthetized mice (data from Figure 1B), we used a similar procedure as described for neuronal synchrony. The resulting awake- and anesthetized-probability curves crossed at 76.5 ± 7.5 s following the onset of Iso, a time point that we defined as the transition time from awake-like to anesthesia-like EEG spectral power. Therefore, following the onset of Iso, the transition time of neuronal synchrony closely matched the transition time of EEG spectral power, with both falling within the transition period of motor behaviors (Figure 3D).

Loss of neuronal synchrony in L5 PNs coincides with recovery of consciousness

Next, we explored the relative timing of the decrease in neuronal synchrony and the recovery of consciousness following the termination of Iso anesthesia, using the same statistical procedures as for the loss of consciousness (Figure 3E). The transition time from anesthesia-like to awake-like neuronal synchrony was 39.5 ± 7.5 s. It took between 23 and 70 s for 25%–75% of mice to start to move their eyes, whiskers, and body, as well as to recover their righting reflex (Franks, 2008; Figure 3F). The transition time from anesthesia-like to awake-like θ-δ EEG ratios was 33.5 ± 7.5 s (Figure 3G). Therefore, the transition time of neuronal synchrony closely matched the transition time of EEG spectral power, with both falling within the transition period of motor behaviors, following the termination of anesthesia (Figure 3H).

Changes of neuronal synchrony in L5 PNs in anterior and posterior cortex coincide

So far, we investigated only the posterior cortex. Therefore, we compared the transition time of neuronal synchrony in the anterior and posterior cortices. Following the onset of Iso, the transition time from awake-like to anesthetized-like neuronal synchrony was 86.5 ± 7.5 s in the anterior cortex (Figure S4), compared with 82.5 ± 7.5s in the posterior cortex (Figures 3A and 3D). Following the termination of Iso, the transition time from anesthetized-like to awake-like neuronal synchrony was 41.5 ± 7.5 s in the anterior cortex, compared with 39.5 ± 7.5 s in the posterior cortex (Figures 3E, 3H, and S4). Therefore, the transition times of neuronal synchrony in L5 PNs coincide in both the anterior and posterior cortex during both the onset of and recovery from anesthesia.

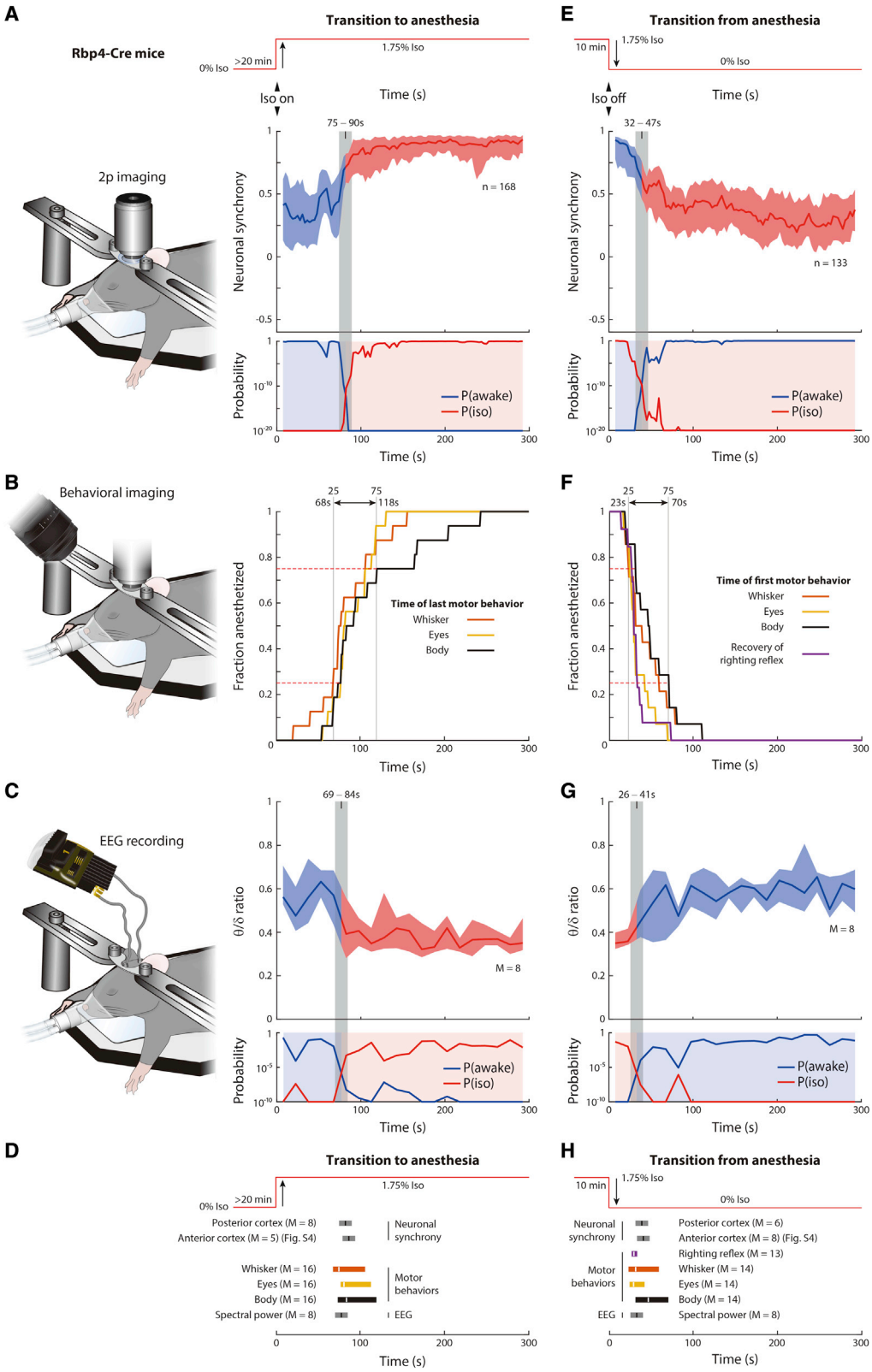

(legend on next page)

Changes of neuronal synchrony coincide with the loss of consciousness in individual mice

Following the onset of Iso anesthesia, the time point at which individual mice stopped moving was variable (Figure 3B). We asked if the transition time of neuronal synchrony correlated with the variable timing of changes in motor behavior. Defining the transition time of motor behaviors as the time at which the mouse stopped moving, as assessed by movements of its eye, whisker, and body, we found that the transition time of neuronal synchrony correlated with the transition time of motor behaviors, with a correlation coefficient of 0.89 (Figure S5). Further, the root mean squared difference between the transition times of motor behavior and neuronal synchrony was 13.7 s, which was within the precision of the transition time in neuronal synchrony alone. Finally, the transition time of neuronal synchrony was not significantly different from the transition time of motor behavior, when analyzed across individual mice by a paired test. Therefore, the transition time of neuronal synchrony closely matches the time at which individual mice stopped moving.

Heightened neuronal synchrony is specific to L5 PNs

Do anesthetics induce an increase in neuronal synchrony in other cortical cell types? To determine this, we recorded spontaneous activity in different cell types in primary visual cortex, across layers, in darkness (Figure 4A).

Neurons in L1 are primarily inhibitory (Schuman et al., 2019). Hence, we selectively imaged inhibitory neurons within the top 100 μm of cortex. Neuronal synchrony was significantly lower under FMM, was not significantly different under Iso, and was significantly higher under Ket-Xyl compared with that when awake (Figure 4B). We then imaged excitatory neurons in L2/3, L4, and L6 (Figure 4A). For all investigated cell types, neuronal synchrony was not consistently different from that when awake under all three anesthetics (Figures 4C–4E). Inhibitory interneurons are interspersed throughout cortex, and those in L1 are molecularly distinct from inhibitory interneurons in deeper layers (Schuman et al., 2019). To explore the effect of general anesthesia on neuronal synchrony in inhibitory neurons outside of L1, we imaged inhibitory neurons deeper than 100 μm. Under FMM, neuronal synchrony was not significantly greater than that while awake, unlike Iso and Ket-Xyl (Figure 4F). In addition, we compared the mean neuronal synchrony per mouse, while awake and during anesthesia, for all investigated cell types and found that L5 PNs were the only cell type to show a significantly higher neuronal synchrony in each of the anesthetics (Figure S6). Therefore, cortical excitatory neurons in L2/3, L4, L6 and cortical inhibitory neurons did not show a consistent change in neuronal synchrony during general anesthesia.

Although neuronal synchrony shows a consistent change only in L5 PNs, cell types in other layers may have subthreshold fluctuations, not detectable by GCaMP7s, that are also synchronous with the activity of L5 PNs. Because FMM did not induce an increase in neuronal synchrony in any cortical layer other than L5, when measured by GCaMP7s, we chose FMM to explore if such synchronous subthreshold fluctuations exist. We patch-clamped L2/3 PNs, while simultaneously imaging L5 PNs (Figure S7). We defined the "relative synchrony" as the correlation of the subthreshold voltage recorded in L2/3 PNs with the mean GCaMP7s activity across the recorded L5 PNs. Relative synchrony was significantly lower than the neuronal synchrony between L5 PNs (Figure S7). Therefore, the synchronous activity in L5 PNs does not simply reflect a common subthreshold fluctuation across cortical layers.

L5 PNs show greatest increase in neuronal synchrony and decreased entropy

The distributions of neuronal synchrony in the anesthetized and awake states overlap in most of the cell types we investigated. Hence, using Monte Carlo sampling, we examined the degree to which the samples obtained in awake and anesthetized conditions could originate from a single common distribution. We obtained standardized distances, measured as Z scores, for each cell type and each anesthetic. A large Z score indicates a low probability that neuronal synchrony values under a given anesthetic are drawn from the common distribution (Figure S8). The Z score for all the three anesthetics in L5 PNs was greater than the Z score for any of the anesthetics in all the other cell types investigated. In addition, through the use of Bayesian estimation (Kruschke, 2013), we modeled the observed neuronal synchrony and computed the probability distribution of the differences in the mean neuronal synchrony while anesthetized compared with those when awake. Only L5 PNs showed a consistent increase in the mean neuronal synchrony across all three anesthetics (Figure S8).

A change in neuronal synchrony could result in a change in the average information (quantified as entropy) that a population of neurons can transmit. We computed the entropy of activity within each recorded population, averaged across time. Unlike all other

Figure 3. Changes in neuronal synchrony coincide with the loss and recovery of consciousness

(A–H) Transition to (A–D) and from (E–H) anesthesia in Rbp4-Cre mice, injected with PHP.eB AAV-CAG-FLEX-GCaMP7s.

(A and E) Neuronal synchrony in posterior cortex. Upper: anesthesia protocol. Middle: neuronal synchrony in 15 s-rolling window. Lower: probability that neuronal synchrony in each window is sampled from awake (P(awake): awake-probability curve; blue line) or Iso (P(iso): anesthetized-probability curve; red line) distributions from Figure 1D. Blue shading when blue line is higher than red line; red shading when red line is higher than blue line (also applied to middle). Gray bar: crossing of P(awake) and P(iso). n = cells in 8 mice (A) and 6 mice (E). See Figure S4.

(B and F) Behavioral imaging with infrared camera. Fraction of mice remaining at each time point following induction (B) or termination (E) of Iso, as assessed by motor behaviors. Dashed lines: 25 and 75 percentiles (time marked by gray lines). Arrow marks time when 25%–75% of mice terminated (B) or initiated (F) movements. See Figure S5.

(C and G) Upper: θ-δ ratio after induction (C) or termination (G) of Iso, in 15-s windows. Lower: probability that θ-δ ratio in each window is sampled from awake (P(awake): awake-probability curve; blue line) or Iso (P(iso): anesthetized-probability curve; red line) distributions from Figure 1B. Shading color and gray bar as in (A) and (E).

(D and H) Transition times of neuronal synchrony for posterior and anterior cortex (A, E, and Figure S4), motor behaviors (B) and (F) and EEG spectral power (C) and (G). (A, E, C, and G) Line: median; shading: 25 percentile–75 percentile. (C, D, G, and H) M = mice.

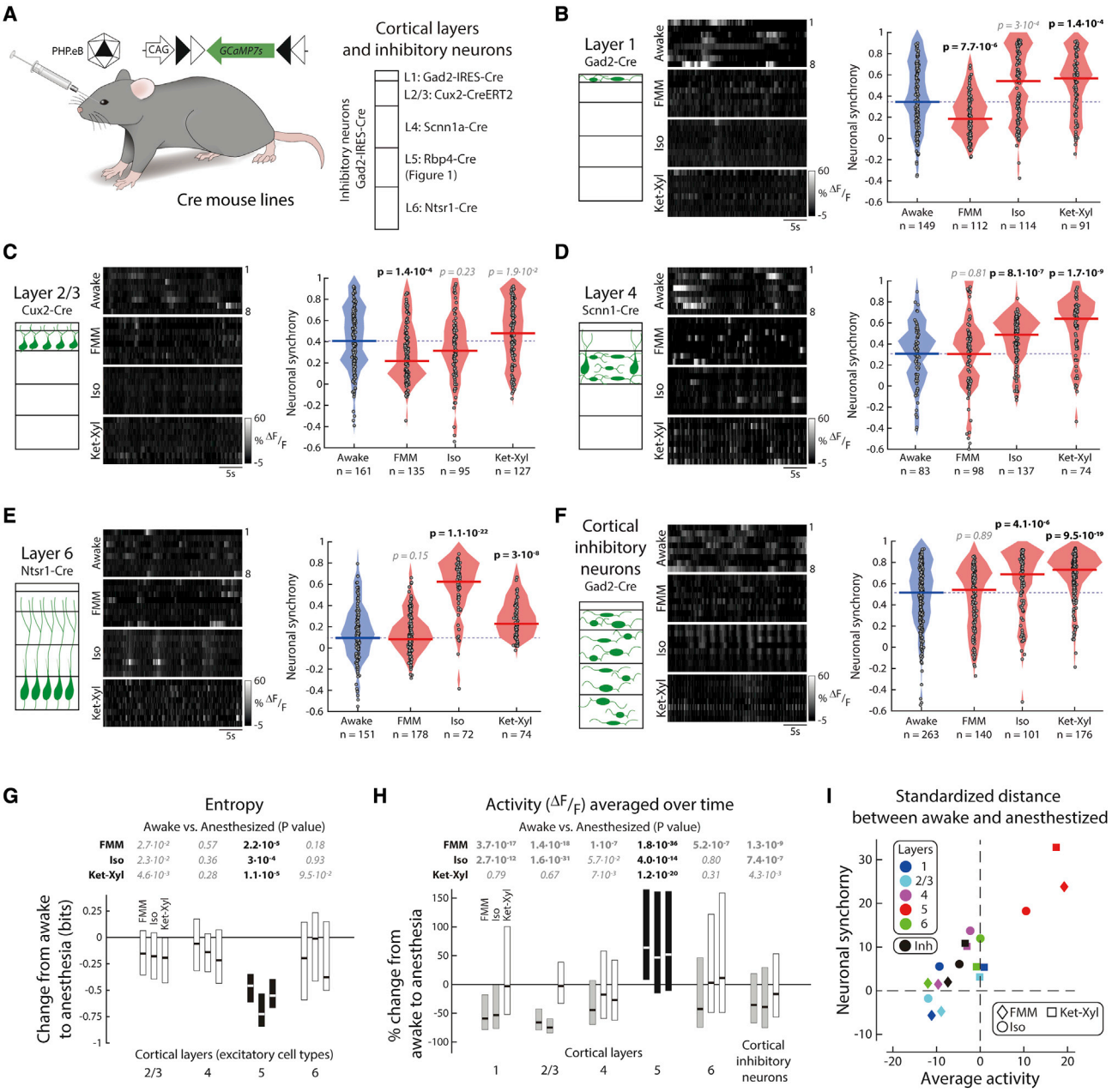

Figure 4. Neurons in cortical layers 1, 2/3, 4, and 6 and cortical inhibitory neurons do not show higher neuronal synchrony across all anesthetics

(A) Mice injected with PHP.eB AAV-CAG-FLEX-GCaMP7s were imaged in darkness.

(B–F) Left: schematic. Middle: example activity (grayscale). Right: filled circles: neuronal synchrony for each cell; solid line: median; shading: distribution; dashed line: awake median. Wilcoxon rank-sum ($p < 0.003$, prior to Bonferroni correction for 18 comparisons, to include L5). See Figure S7. (B) L1: Gad2-Cre. (C) L2/3: Cux2-Cre. (D) L4: Scnn1-Cre. (E) L6: Ntsr-Cre. (F) Cortical inhibitory neurons: Gad2-Cre.

(G) Change in mean population entropy, per unit time (L5: Figure 1D). Line: median; box: 25 percentile–75 percentile; black: significant change. See Figure S9. Wilcoxon rank-sum ($p < 0.05$, prior to Bonferroni correction for 12 comparisons) (bold: significant; italic: not significant).

(H) Change in average spontaneous activity per neuron (L5: Figure 1D). Line: median; box: 25 percentile–75 percentile; black: significant increase; gray: significant decrease. See Figure S10. Wilcoxon rank-sum ($p < 0.003$, prior to Bonferroni correction for 18 comparisons) (bold: significant; italic: not significant).

(I) Standardized distances of neuronal synchrony and average spontaneous activity between each anesthetic and awake. Standardized distances, measured from Monte Carlo samples from the combined distribution of each anesthetized condition and awake, are standard deviations above the mean (Z score). See Figure S8. (B–F) n = neurons from L1: 6 mice; L2/3: 6 mice; L4: 6 mice; L6: 5 mice (awake) and 4 mice (each anesthetic); cortical inhibitory neurons: 5 mice. See Figure S6.

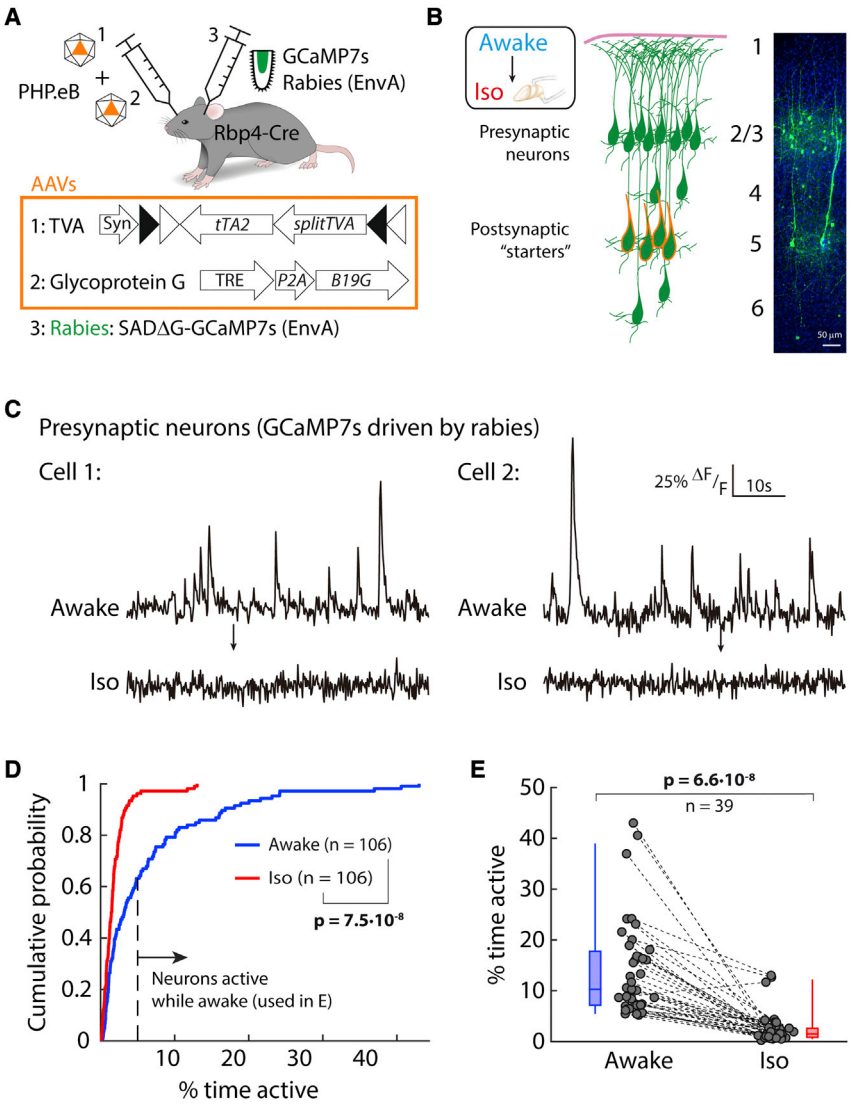

Figure 5. Cortical neurons presynaptic to L5 are silent during anesthesia

(A) Rbp4-Cre mice were infected with rabies encoding GCaMP7s through a dual AAV strategy.

(B) Schematic (left) and immunostaining (right) of GCaMP7s in L5 neurons (starters) and their presynaptic neurons within cortex.

(C) Activity of two example presynaptic neurons before and after Iso anesthesia.

(D) Cumulative probability of activity in presynaptic neurons between awake (blue) and Iso (red). Kolmogorov-Smirnov ($p < 0.003$).

(E) Change in neuronal activity (dashed lines) from awake (blue) to Iso anesthesia (red) for each neuron active >5% of time while awake (from D). Box: 25 percentile–75 percentile; whisker: 5 percentile–95 percentile; line: median. Wilcoxon signed rank ($p < 0.003$). (D and E) n = neurons in 5 mice.

excitatory cell types, L5 PNs showed a significant decrease in entropy in all three anesthetics compared with that when awake (Figure 4G). To control for a concomitant increase in entropy in the time domain, we also computed the entropy of activity in each L5 PN over time, averaged across neurons in the recorded population. On average, individual neurons under anesthesia did not show a change in entropy compared with that when awake (Figure S9); therefore, there is an overall decrease in entropy specifically within L5 PNs across the population.

Only L5 PNs have an increased activity across anesthetics

Although we did not observe a consistent change in mean event amplitude and frequency of L5 PNs (Figure 2), each anesthetic did result in either a higher amplitude or frequency. Therefore, in L5 PNs, the combination of amplitude and frequency, which is the average spontaneous activity over time, was consistently higher in all anesthetics (Figures 4H and S10). Notably, in all other cortical cell types that we investigated, the average spontaneous activity under each anesthetic was either significantly lower or not significantly different from its value while awake. Therefore, L5 PNs are not only the single cortical cell type with increased neuronal synchrony but also the single cortical cell type with increased mean spontaneous activity under general anesthesia (Figure 4I).

Cortical neurons presynaptic to L5 PNs are silent during anesthesia

The majority of cortical inputs to L5 PNs are recurrent connections from within L5 (Kim et al., 2015; Young et al., 2021). However, L5 PNs also receive input from other cortical layers. To measure the neuronal synchrony of these inputs during anesthesia, we used monosynaptically restricted and retrograde transsynaptic rabies tracing initiated from L5 PNs to drive expression of a calcium indicator in neurons directly presynaptic to these cells. We engineered and injected an envelope A-coated rabies virus expressing GCaMP7s into cortex and used a double AAV strategy (Figure 5A) to initiate the spread of rabies specifically from L5 PNs. By 7 days after infection, presynaptic neurons outside L5 expressed GCaMP7s (Figure 5B). We imaged activity of the same presynaptic neurons in both awake and Iso-anesthetized conditions (Figure 5C). Whereas these presynaptic neurons were active while awake, in paired recordings, Iso anesthesia evoked a significant decrease in their activity (Figures 5C–5E). The decrease in activity in this subpopulation of cortical neurons was so strong that the mean activity was at noise level and, hence, it was not possible to compute neuronal synchrony. This suggests that the presynaptic cortical inputs from outside L5 do not provide a direct synchronous drive into L5 PNs during anesthesia.

Activity of L5 PNs is synchronous across cortical areas

To investigate the temporal alignment of L5 PN activity during anesthesia across cortical areas, we performed widefield

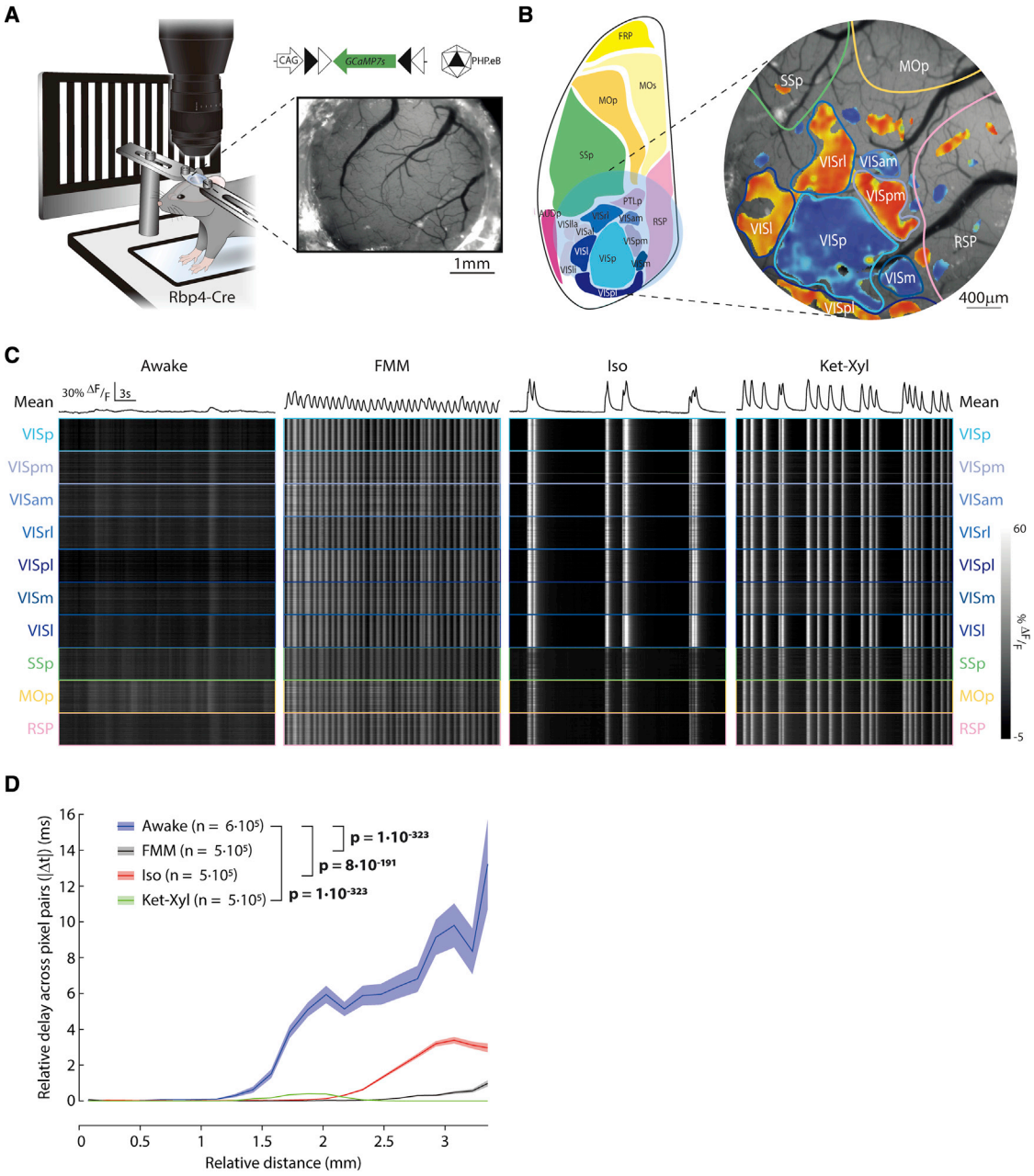

Figure 6. Synchronized activity in L5 extends across cortical areas and distances

(A) Epifluorescence imaging of Rbp4-Cre mice, injected with PHP.eB AAV-CAG-FLEX-GCaMP7s. Inset: cranial window. Visual stimulation to identify visual cortices. Spontaneous activity recorded in darkness.

(B) Left: schematic cranial window location (blue circle). Right: imaging window with visual field sign map marking visual areas (VISp: primary; VISpm: posteromedial; VISam: anteromedial; VISrl: rostrolateral; VISpl: posterolateral; VISm: medial; VISl: lateral) and estimated locations of other cortices (SSp, primary somatosensory; MOp, primary motor; RSP, retrosplenial).

(C) Spontaneous activity in darkness. Upper: mean across pixels. Lower: activity of 100 pixels within each area (grayscale). See Figure S11.

(D) Median relative delay between pixels pairs plotted against their relative distance. Shading: bootstrapped confidence interval. Wilcoxon rank-sum; n = pixel pairs from 6 mice.

fluorescence imaging of activity from a large region of posterior cortex (Figure 6A; area: 12.6 mm^2) in Rbp4-Cre mice injected with PHP.eB AAV-CAG-FLEX-GCaMP7s. We mapped the location of cortical areas in awake mice by using visual stimuli to localize the visual cortices and then, using this as a reference, aligned other adjacent cortical areas (Figure 6B). Following this, we recorded spontaneous calcium activity across the identified cortical areas in darkness.

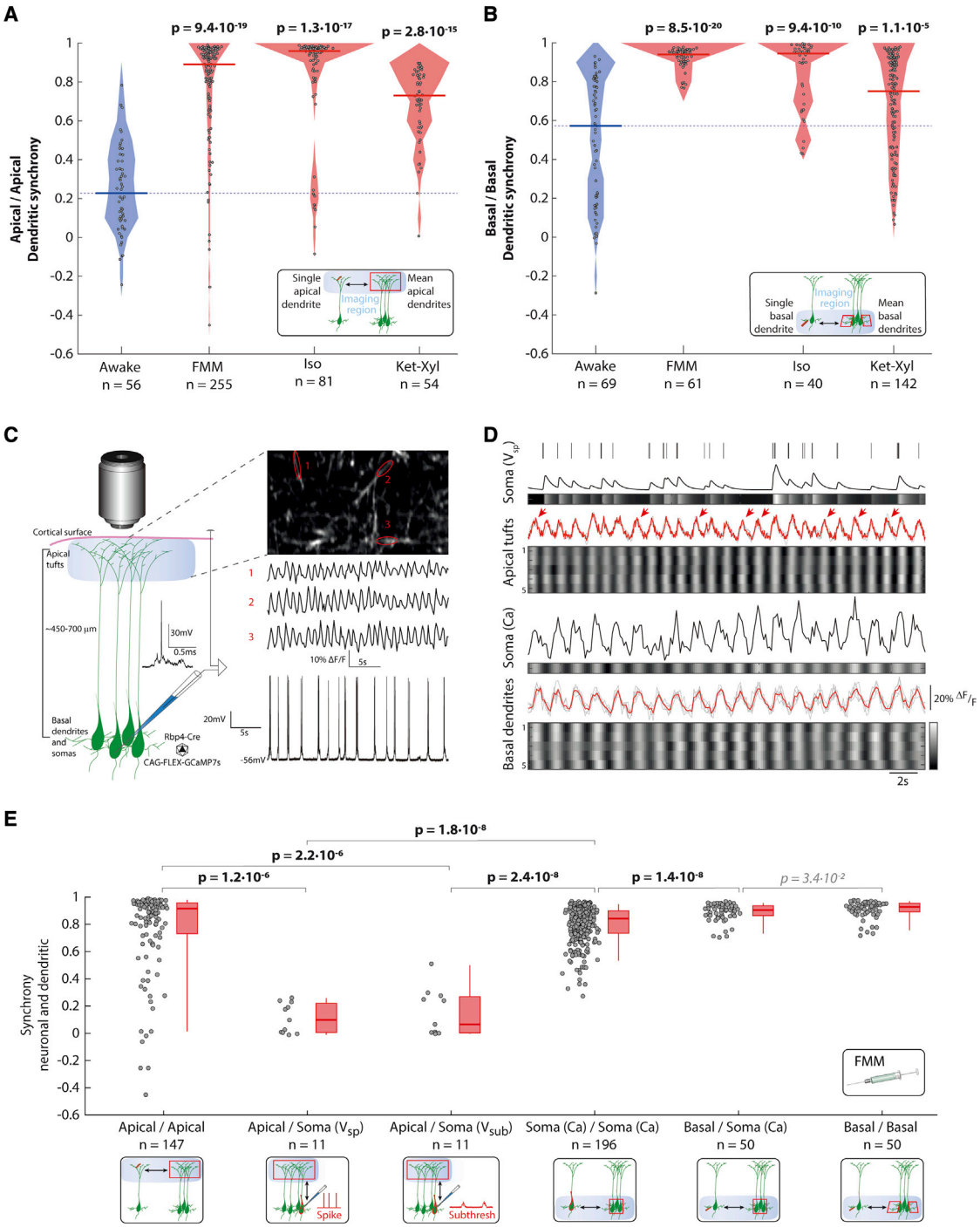

Figure 7. Dendritic synchrony matches neuronal synchrony in basal but not apical dendrites

(A and B) Rbp4-Cre mice injected with PHP.eB AAV-CAG-FLEX-GCaMP7s imaged in darkness. Filled circles: apical tuft (A) and basal dendrite (B) dendritic synchrony; solid line: median; shading: distribution; dashed line: awake median. n = regions of interest (ROIs) from 9 (awake), 8 (each anesthetic) mice.

(C) Simultaneous patch-clamp and imaging. Left: schematic with example (see Figure S12). Right, top: calcium activity from 3 ROIs. Right, bottom: voltage recording.

(D) Simultaneous soma and dendritic recordings. Upper: apical tuft. Lower: basal dendrites. Soma (V_{sp}): somatic spiking and predicted calcium trace (by convolution) (line and grayscale). Apical tufts: ROIs' activity (gray lines, grayscale) with mean (red). Arrows: unaligned calcium events. Soma (Ca): soma activity (line, grayscale). Basal dendrites: ROIs' activity (gray lines, grayscale) with mean (red). Grayscale activity individually scaled from min (black) to max (white).

(legend continued on next page)

Under all the three general anesthetics, spontaneous calcium events were synchronized across multiple cortical areas (Figure 6C). To quantify this synchrony, we computed the cross-correlation of mean activity for all pairs of cortical areas within the imaging window, including visual, somatosensory, motor, and association areas. We defined the relative delay in the activity of each pair of areas as the absolute value of the time lag of the peak cross-correlation. While awake, all the non-visual cortical areas showed delays greater than or equal to 300 ms with at least one of the other areas. In contrast, under FMM, Iso, and Ket-Xyl, every pair of cortical areas showed delays less than or equal to the imaging resolution (100 ms), even when comparing between sensory, motor, and association areas (Figure S11). Therefore, general anesthesia results in the synchronization of activity in L5 PNs across a wide range of cortical areas.

Next, we explored synchrony in L5 PNs across distance, independent of cortical areas. We defined relative delays between pairs of pixels analogously to delays between areas using the pixelwise activity. While awake, there was a progressive increase in the relative delays over distance. In contrast, delays were significantly lower under all three anesthetics (Figure 6D). Taken together, these results suggest that anesthesia-evoked synchronous activity in L5 PNs is independent of both cortical areas and distance.

Basal, but not apical, dendrites are in synchrony with somas

L5 PNs have apical dendrites that extend toward the cortical surface and divide into apical tufts in L1 and basal dendrites that extend within L5. We asked if spontaneous activity within the apical tufts or basal dendrites during anesthesia is synchronized across their own populations. We used *in vivo* two-photon calcium imaging to record spontaneous activity in darkness separately from populations of apical tufts and basal dendrites of L5 PNs in visual cortex while awake and under all three anesthetics. Both apical tufts and basal dendrites showed higher "dendritic synchrony" (defined analogously to neuronal synchrony) within their own populations under all three anesthetics compared with that when awake (Figures 7A and 7B).

We then asked if spontaneous activity within apical tufts or basal dendrites is synchronized relative to the somatic activity. To record from apical tufts and somas simultaneously, we performed *in vivo* two-photon imaging of apical tufts in L1 together with targeted patch-clamp recordings from somas in L5 using FMM anesthesia (Figures 7C and S12). To record from basal dendrites and somas, we simultaneously imaged both compartments using two-photon imaging within L5. We observed a subset of calcium events within the apical tufts that was not synchronous with activity in the soma (Figure 7D). In contrast, calcium events in the basal dendrites were synchronous with calcium events in the soma. To quantify the similarity of the activity in different compartments, we defined the "relative synchrony" between dendrites and somas analogously to the neuronal synchrony. The relative synchrony of the apical tufts with somatic spiking was significantly lower than both the dendritic synchrony among apical tufts and the neuronal synchrony across the somatic population (Figure 7E). Furthermore, the relative synchrony of apical tufts with the subthreshold voltage within the soma was also significantly lower than both the dendritic synchrony among apical tufts and the neuronal synchrony across the somatic population. In contrast to the apical tufts, relative synchrony between the basal dendrites and somas was not significantly different from the dendritic synchrony within basal dendrites. Hence, during FMM anesthesia, the activity between the apical tufts of L5 PNs and their somas showed low relative synchrony, but the activity between L5 PNs' basal dendrites and their somas showed high relative synchrony.

Next, we measured the mean frequency of events across each compartment under all three anesthetics. We reasoned that if the mean event frequency differed between compartments, events in both compartments could not be synchronous. Basal dendrites showed no significant difference in their mean event frequency from the somas under all three anesthetics (Figure S13). However, the apical tufts showed a higher mean event frequency than the somas under FMM, no significant difference from the somas in Iso, and a lower mean event frequency than the somas under Ket-Xyl.

L5 PNs have synchronous output activity

PNs within L5 divide into subpopulations with different efference patterns, including neurons that project locally, those that project to subcortical areas, and those that project to other cortical areas. Do these output channels send spikes during anesthesia? Using targeted *in vivo* patch-clamp recordings from the soma of cortical PNs, we measured the average number of action potentials per subthreshold fluctuation of the membrane voltage (Figure S14). Under FMM anesthesia, L5 PNs showed an average of 1.1 spikes per subthreshold fluctuation. As a comparison, L2/3 excitatory neurons showed an average of 0.015 spikes per subthreshold fluctuation. Additionally, using targeted *in vivo* juxtacellular recordings from the soma of individual L5 PNs, we recorded spontaneous bursts of action potentials during FMM anesthesia in darkness (Figure S12). Thus, L5 PNs send bursts of action potentials during anesthesia.

To understand which brain regions receive synchronous activity, we recorded activity from the IT and PT subpopulations of L5 PNs within the visual cortices in darkness (Figure 8A). Both IT and PT neurons showed consistently higher neuronal synchrony under all three anesthetics, compared with that when awake (Figures 8B, 8C, and S15). Therefore, during anesthesia, L5 PNs send synchronous output locally to subcortical areas, including the TH, and to distant cortical areas.

DISCUSSION

The cortex is composed of distinct cell types that are arranged in different layers. Anesthesia leads to major changes in cortical

(E) Synchrony under FMM (red line: median; box: 25 percentile–75 percentile; whisker 5 percentile–95 percentile). See Figure S13; Soma: V_{sp}: predicted calcium trace (by convolution); V_{sub}: subthreshold membrane voltage; Ca: calcium imaging (Figure 1D); n = ROIs (calcium imaging) or recordings (patch clamp and juxtacellular). Imaging of somas in 9 (awake) and 8 (each anesthetic) mice; dendrites in 5 mice; electrophysiology from 5 neurons in 3 mice. (A, B, and E) Wilcoxon rank-sum ($p < 0.003$, prior to Bonferroni correction for 6 comparisons) (bold: significant; italic: not significant).

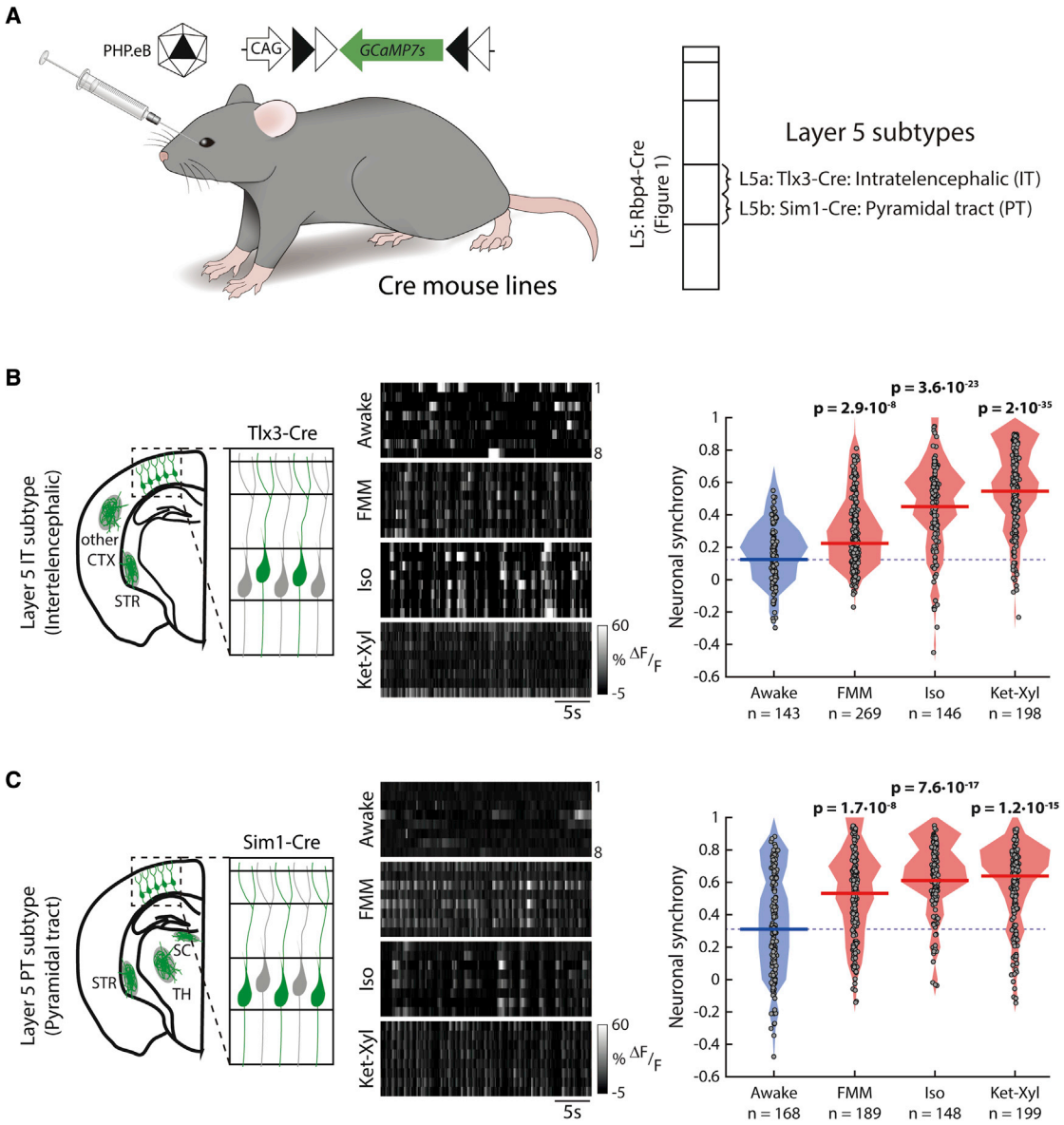

Figure 8. Output subtypes of L5 PNs show increased neuronal synchrony

(A) Mice, injected with PHP.eB AAV-CAG-FLEX-GCaMP7s, were imaged in darkness. See Figure S14.

(B and C) Left: schematic neurons and projections patterns (green) (CTX, cortex; STR, striatum; SC, superior colliculus; TH, thalamus). Middle: example activity (grayscale). Right: filled circles: neuronal synchrony of each neuron; solid line: median; shading: distribution; dashed line: awake median. Wilcoxon rank-sum ($p < 0.003$, prior to Bonferroni correction for 9 comparisons, to include Rbp4-Cre) (bold: significant). See Figure S15. n = neurons in 6 Tlx3-Cre (B), 5 Sim1-Cre (C) mice.

activity, yet these changes have not been investigated at the resolution of defined cell types. Consequently, the spatiotemporal distribution of activity within a cell type, which determines the neuronal information carried by that cell type, is also unknown during anesthesia. Hence, we set out to identify the effect of different anesthetics with regard to spontaneous activity within neurons of a given type. We found two striking effects common to all anesthetics. First, only PNs of L5, and no other cortical cell type, consistently showed synchronous activity in all three anesthetics across different locations both within and across cortical areas. Second, the higher neuronal synchrony in L5 PNs was accompanied by higher spontaneous activity compared with that when awake. In contrast, other cortical cell types as well as neurons providing out-of-layer input to L5 PNs showed either no change or decreased spontaneous activity during anesthesia.

Frequency analysis of EEG recordings previously revealed a shift toward low frequency oscillations that correlates with unconsciousness. This shift is thought to be a result of synchronization of activity across populations of neurons. Our results confirm that all the three anesthetics show an increase in

amplitude within the 0–2-Hz band. However, within this band, individual anesthetics have distinct frequency distributions. Given that calcium indicators allow the measurement of activity across neuronal populations of defined cell types, we characterized the synchrony by calculating the precise temporal alignment of the spontaneous activity between individual neurons in cortical cell types. We quantified temporal synchrony through the correlation between pairs of neurons (Lissek et al., 2016), the correlation of a single neuron with the remaining population, and the temporal variability of activity within the population. All the three measures revealed consistently higher synchrony in L5 PNs (Figures 1D and S1). Because our aim was to compute the temporal synchrony of individual neurons within a cell type, the most relevant measure was neuronal synchrony, which is the correlation of the activity of individual neurons with the remaining population. Directly measuring neuronal synchrony allows the periodic and aperiodic alignment of activity in a neuronal population to be distinguished, up to the imaging rate and the sensitivity of GCaMP7s, which may not detect every spike. In contrast, any temporal alignment of activity can only be indirectly estimated via frequency analysis (Donoghue et al., 2020). Indeed, we observed that the common feature of spontaneous activity under different anesthetics was not a consistent change in event frequency but instead an aperiodic temporal alignment of activity of L5 PNs.

The amount of activity in cortical neurons during altered states of consciousness has been studied extensively. Although some studies report a decrease in cortical activity, others report an increase in spontaneous activity in some cells, as well as a specific increase in bursting activity across the deep layers of cortex (Bastos et al., 2021; Redinbaugh et al., 2020; Senzai et al., 2019). Here, we characterize the change in activity specific to individual cortical cell types, as measured with GCaMP7s. During anesthesia compared with that when awake, we reported that spontaneous activity in the visual cortex, measured in darkness, increased in L5 PNs (Figure 4H). In contrast, in all other cortical layers, depending on the specific anesthetic, we observed either no change or a decrease in spontaneous activity compared with that when awake (Figure S10).

Synchronous periods of silence, termed synchronous fragmentation, have been observed in cortex during anesthesia. If activity in neurons is synchronous, then the periods of absence of activity are also necessarily synchronous. The converse, however, is not necessarily true. The absence of activity in all neurons during specific intervals does not imply that all the neurons must then fire synchronously outside of those intervals, which we observed in L5 PNs. Given the observation of structured periods of quiescence, such as synchronous fragmentation and burst suppression, as well as the overall reduction of activity during general anesthesia, it had been proposed that a temporally precise increase of activity of inhibitory neurons is involved in generating the recorded phenomena described above (Brown et al., 2011). However, we found that the average activity in L5 PNs increases during general anesthesia in all three anesthetics (Figures 4H and S10). In addition, we found that inhibitory neurons, both in L1, as well as more generally, when combined across the depth of cortex below L1, do not show consistently higher neuronal synchrony across the three anesthetics. This suggests that temporally precise inhibitory inputs, across the entire depth of cortex, may not be necessary for heightened synchronous firing across L5 PNs during general anesthesia. However, we cannot exclude a possible role for specific subgroups of interneurons within individual layers or specific interneuron cell types in regulating the neuronal synchrony within L5 PNs.

L5 PNs have strong recurrent connectivity, and several of our results suggest that recurrent activity within L5 PNs may be sufficient to explain the synchronous events within L5 PNs during anesthesia. First, our patch-clamp recordings of L5 PNs show that the synchronous spontaneous calcium activity in individual neurons represents actual firing (Figures 7C, S12, and S14). Second, within L5 PNs, we observe neuronal synchrony within the L5 IT subpopulation (Figure 8B), whose axons provide long-range intracortical efference to other L5 PNs. Third, the TH as a whole is unlikely to provide a synchronous drive to sensory cortices because we show that L4 neurons in visual cortex, which receive most of the thalamic input into cortex, do not synchronize their activity across anesthetics (Figure 4D). Fourth, we show that the out-of-layer neurons directly presynaptic to L5 PNs show reduced activity (Figures 5D, 5E, and S14), suggesting that the neuronal synchrony within L5 PNs is not inherited from an out-of-layer presynaptic cortical population. Therefore, during anesthesia, activity within L5 PNs contains the necessary components to provide an internal drive for synchronous activity across the L5 PN population, including the long-range synchrony across cortical areas and distance (Figures 6C and 6D).

Within L5, both PT and IT subtypes show significantly higher neuronal synchrony during general anesthesia (Figures 8B and 8C). When all three subtypes of L5 PNs are labeled, as in the Rbp4-Cre line, neuronal synchrony is even further increased (Figure S15). This suggests that the greatest increase in neuronal synchrony is found within the third, NP subtype of L5 PNs, which receive local input and provide local output. We suggest the following model for the relative differences in neuronal synchrony among the three L5 subtypes: NP neurons connect to other NP neurons more strongly than to IT and PT neurons. In contrast, IT and PT neurons send outputs preferentially to distant areas. Hypothesizing that general anesthetics induce bursting of all L5 PNs, this connectivity would result in the bursts aligning more within NP neurons as opposed to IT and PT neurons, and therefore, greater neuronal synchrony within the NP subtype.

A common feature of general anesthetics is the disruption of consciousness, and different theories of consciousness assign different roles to distinct cortical connections. One view is that communication in cortico-cortical loops between distinct cortical regions underlies the generation of conscious perception (Mashour et al., 2020; Tononi et al., 2016). Others regard thalamocortical loops as crucial in the maintenance of consciousness (Alkire et al., 2008; Aru et al., 2019; Llinás et al., 1998). Electrical stimulation of both the frontal cortex (Pal et al., 2018) and the central TH (Bastos et al., 2021; Redinbaugh et al., 2020) have each been shown to be capable of reversing anesthesia, resulting in a partial recovery of consciousness. We observe that the changes in neuronal synchrony within L5 PNs, which contribute to cortico-cortical and cortico-thalamic connections, closely match the timing of features, such as EEG and various motor behaviors, associated with the loss and

recovery of consciousness (Figures 3D and 3H). Furthermore, the timing of behavioral changes and the change in neuronal synchrony are correlated across individual mice (Figure S5). Additionally, although a light dose of anesthetic does not result in increased neuronal synchrony, adding an adjuvant of anesthesia, such as medetomidine, to that dose results in an increase in neuronal synchrony and a concomitant increase in the depth of anesthesia from light depth to surgical depth (Figure S3). Hence, our work is consistent with a role for synchronous activity of L5 PNs in regulating the loss of consciousness. However, our work does not directly establish a causal link between neuronal synchrony within L5 PNs and the loss of consciousness, which should prove a productive future direction of exploration.

Synchronous activity in L5 PNs can disrupt the information transmitted between the cortex and TH in cortico-thalamic loops. Indeed, our measurements specifically within the PT subpopulation of L5 PNs, that send outputs from cortex to TH, demonstrate heightened neuronal synchrony within this subtype, across all three anesthetics (Figure 8C). An additional mechanism for the disconnection of these loops is the decoupling of apical tufts from the soma within L5 PNs during anesthesia. Previously, this disconnection has been reported for stimulation of the apical dendrites in a subset of general anesthetics, including Iso and Ket (Suzuki and Larkum, 2020). In our work, in the presence of FMM, we observed a reduction in the relative synchrony between apical tufts and the soma for spontaneous activity (Figure 7E), which is consistent with tuft-to-soma decoupling. Additionally, for both FMM and Ket-Xyl, we observed that the apical dendrites have different event frequencies compared with those of the soma (Figure S13). Hence, in L5 PNs, the decoupling of apical dendrites from the soma extends to spontaneous activity during anesthesia. In contrast, we found that basal dendrites show an increased relative synchrony with the soma. This suggests that basal dendrites are coupled to the soma during general anesthesia. Thalamic inputs enter L5 PNs through both basal and apical dendrites (Harris and Shepherd, 2015). Therefore, whereas decoupling of the apical dendrites from the soma of L5 PNs could disrupt cortico-thalamic information entering through axonal connections within L1, synchronous activity within L5 PNs would decrease all information within cortico-thalamic loops, as well as possibly driving TH into a state of activity specific to anesthesia.

Theories about conscious perception that rely on cortico-cortical communication emphasize the role of different cortical areas. Some assign an important role for information transfer between cortical areas along the anterior-posterior axis, whereas others have focused on information transfer between associative and sensory cortices. We have primarily recorded from neurons in the posterior half of the brain. In widefield recordings, we demonstrated synchrony with minimal delay across L5 PNs across an area of posterior cortex encompassing sensory cortices, motor cortices, and the RSP cortex, which is a higher order association cortex (Figure 6). In contrast, it has previously been shown that a reduced dose of ketamine, which results in a dissociative yet conscious state, leads to synchrony only in RSP cortex (Vesuna et al., 2020). Therefore, the fraction of posterior cortex with synchronous L5 PN activity appears to be correlated with the degree to which consciousness is maintained. Although our results focus on the posterior cortex, we did show that the transition time of neuronal synchrony during both the loss and recovery of consciousness in anterior cortex closely matches the corresponding transition times in posterior cortex, suggesting that the anesthesia-induced synchronization of activity in L5 PNs occurs throughout cortex. Subcortical areas were also shown to be involved in generating or maintaining anesthesia-induced behavioral changes either because general anesthesia induces a wide range of effects on an organism beyond the disruption of consciousness, including decreases in alertness, muscle tone, heart rate, and respiration rate or because these areas are also involved in the generation or maintenance of consciousness(Alkire et al., 2007; Gao et al., 2019; Jiang-Xie et al., 2019; Muindi et al., 2016; Solt et al., 2014). The relative role of cortical and subcortical areas in generating unconsciousness calls for further exploration.

In this study, we have focused on identifying features of cortical activity in individual cortical cell types that are common across different general anesthetics. However, each anesthetic induced a distinct combination of changes in synchrony and overall activity across cortical cell types. For example, in L4 PNs, FMM led to a decrease in activity but no change in neuronal synchrony, whereas Iso and Ket-Xyl resulted in an increase in neuronal synchrony with no associated change in activity. Therefore, different anesthetics show varied effects on the examined cortical cell types, with the exception of the increase in synchrony and activity within L5 PNs.

Many models have suggested that anesthesia results in the global disconnection of cortex from the rest of the brain (Hudetz and Mashour, 2016; Koch et al., 2016; Schroeder et al., 2016; Wenzel et al., 2019). Our results show synchronization of L5 PNs across brain areas during which these neurons act effectively as a single unit. Therefore, the anesthesia-induced disconnection of cortex may not be due to a transition from a state of cortical activity during wakefulness to one of inactivity during anesthesia. Instead, our results suggest that during general anesthesia, the cortex may shift from a mode characterized by spatially asynchronous L5 outputs, which carry a high amount of information, to a mode characterized by highly active, but spatially synchronous L5 outputs, with low information content.

STAR★METHODS

Detailed methods are provided in the online version of this paper and include the following:

- KEY RESOURCES TABLE
- RESOURCE AVAILABILITY
  - Lead contact
  - Materials availability
  - Data and code availability
- EXPERIMENTAL MODEL AND SUBJECT DETAILS
  - Animals
- METHOD DETAILS
  - Adeno-associated viruses (AAVs)
  - Rabies virus production
  - Immunohistochemistry
  - Cortical layer targeting
  - Cranial window implantation

- Two-photon in vivo calcium imaging
- Rabies infection of Rbp4-Cre neurons
- Steady-state anesthesia during experiments
- Loss and recovery of consciousness

- QUANTIFICATION AND STATISTICAL ANALYSIS
  - Filtering of calcium traces
  - EEG analysis
  - Widefield image analysis
  - Filtering of voltage traces
  - Correlation analyses
  - Computing event-based statistics
  - Analysis of mean activity
  - Computing entropy
  - Statistical analyses

SUPPLEMENTAL INFORMATION

Supplemental information can be found online at https://doi.org/10.1016/j.neuron.2022.03.032.

ACKNOWLEDGMENTS

We thank N. Verma, F. Franke, C. Cameron, P. King, M. Cattaneo, D. Jothimani, and M. de Gennaro for comments; C. Cepko for the pHGT1-Adeno1 plasmid; the Complex Viruses Platform for AAV production; and V. Juvin (SciArtWork) for graphics. We acknowledge EMBO (ALTF 1552-2015; Marie Curie Action) and HFSP fellowships (LT000447/2016) to M.M., NKFIH (FK18 No:129120) and MTA (Lendület) to D.H., DFG (118803580-SFB 870 Z1) grant to K.-K.C., SNSF Synergia (CRSII3_141801), SNSF (31003A_182523), SNSF NCCR "Molecular Systems Engineering", ERC Advanced (RETMUS, N°669157, HURET N°883781) grants, and Louis-Jeantet Foundation and Koerber Foundation awards to B.R.

AUTHOR CONTRIBUTIONS

Conceptualization, A. Bharioke, M.M., and A. Brignall; methodology, A. Bharioke and M.M.; investigation: A. Bharioke, M.M., and G.K.; data curation, A. Bharioke, M.M., A. Brignall, and E.M.; formal analysis, A. Bharioke and M.M.; resources, M.F.E., N.L., D.H., B.G.-S., and K.-K.C.; software, A. Bharioke and E.M.; supervision, B.R.; writing, A. Bharioke, M.M., A. Brignall, and B.R.

DECLARATION OF INTERESTS

The authors declare no competing interests.

Received: November 9, 2020
Revised: October 30, 2021
Accepted: March 28, 2022
Published: April 21, 2022

REFERENCES

Aasebø, I.E.J., Lepperød, M.E., Stavrinou, M., Nøkkevangen, S., Einevoll, G., Hafting, T., and Fyhn, M. (2017). Temporal processing in the visual cortex of the awake and anesthetized rat. eNeuro *4*, 1–26.

Adams, S., and Pacharinsak, C. (2015). Mouse anesthesia and analgesia. Curr. Protoc. Mouse Biol. *5*, 51–63.

Akeju, O., Loggia, M.L., Catana, C., Pavone, K.J., Vazquez, R., Rhee, J., Contreras Ramirez, V., Chonde, D.B., Izquierdo-Garcia, D., Arabasz, G., et al. (2014b). Disruption of thalamic functional connectivity is a neural correlate of dexmedetomidine-induced unconsciousness. Elife *3*, e04499.

Akeju, O., Westover, M.B., Pavone, K.J., Sampson, A.L., Hartnack, K.E., Brown, E.N., and Purdon, P.L. (2014a). Effects of sevoflurane and propofol on frontal electroencephalogram power and coherence. Anesthesiology *121*, 990–998.

Akrawi, W.P., Drummond, J.C., Kalkman, C.J., and Patel, P.M. (1996). A comparison of the electrophysiologic characteristics of EEG burst-suppression as produced by isoflurane, thiopental, etomidate, and propofol. J. Neurosurg. Anesthesiol. *8*, 40–46.

Albrecht, M., Henke, J., Tacke, S., Markert, M., and Guth, B. (2014). Effects of isoflurane, ketamine-xylazine and a combination of medetomidine, midazolam and fentanyl on physiological variables continuously measured by telemetry in Wistar rats. BMC Vet. Res. *10*, 198.

Alkire, M.T., Hudetz, A.G., and Tononi, G. (2008). Consciousness and anesthesia. Science *322*, 876–880.

Alkire, M.T., McReynolds, J.R., Hahn, E.L., and Trivedi, A.N. (2007). Thalamic microinjection of nicotine reverses sevoflurane-induced loss of righting reflex in the rat. Anesthesiology *107*, 264–272.

Angel, A. (1993). Central neuronal pathways and the process of anaesthesia. Br. J. Anaesth. *71*, 148–163.

Aru, J., Suzuki, M., Rutiku, R., Larkum, M.E., and Bachmann, T. (2019). Coupling the state and contents of consciousness. Front. Syst. Neurosci. *13*, 43.

Bastos, A.M., Donoghue, J.A., Brincat, S.L., Mahnke, M., Yanar, J., Correa, J., Waite, A.S., Lundqvist, M., Roy, J., Brown, E.N., and Miller, E.K. (2021). Neural effects of propofol-induced unconsciousness and its reversal using thalamic stimulation. Elife *10*, e60824.

Bekker, A., and Sturaitis, M.K. (2005). Dexmedetomidine for neurological surgery. Neurosurgery *57*, 1–10, discussion 1–10.

Boas, R.A., and Villiger, J.W. (1985). Clinical actions of fentanyl and buprenorphine: the significance of receptor binding. Br. J. Anaesth. *57*, 192–196.

Brown, E.N., Purdon, P.L., and Van Dort, C.J. (2011). General Anesthesia and altered states of arousal: a systems neuroscience analysis. Annu. Rev. Neurosci. *34*, 601–628.

Brown, R., Lau, H., and LeDoux, J.E. (2019). Understanding the higher-order approach to consciousness. Trends Cogn. Sci. *23*, 754–768.

Buchholz, U.J., Finke, S., and Conzelmann, K.K. (1999). Generation of bovine respiratory syncytial virus (BRSV) from cDNA: BRSV NS2 is not essential for virus replication in tissue culture, and the human RSV leader region acts as a functional BRSV genome promoter. J. Virol. *73*, 251–259.

Chan, K.Y., Jang, M.J., Yoo, B.B., Greenbaum, A., Ravi, N., Wu, W.-L., Sánchez-Guardado, L., Lois, C., Mazmanian, S.K., Deverman, B.E., and Gradinaru, V. (2017). Engineered AAVs for efficient noninvasive gene delivery to the central and peripheral nervous systems. Nat. Neurosci. *20*, 1172–1179.

Chen, X., Shu, S., and Bayliss, D.A. (2009). HCN1 channel subunits are a molecular substrate for hypnotic actions of ketamine. J. Neurosci. *29*, 600–609.

Civillico, E.F., and Contreras, D. (2012). Spatiotemporal properties of sensory responses *in vivo* are strongly dependent on network context. Front. Syst. Neurosci. *6*, 25.

Clark, D.L., and Rosner, B.S. (1973). Neurophysiologic effects of general anesthetics. I. The electroencephalogram and sensory evoked responses in man. Anesthesiology *38*, 564–582.

Dana, H., Sun, Y., Mohar, B., Hulse, B.K., Kerlin, A.M., Hasseman, J.P., Tsegaye, G., Tsang, A., Wong, A., Patel, R., et al. (2019). High-performance calcium sensors for imaging activity in neuronal populations and microcompartments. Nat. Methods *16*, 649–657.

Danneman, P.J., Suckow, M.A., and Brayton, C. (2012). The Laboratory Mouse, Second Edition (CRC Press).

Dasilva, M., Camassa, A., Navarro-Guzman, A., Pazienti, A., Perez-Mendez, L., Zamora-López, G., Mattia, M., and Sanchez-Vives, M.V. (2021). Modulation of cortical slow oscillations and complexity across anesthesia levels. NeuroImage *224*, 117415.

Donoghue, T., Haller, M., Peterson, E.J., Varma, P., Sebastian, P., Gao, R., Noto, T., Lara, A.H., Wallis, J.D., Knight, R.T., et al. (2020). Parameterizing

neural power spectra into periodic and aperiodic components. Nat. Neurosci. *23*, 1655–1665.

Erchova, I.A., Lebedev, M.A., and Diamond, M.E. (2002). Somatosensory cortical neuronal population activity across states of anaesthesia. Eur. J. Neurosci. *15*, 744–752.

Ewald, A.J., Werb, Z., and Egeblad, M. (2011). Monitoring of vital signs for long-term survival of mice under anesthesia. Cold Spring Harb. Protoc. *2011*, pdb.prot5563.

Finke, S., Mueller-Waldeck, R., and Conzelmann, K.-K. (2003). Rabies virus matrix protein regulates the balance of virus transcription and replication. J. Gen. Virol. *84*, 1613–1621.

Fleischmann, T., Jirkof, P., Henke, J., Arras, M., and Cesarovic, N. (2016). Injection anaesthesia with fentanyl-midazolam-medetomidine in adult female mice: importance of antagonization and perioperative care. Lab Anim. *50*, 264–274.

Franco, S.J., Gil-Sanz, C., Martinez-Garay, I., Espinosa, A., Harkins-Perry, S.R., Ramos, C., and Müller, U. (2012). Fate-restricted neural progenitors in the mammalian cerebral cortex. Science *337*, 746–749.

Franks, N.P. (2008). General anaesthesia: from molecular targets to neuronal pathways of sleep and arousal. Nat. Rev. Neurosci. *9*, 370–386.

Fulcher, B.D., Murray, J.D., Zerbi, V., and Wang, X.-J. (2019). Multimodal gradients across mouse cortex. Proc. Natl. Acad. Sci. USA *116*, 4689–4695.

Gao, S., Proekt, A., Renier, N., Calderon, D.P., and Pfaff, D.W. (2019). Activating an anterior nucleus gigantocellularis subpopulation triggers emergence from pharmacologically-induced coma in rodents. Nat. Commun. *10*, 2897.

Garrett, M.E., Nauhaus, I., Marshel, J.H., and Callaway, E.M. (2014). Topography and areal organization of mouse visual cortex. J. Neurosci. *34*, 12587–12600.

Gerfen, C.R., Paletzki, R., and Heintz, N. (2013). GENSAT BAC Cre-recombinase driver lines to study the functional organization of cerebral cortical and basal ganglia circuits. Neuron *80*, 1368–1383.

Ghanem, A., Kern, A., and Conzelmann, K.-K. (2012). Significantly improved rescue of rabies virus from cDNA plasmids. Eur. J. Cell Biol. *91*, 10–16.

Golomb, D., and Rinzel, J. (1994). Clustering in globally coupled inhibitory neurons. Phys. Nonlinear Phenom. *72*, 259–282.

Gong, S., Doughty, M., Harbaugh, C.R., Cummins, A., Hatten, M.E., Heintz, N., and Gerfen, C.R. (2007). Targeting Cre recombinase to specific neuron populations with bacterial artificial chromosome constructs. J. Neurosci. *27*, 9817–9823.

Haberl, M.G., Viana da Silva, S., Guest, J.M., Ginger, M., Ghanem, A., Mulle, C., Oberlaender, M., Conzelmann, K.-K., and Frick, A. (2015). An anterograde rabies virus vector for high-resolution large-scale reconstruction of 3D neuron morphology. Brain Struct. Funct. *220*, 1369–1379.

Hagihira, S. (2015). Changes in the electroencephalogram during anaesthesia and their physiological basis. Br. J. Anaesth. *115*, i27–i31.

Harris, K.D., and Shepherd, G.M.G. (2015). The neocortical circuit: themes and variations. Nat. Neurosci. *18*, 170–181.

Harvey, M., Lau, D., Civillico, E., Rudy, B., and Contreras, D. (2012). Impaired long-range synchronization of gamma oscillations in the neocortex of a mouse lacking Kv3.2 potassium channels. J. Neurophysiol. *108*, 827–833.

Hemmings, H.C., Riegelhaupt, P.M., Kelz, M.B., Solt, K., Eckenhoff, R.G., Orser, B.A., and Goldstein, P.A. (2019). Towards a comprehensive understanding of anesthetic mechanisms of action: a decade of discovery. Trends Pharmacol. Sci. *40*, 464–481.

Holtmaat, A., Bonhoeffer, T., Chow, D.K., Chuckowree, J., De Paola, V., Hofer, S.B., Hübener, M., Keck, T., Knott, G., Lee, W.-C., et al. (2009). Long-term, high-resolution imaging in the mouse neocortex through a chronic cranial window. Nat. Protoc. *4*, 1128–1144.

Hudetz, A.G. (2002). Effect of volatile anesthetics on interhemispheric EEG cross-approximate entropy in the rat. Brain Res. *954*, 123–131.

Hudetz, A.G., and Mashour, G.A. (2016). Disconnecting consciousness: is there a common anesthetic end-point? Anesth. Analg. *123*, 1228–1240.

Hudetz, A.G., Vizuete, J.A., and Imas, O.A. (2009). Desflurane selectively suppresses long-latency cortical neuronal response to flash in the rat. Anesthesiology *111*, 231–239.

Jiang-Xie, L.-F., Yin, L., Zhao, S., Prevosto, V., Han, B.-X., Dzirasa, K., and Wang, F. (2019). A common neuroendocrine substrate for diverse general anesthetics and sleep. Neuron *102*, 1053–1065.e4.

Jüttner, J., Szabo, A., Gross-Scherf, B., Morikawa, R.K., Rompani, S.B., Hantz, P., Szikra, T., Esposti, F., Cowan, C.S., Bharioke, A., et al. (2019). Targeting neuronal and glial cell types with synthetic promoter AAVs in mice, non-human primates and humans. Nat. Neurosci. *22*, 1345–1356.

Kajiwara, M., Kato, R., Oi, Y., and Kobayashi, M. (2020). Propofol decreases spike firing frequency with an increase in spike synchronization in the cerebral cortex. J. Pharmacol. Sci. *142*, 83–92.

Kalatsky, V.A., and Stryker, M.P. (2003). New paradigm for optical imaging: temporally encoded maps of intrinsic signal. Neuron *38*, 529–545.

Khan, Z.P., Munday, I.T., Jones, R.M., Thornton, C., Mant, T.G., and Amin, D. (1999). Effects of dexmedetomidine on isoflurane requirements in healthy volunteers. 1: Pharmacodynamic and pharmacokinetic interactions. Br. J. Anaesth. *83*, 372–380.

Kim, E.J., Juavinett, A.L., Kyubwa, E.M., Jacobs, M.W., and Callaway, E.M. (2015). Three types of cortical Layer 5 neurons that differ in brain-wide connectivity and function. Neuron *88*, 1253–1267.

Koch, C., Massimini, M., Boly, M., and Tononi, G. (2016). Neural correlates of consciousness: progress and problems. Nat. Rev. Neurosci. *17*, 307–321.

Kohtoh, S., Taguchi, Y., Matsumoto, N., Wada, M., Huang, Z.-L., and Urade, Y. (2008). Algorithm for sleep scoring in experimental animals based on fast Fourier transform power spectrum analysis of the electroencephalogram. Sleep Biol. Rhythms *6*, 163–171.

Kruschke, J.K. (2013). Bayesian estimation supersedes the t test. J. Exp. Psychol. Gen. *142*, 573–603.

Lavin, T.K., Jin, L., Lea, N.E., and Wickersham, I.R. (2020). Monosynaptic tracing success depends critically on helper virus concentrations. Front. Synaptic Neurosci. *12*, 6.

Lee, H., Tanabe, S., Wang, S., and Hudetz, A.G. (2021). Differential effect of anesthesia on visual cortex neurons with diverse population coupling. Neuroscience *458*, 108–119.

Lee, H., Wang, S., and Hudetz, A.G. (2020). State-dependent cortical unit activity reflects dynamic brain state transitions in anesthesia. J. Neurosci. *40*, 9440–9454.

Lee, U., Ku, S., Noh, G., Baek, S., Choi, B., and Mashour, G.A. (2013). Disruption of frontal-parietal communication by ketamine, propofol, and sevoflurane. Anesthesiology *118*, 1264–1275.

Lein, E.S., Hawrylycz, M.J., Ao, N., Ayres, M., Bensinger, A., Bernard, A., Boe, A.F., Boguski, M.S., Brockway, K.S., Byrnes, E.J., et al. (2007). Genome-wide atlas of gene expression in the adult mouse brain. Nature *445*, 168–176.

Lewis, L.D., Weiner, V.S., Mukamel, E.A., Donoghue, J.A., Eskandar, E.N., Madsen, J.R., Anderson, W.S., Hochberg, L.R., Cash, S.S., Brown, E.N., and Purdon, P.L. (2012). Rapid fragmentation of neuronal networks at the onset of propofol-induced unconsciousness. Proc. Natl. Acad. Sci. USA *109*, E3377–E3386.

Lissek, T., Obenhaus, H.A., Ditzel, D.A.W., Nagai, T., Miyawaki, A., Sprengel, R., and Hasan, M.T. (2016). General anesthetic conditions induce network synchrony and disrupt sensory processing in the cortex. Front. Cell. Neurosci. *10*, 64.

Liu, K., Kim, J., Kim, D.W., Zhang, Y.S., Bao, H., Denaxa, M., Lim, S.-A., Kim, E., Liu, C., Wickersham, I.R., et al. (2017). Lhx6-positive GABA-releasing neurons of the zona incerta promote sleep. Nature *548*, 582–587.

Llinás, R., Ribary, U., Contreras, D., and Pedroarena, C. (1998). The neuronal basis for consciousness. Philos. Trans. R. Soc. Lond. B Biol. Sci. *353*, 1841–1849.

Madisen, L., Garner, A.R., Shimaoka, D., Chuong, A.S., Klapoetke, N.C., Li, L., van der Bourg, A., Niino, Y., Egolf, L., Monetti, C., et al. (2015). Transgenic mice for intersectional targeting of neural sensors and effectors with high specificity and performance. Neuron *85*, 942–958.

Madisen, L., Zwingman, T.A., Sunkin, S.M., Oh, S.W., Zariwala, H.A., Gu, H., Ng, L.L., Palmiter, R.D., Hawrylycz, M.J., Jones, A.R., et al. (2010). A robust and high-throughput Cre reporting and characterization system for the whole mouse brain. Nat. Neurosci. *13*, 133–140.

Marshel, J.H., Garrett, M.E., Nauhaus, I., and Callaway, E.M. (2011). Functional specialization of seven mouse visual cortical areas. Neuron *72*, 1040–1054.

Mashour, G.A. (2014). Top-down mechanisms of anesthetic-induced unconsciousness. Front. Syst. Neurosci. *8*, 115.

Mashour, G.A., and Hudetz, A.G. (2018). Neural correlates of unconsciousness in large-scale brain networks. Trends Neurosci. *41*, 150–160.

Mashour, G.A., Roelfsema, P., Changeux, J.-P., and Dehaene, S. (2020). Conscious processing and the global neuronal workspace hypothesis. Neuron *105*, 776–798.

Muindi, F., Kenny, J.D., Taylor, N.E., Solt, K., Wilson, M.A., Brown, E.N., and Van Dort, C.J. (2016). Electrical stimulation of the parabrachial nucleus induces reanimation from isoflurane general anesthesia. Behav. Brain Res. *306*, 20–25.

Murphy, M., Bruno, M.-A., Riedner, B.A., Boveroux, P., Noirhomme, Q., Landsness, E.C., Brichant, J.-F., Phillips, C., Massimini, M., Laureys, S., et al. (2011). Propofol anesthesia and sleep: a high-density EEG study. Sleep *34*, 283-91A.

Olkkola, K.T., and Ahonen, J. (2008). Midazolam and other benzodiazepines. In Modern Anesthetics, J. Schüttler and H. Schwilden, eds. (Springer), pp. 335–360.

Osakada, F., Mori, T., Cetin, A.H., Marshel, J.H., Virgen, B., and Callaway, E.M. (2011). New rabies virus variants for monitoring and manipulating activity and gene expression in defined neural circuits. Neuron *71*, 617–631.

Pal, D., Dean, J.G., Liu, T., Li, D., Watson, C.J., Hudetz, A.G., and Mashour, G.A. (2018). Differential role of prefrontal and parietal cortices in controlling level of consciousness. Curr. Biol. *28*, 2145–2152.e5.

Pavel, M.A., Petersen, E.N., Wang, H., Lerner, R.A., and Hansen, S.B. (2020). Studies on the mechanism of general anesthesia. Proc. Natl. Acad. Sci. USA *117*, 13757–13766.

Peirce, J., Gray, J.R., Simpson, S., MacAskill, M., Höchenberger, R., Sogo, H., Kastman, E., and Lindeløv, J.K. (2019). PsychoPy2: Experiments in behavior made easy. Behav. Res. Methods *51*, 195–203.

Pnevmatikakis, E.A., and Giovannucci, A. (2017). NoRMCorre: an online algorithm for piecewise rigid motion correction of calcium imaging data. J. Neurosci. Methods *291*, 83–94.

Purdon, P.L., Pierce, E.T., Mukamel, E.A., Prerau, M.J., Walsh, J.L., Wong, K.F.K., Salazar-Gomez, A.F., Harrell, P.G., Sampson, A.L., Cimenser, A., et al. (2013). Electroencephalogram signatures of loss and recovery of consciousness from propofol. Proc. Natl. Acad. Sci. USA *110*, E1142–E1151.

Purdon, P.L., Sampson, A., Pavone, K.J., and Brown, E.N. (2015). Clinical electroencephalography for anesthesiologists part I: background and basic signatures. Anesthesiology *123*, 937–960.

Redinbaugh, M.J., Phillips, J.M., Kambi, N.A., Mohanta, S., Andryk, S., Dooley, G.L., Afrasiabi, M., Raz, A., and Saalmann, Y.B. (2020). Thalamus modulates consciousness via layer-specific control of cortex. Neuron *106*, 66–75.e12.

Savola, J.-M., Ruskoaho, H., Puurunen, J., Salonen, J.S., and Kärki, N.T. (1986). Evidence for medetomidine as a selective and potent agonist α2-adrenoreceptors. J. Auton. Pharmacol. *6*, 275–284.

Schroeder, K.E., Irwin, Z.T., Gaidica, M., Nicole Bentley, J.N., Patil, P.G., Mashour, G.A., and Chestek, C.A. (2016). Disruption of corticocortical information transfer during ketamine anesthesia in the primate brain. NeuroImage *134*, 459–465.

Schuman, B., Machold, R.P., Hashikawa, Y., Fuzik, J., Fishell, G.J., and Rudy, B. (2019). Four unique interneuron populations reside in neocortical Layer 1. J. Neurosci. *39*, 125–139.

Schwartz, D.D., and Clark, T.P. (1998). Affinity of detomidine, medetomidine and xylazine for alpha-2 adrenergic receptor subtypes. J. Vet. Pharmacol. Ther. *21*, 107–111.

Senzai, Y., Fernandez-Ruiz, A., and Buzsáki, G. (2019). Layer-specific physiological features and interlaminar interactions in the primary visual cortex of the mouse. Neuron *101*, 500–513.e5.

Solt, K., Van Dort, C.J., Chemali, J.J., Taylor, N.E., Kenny, J.D., and Brown, E.N. (2014). Electrical stimulation of the ventral tegmental area induces reanimation from general anesthesia. Anesthesiology *121*, 311–319.

Steriade, M., Nuñez, A., and Amzica, F. (1993). A novel slow (< 1 Hz) oscillation of neocortical neurons *in vivo*: depolarizing and hyperpolarizing components. J. Neurosci. *13*, 3252–3265.

Suzuki, M., and Larkum, M.E. (2020). General Anesthesia decouples cortical pyramidal neurons. Cell *180*, 666–676.e13.

Taniguchi, H., He, M., Wu, P., Kim, S., Paik, R., Sugino, K., Kvitsiani, D., Fu, Y., Lu, J., Lin, Y., et al. (2011). A resource of Cre driver lines for genetic targeting of GABAergic neurons in cerebral cortex. Neuron *71*, 995–1013.

Tasic, B., Menon, V., Nguyen, T.N., Kim, T.K., Jarsky, T., Yao, Z., Levi, B., Gray, L.T., Sorensen, S.A., Dolbeare, T., et al. (2016). Adult mouse cortical cell taxonomy revealed by single cell transcriptomics. Nat. Neurosci. *19*, 335–346.

Tiscornia, G., Singer, O., and Verma, I.M. (2006). Production and purification of lentiviral vectors. Nat. Protoc. *1*, 241–245.

Tononi, G., Boly, M., Massimini, M., and Koch, C. (2016). Integrated information theory: from consciousness to its physical substrate. Nat. Rev. Neurosci. *17*, 450–461.

Uhrig, L., Sitt, J.D., Jacob, A., Tasserie, J., Barttfeld, P., Dupont, M., Dehaene, S., and Jarraya, B. (2018). Resting-state dynamics as a cortical signature of anesthesia in monkeys. Anesthesiology *129*, 942–958.

Vesuna, S., Kauvar, I.V., Richman, E., Gore, F., Oskotsky, T., Sava-Segal, C., Luo, L., Malenka, R.C., Henderson, J.M., Nuyujukian, P., et al. (2020). Deep posteromedial cortical rhythm in dissociation. Nature *586*, 87–94.

Vizuete, J.A., Pillay, S., Ropella, K.M., and Hudetz, A.G. (2014). Graded defragmentation of cortical neuronal firing during recovery of consciousness in rats. Neuroscience *275*, 340–351.

Wenzel, M., Han, S., Smith, E.H., Hoel, E., Greger, B., House, P.A., and Yuste, R. (2019). Reduced repertoire of cortical microstates and neuronal ensembles in medically induced loss of consciousness. Cell Syst. *8*, 467–474.e4.

Wickersham, I.R., Lyon, D.C., Barnard, R.J.O., Mori, T., Finke, S., Conzelmann, K.-K., Young, J.A.T., and Callaway, E.M. (2007). Monosynaptic restriction of transsynaptic tracing from single, genetically targeted neurons. Neuron *53*, 639–647.

Xu, Q., Ming, Z., Dart, A.M., and Du, X.-J. (2007). Optimizing dosage of ketamine and xylazine in murine echocardiography. Clin. Exp. Pharmacol. Physiol. *34*, 499–507.

Yardeni, T., Eckhaus, M., Morris, H.D., Huizing, M., and Hoogstraten-Miller, S. (2011). Retro-orbital injections in mice. Lab Anim. *40*, 155–160.

Young, H., Belbut, B., Baeta, M., and Petreanu, L. (2021). Laminar-specific cortico-cortical loops in mouse visual cortex. Elife *10*, e59551.

Zhuang, J., Ng, L., Williams, D., Valley, M., Li, Y., Garrett, M., and Waters, J. (2017). An extended retinotopic map of mouse cortex. Elife *6*, e18372.

Zorumski, C.F., Izumi, Y., and Mennerick, S. (2016). Ketamine: NMDA receptors and beyond. J. Neurosci. *36*, 11158–11164.

STAR★METHODS

KEY RESOURCES TABLE

REAGENT or RESOURCE	SOURCE	IDENTIFIER
Antibodies		
Rat monoclonal anti-GFP	Nacalai	Cat # 04404-84; RRID: AB_2313654
Alexa Fluor 488 donkey anti-rabbit IgG	Thermo Fisher Scientific	Cat #: A-21206; RRID: AB_141708
Bacterial and virus strains		
PHP.eB AAV-CAG-FLEX-GCaMP7s	This paper	N/A
PHP.eB AAV-syn-FLEX-splitTVA-EGFP-tTA	This paper	N/A
PHP.eB AAV-TREtight-mTagBFP2-B19G	This paper	N/A
EnvA-SADΔG-GCaMP7s rabies virus	This paper	N/A
Chemicals, peptides, and recombinant proteins		
Tamoxifen citrate pellets	Kliba Nafag	3302.PX.V20
Fentanyl	Janssen	N/A
Medetomidine	Virbac AG	QN05CM91
Midazolam	Sintetica	N/A
Ketamine	Pfizer AG	1076850
Xylazine	Bayer	N/A
Isoflurane (Attane)	Provet AG	QN01AB06
Experimental models: Cell lines		
BSR T7/5	Buchholz et al., 1999	N/A
BHK-MG-on	Ghanem et al., 2012	N/A
BHK-EnvA	Wickersham et al., 2007	N/A
BHK-21	ATCC	CCL-10
HEK293T	ATCC	CRL-3216
HEK293T-TVA	Osakada et al., 2011	N/A
Experimental models: Organisms/strains		
Gad2-IRES-Cre mice	Jackson Labs	010802
Cux2-CreERT2 mice	MMRRC	032779-MU
Scnn1a-Tg3-Cre mice	Jackson Labs	009613
Rbp4-Cre KL100 mice	MMRRC	031125-UCD
Tlx3-Cre PL56 mice	MMRRC	041158-UCD
Sim1-Cre KJ18 mice	Gerfen et al., 2013	N/A
Ntsr1-Cre GN220 mice	MMRRC	030648-UCD
Wildtype (C57BL/6) mice	Charles River	000664
Recombinant DNA		
pGP-AAV-CAG-FLEX-jGCaMP7s-WPRE	Dana et al., 2019	Addgene #104495
pGP-AAV-syn-FLEX-splitTVA-EGFP-tTA	Liu et al., 2017	Addgene #100798
pGP-AAV-TREtight-mTagBFP2-B19G	Liu et al., 2017	Addgene #100799
pHHSC-SADΔG-mCherry	Haberl et al., 2015	N/A
pHHSC-SADΔG-jGCaMP7s	This paper	N/A
pTIT-SAD G	Finke et al., 2003	N/A
AAV serotype: PHP.eB	Chan et al., 2017	N/A
pHGTI-Adeno1	Laboratory of Constance Cepko	N/A

(*Continued on next page*)

Continued

REAGENT or RESOURCE	SOURCE	IDENTIFIER
Software and algorithms		
NoRMCorre	Pnevmatikakis and Giovannucci, 2017	https://github.com/flatironinstitute/NoRMCorre
Matlab Toolbox for Bayesian Estimation	Kruschke, 2013	https://github.com/NilsWinter/matlab-bayesian-estimation
Matlab R2020a	Mathworks	RRID: SCR_001622
Downloader Utility	Evolocus LLC	V2.02
PsychoPy	Peirce et al., 2019	https://www.psychopy.org/
Abfload	Matlab Central File Exchange	https://www.mathworks.com/matlabcentral/fileexchange/22114-fcollman-abfload
Custom code (Matlab) to analyze data	This paper	https://doi.org/10.5281/zenodo.6371706
Other		
Micro-fine+ Insulin syringes (30 gauge)	BD	324825
Datex Ohmeda Isotec 5 continuous flow vaporizer	Groppler Medizintechnik	N/A
MouseSTAT Jr with Paw Sensor (Pulse oximeter)	Kent Scientific	N/A
IR camera	Imaging source	DMK 22BUC03
Galvo-galvo scanning two photon microscope	Femtonics	N/A
FemtoSMART resonant-galvo scanning microscope	Femtonics	N/A
Nikon 25X water immersion objective (1.1 NA)	Nikon	N/A
Olympus 16X water immersion objective (0.8 NA)	Olympus	N/A
Stereotactic micromanipulator	Narishige	SM-15R
Microinjector	Narishige	IM-9B
Neurologger 2A	Evolocus LLC	N/A
Teflon-coated silver wire	World Precision Instruments	AGT0510
M0.6 x 0.8 screws	US Micro Screw	N/A
ORCA-Flash4.0 V3 CMOS camera	Hamamatsu	N/A
Epifluorescence microscope	Olympus	SZX16
Widefield light source	Olympus	U-HGLGPS
Multiclamp amplifier	Molecular Devices	700B

RESOURCE AVAILABILITY

Lead contact

Further information and requests for resources and reagents should be directed to and will be fulfilled by the lead contact, Botond Roska (botond.roska@iob.ch).

Materials availability

All unique reagents generated in this study are available from the lead contact with a completed Materials Transfer Agreement.

Data and code availability

All data reported in this paper will be shared by the lead contact upon request.

Custom code has been deposited at Zenodo and is publicly available as of the date of publication. The DOI is listed in the key resources table.

Any additional information required to reanalyze the data reported in this paper is available from the lead contact upon request.

EXPERIMENTAL MODEL AND SUBJECT DETAILS

Animals

Animal experiments were performed in accordance with standard ethical guidelines (European Communities Guidelines on the Care and Use of Laboratory Animals, 86/609/EEC) and were approved by the Veterinary Department of the Canton of Basel-Stadt. Wildtype mice and the following transgenic mouse lines were used: Gad2-IRES-Cre mice (Taniguchi et al., 2011), Cux2-CreERT2 (Franco et al., 2012), Scnn1a-Tg3-Cre (Madisen et al., 2010), Rbp4-Cre KL100 (Gerfen et al., 2013; Gong et al., 2007), Tlx3-Cre

PL56 (Gerfen et al., 2013), Sim1-Cre KJ18 (Gerfen et al., 2013), and Ntsr1-Cre GN220 (Gong et al., 2007). All mice were of C57BL/6 background, both male and female, from 35 days to 7 months old, and maintained on a normal 12-hour light/dark cycle, and group-housed where possible in a pathogen-free environment with ad libitum access to food and drinking water. Littermates of the same sex were randomly assigned to experimental groups. Imaging and recordings, following AAV infection and cranial window surgeries, were performed on adult mice, from 70 days onwards. For Cux2-CreERT2 mice, tamoxifen was supplemented through their food pellets (400 mg tamoxifen citrate/kg pellets; 3302.PX.V20, Kliba Nafag) at least one week before the injection of any AAVs, and continued until expression of neurons was observed, usually by three weeks after AAV infection.

METHOD DETAILS

Adeno-associated viruses (AAVs)

Three different AAVs, all of PHP.eB serotype, were used in our report. PHP.eB AAV-CAG-FLEX-GCaMP7s was generated from the plasmid pGP-AAV-CAG-FLEX-jGCaMP7s-WPRE (Plasmid #104495, Addgene) (Dana et al., 2019). PHP.eB AAV-syn-FLEX-splitTVA-EGFP-tTA was generated from the plasmid pGP-AAV-syn-FLEX-splitTVA-EGFP-tTA (Plasmid #100798, Addgene) (Lavin et al., 2020). PHP.eB AAV-TREtight-mTagBFP2-B19G was generated from the plasmid pGP-AAV-TREtight-mTagBFP2-B19G (Plasmid #100799, Addgene) (Lavin et al., 2020). Virus production was performed as previously described in Jüttner et al. (2019). In short, HEK293T cells (CRL-3216, ATCC) were co-transfected with three plasmids: an AAV transgene plasmid, an AAV helper plasmid encoding the AAV Rep2 and Cap proteins for the selected capsid (PHP.eB) (Chan et al., 2017), and the pHGT1-Adeno1 helper plasmid expressing adenoviral genes (kindly provided by C. Cepko, Harvard Medical School, Boston, USA). Transfection was done using branched polyethylenimine (02371, Polysciences). For the production, 10 cell culture dishes each 15 cm in diameter were co-transfected with the mixture of the three plasmids at 80% confluence of HEK293T cells (CRL-3216, ATCC). AAV purification was performed using a discontinuous iodixanol gradient (OptiPrep, D1556, Sigma) and ultracentrifugation for 90 minutes at 242,000 g (Tiscornia et al., 2006). AAV particles were purified and concentrated in Amicon Ultra-15, PLHK Ultracel-PL Membran, 100 kDa columns (UFC910024, Millipore).

For systemic administration of AAVs, mice were anesthetized with 2% isoflurane. 0.5 – 20 μl of purified AAV, with the volume adjusted to 50 μl by adding saline solution (0.9%), was injected retro-orbitally into the sinus using a 30-gauge micro-fine insulin syringe (Yardeni et al., 2011). A minimum of 2×10^{10} genome copies (GC) of virus were injected per gram of mouse weight.

Rabies virus production

To generate the SAD ΔG jGCaMP7s rabies virus, we PCR amplified a fragment containing GCaMP7s and NheI/NotI restriction sites from the pGP-AAV-CAG-FLEX-jGCaMP7s-WPRE plasmid and inserted the resulting fragment into a DNA plasmid containing the genome for SADΔG-mCherry rabies virus, pHHSC-SADΔG-mCherry (Haberl et al., 2015; Wickersham et al., 2007). Next, SADΔG-GCaMP7s virus was rescued in BSR T7/5 cells (Buchholz et al., 1999) transfected with pTIT-SAD G (Finke et al., 2003) and amplified in BHK-MG-on cells providing SAD G (Ghanem et al., 2012). The resulting virus was used to infect BHK-EnvA (Wickersham et al., 2007) cells to obtain Envelope A-coated SADΔG-GCaMP7s virus (“EnvA-SADΔG-GCaMP7s”). The EnvA-coated virus was concentrated by ultracentrifugation and used for *in vivo* injection. Plaque-forming unit (pfu) number titration was performed by infecting BHK-21 cells (ATCC) and HEK293T-TVA (Osakada et al., 2011) cells with G-coated virus and EnvA-coated virus, respectively. The minimum titer used for injection was $> 10^{10}$ pfu/ml.

Immunohistochemistry

Mice were sedated using FMM and then perfused with PBS (diluted from 10X PBS stock (70011044, Thermo Fisher)), followed by 4% (wt/vol) paraformaldehyde (PFA) diluted in PBS. Brains were immediately removed and placed in 4% PFA, overnight at 4°C. Brains were washed three times for 10 min in PBS. To improve antibody penetration, brains were cryoprotected by transferring the brains to 30% (wt/vol) sucrose and left until brains sunk. They were then subjected to 3 freeze–thaw cycles using dry ice and either further processed or stored at -80°C prior to processing. Brains were embedded in 4% agarose (SeaKem LE Agarose, Lonza) and 150 μm thick coronal sections were then cut using a vibratome (VT1000S vibratome, Leica Biosystems). Slices were incubated for 2h in blocking buffer containing 10% (vol/vol) normal donkey serum (NDS) (Chemicon), 1% (wt/vol) BSA, 0.5% (vol/vol) Triton X-100 and 0.01% sodium azide (SigmaAldrich) in PBS, followed by a primary antibody treatment for 3–7 days at room temperature in buffer containing 3% (vol/vol) NDS, 1% (wt/vol) BSA, 0.01% (wt/vol) sodium azide and 0.5% Triton X-100 in PBS. The primary antibody used in this study was a rat monoclonal anti-GFP (Catalog no. 04404-84, RRID: AB_2313654, Nacalai). The slices were then washed three times in PBS before being transferred to secondary antibody incubation for 24h at room temperature. The secondary antibody used in this study was an Alexa Fluor 488 donkey anti-rabbit IgG (heavy and light chains (H+L), catalog no. A-21206, RRID: AB_141708, Thermo Fisher Scientific). Slices were stained in PBS supplemented with Hoechst 33342 (10 $\mu g ml^{-3}$) for 20 min at room temperature. Before embedding, slices were washed three times in PBS and then embedded in ProLong Gold Antifade Mountant (Thermo Fisher Scientific). A spinning disc microscope (Axio Imager M2 upright microscope, Yokogawa CSU W1 dual camera T2 spinning disk confocal scanning unit, Visitron VS-Homogenizer on an Olympus IXplore Spin confocal spinning disc microscope system) was used to image slides, using a 20X (UPLSAPO20X, Olympus) objective.

Cortical layer targeting

To study inhibitory cell types within cortex, Gad2-IRES-Cre mice (Taniguchi et al., 2011) were injected with PHP.eB AAV-CAG-FLEX-GCaMP7s. Inhibitory neurons within L1 were distinguished from all other inhibitory neurons by the relative depth of the recording, with neurons shallower than 100 μm defined as being in L1 and neurons deeper than 100 μm grouped as cortical inhibitory neurons (Lein et al., 2007). To study cortical L2/3, Cux2-CreERT2 (Franco et al., 2012) mice were used. Cre was induced by feeding the mice food pellets supplemented with tamoxifen (as described above), and then PHP.eB AAV-CAG-FLEX-GCaMP7s was injected. To study cortical L4, Scnn1a-Tg3-Cre mice (Madisen et al., 2010) were injected with PHP.eB AAV-CAG-FLEX-GCaMP7s. To study cortical L5, three mouse lines were injected with PHP.eB AAV-CAG-FLEX-GCaMP7s: Rbp4-Cre KL100 (Gerfen et al., 2013; Gong et al., 2007), Tlx3-Cre PL56 (Gerfen et al., 2013) (to label the IT subpopulation), and Sim1-Cre KJ18 (Gerfen et al., 2013) (to label the PT subpopulation). To study cortical layer 6, Ntsr1-Cre GN220 mice (Gong et al., 2007) were injected with PHP.eB AAV-CAG-FLEX-GCaMP7s.

Cranial window implantation

Cranial windows were implanted 1-3 weeks after AAV injection. Mice were anesthetized with Fentanyl-Medetomidine-Midazolam (FMM) (Fentanyl (Janssen, 0.05 mg/kg), Medetomidine (Virbac AG, 0.5 mg/kg), Midazolam (Sintetica, 5 mg/kg)). To prevent dehydration of the cornea during surgery, we applied Coliquifilm (Allergan) to the eyes. The skin was removed, the skull cleared of tissue, and a thin titanium holder was attached to the skull with dental cement (Superbond C&B) allowing for head fixation during calcium imaging (Holtmaat et al., 2009). For recordings in posterior cortex, a 4 mm diameter craniotomy was made over the left hemisphere, exposing the visual cortices and surrounding areas. For recordings in anterior cortex, a semi-circular craniotomy was made over the left hemisphere. After removal of the bone, dehydration of the cortical surface was minimized by repeatedly applying cortex buffer to the surface (Cortex buffer: 125 mM NaCl, 5 mM KCl, 10 mM glucose, 10 mM HEPES, 2 mM $MgSO_4$ and 2 mM $CaCl_2$). The cortical surface was covered with either a 4 mm diameter glass coverslip (for craniotomies in the posterior cortex) or a coverslip cut to shape (for craniotomies exposing the anterior cortex), and sealed with UV glue (NOA 68, Norland), stabilized by an additional layer of dental cement. Buprenorphine (Temgesic, 0.05-0.1 mg/kg) was injected 20 minutes before the end of the surgery to provide extended pain relief during the immediate recovery from surgery. At the end of surgery, mice were woken using an antagonist mixture to counteract FMM anesthesia (Atipamezol (Virbac, 2.5 mg/kg), Flumazenil (Sintetica, 0.5 mg/kg)). Mice were monitored daily following surgery and allowed to recover for at least 10 days before any experimental manipulations.

Two-photon in vivo calcium imaging

GCaMP7s expressing neurons were imaged using two different two-photon (920 nm) laser scanning microscopes (Holtmaat et al., 2009). The first, a Femtonics galvo-galvo scanning microscope, was equipped with a Nikon 25X water immersion objective (1.1 NA). Imaging was performed at 5-10 Hz, up to 750 μm below the cortical surface (cortical layers 1-6). Each recording of spontaneous calcium activity was 5 minutes in length. The second two-photon microscope used was a FemtoSMART resonant-galvo scanning microscope. It was equipped with an Olympus 16X water immersion objective (0.8 NA). This microscope was used for simultaneous imaging and electrophysiology. Recordings were made at 27 Hz, for 2 minutes. The temperature of the animal was kept at 37 °C using a temperature controller (TC1000, CWE). During all imaging sessions, mice (both awake and anesthetized) were head fixed under the objective, within a light-proof box to ensure darkness. Mice were monitored during recordings, under infrared illumination (DMK 22BUC03, Imaging Source). For recordings of mice injected with rabies, pairwise recordings were performed in both awake and anesthetized conditions. Therefore, only Iso anesthesia was used, to ensure that both recordings could be performed sequentially, minimizing movement within the recording field. Awake recordings were performed first, followed by Iso induction. Steady state Iso anesthesia was confirmed via lack of spontaneous movements, lack of muscle tone, and the absence of a paw withdrawal reflex in response to a toe pinch, as detailed below.

Calcium indicators temporally smooth signals, but have high sensitivity, and GCaMP7s can detect single action potentials (Dana et al., 2019). The imaging frame rate imposed a constraint on the recording precision of the relative timing of each individual event, and the resulting quantification of temporal alignment of the activity between neurons. For bursting activity, while we were unable to detect individual underlying events (> 10 Hz) (Dana et al., 2019), we were able to detect each burst through the change in amplitude in the smoothed calcium signal.

Rabies infection of Rbp4-Cre neurons

To label the population of cortical neurons presynaptic to L5 PNs, we followed the previously described double AAV strategy (Lavin et al., 2020) using one PHP.eB AAV to drive Cre-dependent expression of the avian receptor for envelope-A (TVA) and tetracycline-controlled transactivator protein (tTA2), and a second PHP.eB AAV to drive tTA2-dependent expression of the rabies glycoprotein G. In detail, we performed retro-orbital injections of Rbp4-cre mice with a mixture of 0.5 μl of PHP.eB AAV-syn-FLEX-splitTVA-EGFP-tTA (with a titer of 1.0×10^{14} GC/ml) and 7 μl of PHP.eB AAV-TREtight-mTagBFP2-B19G (with a titer of 5.0×10^{13} GC/ml), adjusted for each 25 g of mouse weight. 12 days later, we placed a cranial window above visual cortex, as described above. During the cranial window surgery, 300 nl of Env-SADΔG-GCaMP7s rabies was injected using a stereotactic micromanipulator (SM-15R, Narishige) and a microinjector (IM-9B, Narishige). The injections were stereotactically positioned in the visual cortex, 500 μm below the pial surface. The injection needle was pulled from borosilicate glass with filament (BF100-50-10, Sutter Instrument) using a P-97

micropipette puller (Sutter Instrument). After the injection, the needle was left in place for 10 min to prevent backflow. Cortical neurons directly presynaptic to L5, identified by expression outside of L5, were imaged using a two-photon microscope, 7 – 14 days after the injection, as detailed above.

Steady-state anesthesia during experiments

Mice were defined to be awake in the absence of any anesthetic, if they showed muscle tone in their face, jaw, and body and demonstrated eye, whisker, or body movements (Adams and Pacharinsak, 2015; Danneman et al., 2012). Muscle tone was monitored throughout all experiments via visual inspection under IR illumination (DMK 22BUC03, Imaging Source). A pulse oximeter attached to a sensor applied to the rear paw (MouseSTAT Jr with Paw Sensor, Kent Scientific) was used to monitor the heart rate of mice. Additionally, in a subset of mice, EEG measurements were used to monitor them while awake, and during anesthesia, as described below (Figure 1B). We observed that, while awake, mice showed a heart rate higher than 500 bpm and a θ-δ EEG ratio > 0.5. Within any experimental day, no recordings on awake mice were performed following any injected anesthesia. A brief period of isoflurane anesthesia was used to head-fix each animal under the microscope, and all awake recordings were performed at least 10 minutes following this short isoflurane exposure.

For the induction and maintenance of general anesthesia during experiments, mice were anesthetized with either a mixture of Fentanyl-Medetomidine-Midazolam (Fentanyl (Janssen, 0.05 mg/kg), Medetomidine (Virbac, 0.5 mg/kg), Midazolam (Sintetica, 5 mg/kg)), 1.75% Isoflurane (Provet) delivered using a Respironics EverFlo OPI pump, Phillips, UniVet Porta Anesthetic machine (using a Datex Ohmeda Isotec 5 continuous flow vaporizer), Groppler Medizintechnik), or a mixture of Ketamine and Xylazine (Ketamine (Pfizer, 100 mg/kg), Xylazine (Bayer, 16 mg/kg)). Injectable anesthetic agents were administered, subcutaneously, through single bolus injections. The desired mixture of isoflurane with oxygen was generated by the vaporizer and applied to the mouse through a nasal mask (Groppler Medizintechnik), with a flow rate of 0.8 l/min.

Anesthesia was held at a surgical depth, as assessed by the lack of spontaneous movement, lack of muscle tone in the jaw, face, and body, the absence of a paw withdrawal reflex in response to a toe pinch, as well as a rapid, shallow breathing rate, without gasping. During a consistent surgical depth of anesthesia, Iso anesthetized mice were observed to have a heart rate of 350 – 400 bpm (Adams and Pacharinsak, 2015; Ewald et al., 2011), Ket-Xyl anesthetized mice had a heart rate of 250 – 300 bpm (Xu et al., 2007), and FMM anesthetized mice had a heart rate of 200 – 250 bpm (Fleischmann et al., 2016). In all three anesthetics, mice showed a θ-δ EEG ratio < 0.5 (Figure 1B). During both awake and anesthetized experimental sessions, the eyes of the mice were open, but all recordings were performed in darkness. The specific parameters used were as in our Animal Protocol, approved by Canton Basel-Stadt, as per the European Communities Guidelines on the Care and Use of Laboratory Animals (2010/63/EU).

For experiments where the depth of anesthesia was varied (Figures S2 and S3), the depth of anesthesia was defined as follows. Light anesthesia was defined by the presence of a righting reflex and shallow, non-gasping breathing. Deep anesthesia was defined by the absence of a righting reflex, and the presence of gasping breathing.

To measure spontaneous activity in response to increasing concentrations of Iso anesthesia (for Figure S2), we recorded following at least 10 minutes of application of each concentration of Iso to the mouse. We assessed the depth of anesthesia at each concentration through presence of spontaneous movements, muscle tone in the jaw, face, and body, as well as the disappearance of the paw withdrawal reflex in response to a toe pinch (Adams and Pacharinsak, 2015). At 1% isoflurane, mice showed spontaneous movements. Additionally, muscle tone and the paw withdrawal reflex were both present. The respiratory rate remained rapid but was shallower than while awake. This corresponded to light anesthesia. Additionally, mice demonstrated both a righting reflex, and a paw withdrawal reflex (in response to a toe pinch). At 1.5% and 2% isoflurane, spontaneous movements, muscle tone, and the paw withdrawal reflex were all absent. Again, the respiration rate remained rapid, but became even more shallow. Hence, these concentrations of Iso corresponded to a surgical depth of anesthesia. Finally, at 2.5% isoflurane, in addition to the loss of movements and reflexes, the mouse demonstrated gasping respiration. Hence, this corresponded to deep anesthesia.

To measure spontaneous activity in the presence of medetomidine (for Figure S2), we recorded at least 10 minutes following a subcutaneous injection of 0.5 mg/kg of medetomidine. For increasing concentrations of Iso anesthesia, we recorded following at least 10 minutes of application of each concentration of Iso. Mice injected with medetomidine, in the absence of any isoflurane, displayed both a righting reflex and a paw withdrawal reflex (in response to a toe pinch). In contrast, mice anesthetized with medetomidine, in the presence of 1%, 1.5%, and 2% Iso did not show both a righting reflex, and a paw withdrawal reflex (in response to a toe pinch).

To measure spontaneous activity in the presence of varying concentrations of FMM (for Figure S2), we recorded 5 minutes following a single injection of FMM, and then injected a second dose of FMM (half the normal dosage), before making a second recording 5 minutes following the second injection.

Loss and recovery of consciousness

Anesthetic protocol

To determine the timing at which mice lose motor behaviors following the induction of anesthesia, we head-fixed mice under the two-photon microscope in darkness and allowed them to acclimatize. To study synchrony during loss of consciousness (LOC), we used Iso to anesthetize mice, so as to precisely control the timing of the onset anesthesia. Mice were awake for 20 minutes, prior to the induction of 1.75% Iso anesthesia, and their behavior was monitored under infrared illumination (DMK 22BUC03, Imaging Source).

With the onset of 1.75% Iso anesthesia, we recorded the movement of the mice, and identified the point at which each mouse stopped initiating whisker movements, eye and eyelid movements, as well as overall body movements. Additionally, mice were confirmed to be at a surgical depth of anesthesia immediately following the recording, by the absence of a paw withdrawal reflex in response to a toe pinch.

To determine the timing at which mice regain motor behaviors following the termination of anesthesia, we performed two sets of experiments. In the first case, we head-fixed mice under the two-photon microscope in darkness and allowed them to acclimatize, while monitoring them under infrared illumination (DMK 22BUC03, Imaging Source). To study synchrony during return of consciousness (ROC), we used Iso to anesthetize mice, so as to precisely control the timing of the offset of anesthesia. Mice were then anesthetized for 10 minutes with 1.75% Iso anesthesia. At this point, mice were confirmed to be at a surgical depth of anesthesia, by the absence of a paw withdrawal reflex in response to a toe pinch, just prior to the termination of anesthesia. With the termination of 1.75% Iso anesthesia, we recorded the movement of the mice, and identified the point at which each mouse started initiating whisker movements, eye and eyelid movements, as well as body movements. All mice had shown such spontaneous movements, prior to the end of the recording interval. Additionally, mice were confirmed to show a paw withdrawal reflex in response to a toe pinch, following the end of each ROC recording. In the second case, we recorded the timing of the recovery of the righting reflex following the termination of anesthesia. We anesthetized mice for 10 minutes at 1.75 % Iso in an induction chamber (Groppler Medizintechnik), and then removed them from the chamber and placed them on their backs. At this point, mice were confirmed to be at a surgical depth of anesthesia, by the absence of a paw withdrawal reflex in response to a toe pinch. The timing at which mice initiated a righting turn was then recorded, which we defined as the timing of recovery of the righting reflex for each mouse.

Behavioral changes

Curves describing the behavioral change during the induction and termination of anesthesia were generated by calculating the fraction of mice that showed the loss or recovery of each type of motor behavior at each time point. The transition period for motor behavior was defined by the time period from when 25% to 75% of the mice demonstrated the change in motor behavior. For a subset of mice, two photon recordings showed strong movements, and therefore, only behavioral timing was recorded, with the neuronal synchrony not computed. For the comparison of the transition time of neuronal synchrony with the time at which mice stopped moving, for individual mice, we defined the transition time of motor behaviors, for each mouse, as the time point at which the last motor behavior of any type (i.e. eye or eyelid, whisker, or body movements) was observed, during the induction of anesthesia.

Electroencephalography (EEG). To install EEG monitoring screws within the skull, mice were anesthetized with Fentanyl-Medetomidine-Midazolam (FMM) (Fentanyl (Janssen, 0.05 mg/kg), Medetomidine (Virbac AG, 0.5 mg/kg), Midazolam (Sintetica, 5 mg/kg)). To prevent dehydration of the cornea during surgery, we applied Coliquifilm (Allergan) to the eyes. The skin was removed, the skull cleared of tissue, and a thin titanium holder was attached to the skull with dental cement, allowing for head fixation during EEG recordings. Two indentations were drilled into the skull, one over the visual cortex and the other over cerebellum. In each indentation, a screw (M0.6 x 0.8, US Micro Screw) was tightened. A Teflon-coated silver wire (AGT0510, World Precision Instruments) was stripped on both ends and then soldered to a connector pin on one end. The other end of the wire was tied around the screw above visual cortex. The wire was then connected to the first recording channel of the EEG (Neurologger 2A, Evolocus LLC) using the connector pin. All the other recording channels, ground, and reference channel were grounded to the mouse. Recordings were taken at a frequency of 400 Hz. Steady state recordings were performed following application of FMM, 1.75% Iso, Ket-Xyl (Figure 1B), medetomidine, 1% Iso, and medetomidine together with 1% Iso (Figure S3). For recordings during both LOC and ROC, to characterize the time course of the induction and termination of anesthesia, mice were anesthetized with 1.75% isoflurane applied to the mouse through a nasal mask (Groppler Medizintechnik), with a flow rate of 0.8 l/min. Mice were head-fixed while awake for at least 20 minutes before the start of LOC recordings. The recordings were started with the onset of Iso anesthesia, and recordings were made for a total of 5 minutes. Mice were confirmed to be at a surgical depth of anesthesia immediately following the recording, by the absence of a paw withdrawal reflex in response to a toe pinch. Prior to the start of ROC recordings, mice were anesthetized in 1.75% Iso for 10 minutes. At this point, mice were confirmed to be at a surgical depth of anesthesia, by the absence of a paw withdrawal reflex in response to a toe pinch, just prior to the termination of anesthesia. Recordings were started with the termination of Iso anesthesia and were made for a total of 5 minutes.

Following each recording, the Neurologger unit was disconnected from the wires, and connected to a Neurologger USB adapter (Evolocus LLC). The Downloader utility (v2.02, Evolocus LLC) was used to import the data stored on the Neurologger unit. The same utility was then used to convert the data to Float32IE, to allow the recordings to be imported into Matlab for further analysis (R2020a, Mathworks). All data on the Neurologger was then erased prior to the next recording.

Widefield imaging. Widefield fluorescence imaging was performed as previously described (Garrett et al., 2014; Marshel et al., 2011; Zhuang et al., 2017). The cortex was illuminated with blue light (U-HGLGPS light source filtered through a bandpass excitation filter, 460-495 nm, SZX2-FGFPA, Olympus), and imaged using an epifluorescence microscope (SZX16, Olympus) with a 1.6x objective (SDF PLAPO 1.6x PF, Olympus). The focal plane of imaging was below the cortical surface. Fluorescent light emitted from GCaMP7s was filtered through a bandpass emission filter (510-550 nm, SZX2-FGFPA, Olympus), and detected using a CMOS camera (ORCA-Flash4.0 V3, Hamamatsu). Data was recorded via the CameraLink interface, using the HCImage Live software (Hamamatsu).

To determine retinotopic maps of visual responses, mice were presented with flickering, periodically drifting bars (4 cardinal directions of motion, 8 bar sweeps per direction) (Kalatsky and Stryker, 2003; Marshel et al., 2011; Zhuang et al., 2017). We ensured that

the size and speed of the bar was constant relative to the mouse's perspective. Stimuli were generated using PsychoPy (Peirce et al., 2019) and displayed on an edge-LED display (UE40KU6400U, Samsung). The display was placed within the contralateral visual field from the surgical window, such that it covered -65.5 to 65.5 degrees in azimuth and -26.5 to 64 degrees in altitude, within the visual field of the head-fixed mouse. In contrast to the imaging used for mapping visual cortices, to compare the awake and anesthetized conditions under all three anesthetics (FMM, Iso, and Ket-Xyl) across cortex, imaging was performed in darkness, without any visual stimulation.

Electrophysiology. For electrophysiological recordings we used whole-cell patch pipettes, pulled from borosilicate glass with filament (O.D.: 1.5 mm, I.D.: 0.86 mm) using a P-97 micropipette puller (Sutter Instrument Company) and filled with intracellular solution containing: 0.2 mM EGTA, 130 mM K-gluconate, 4 mM KCl, 2 mM NaCl, 10 mM HEPES, 4 mM ATP-Mg, 0.3 mM GTP-Tris, 14 mM phosphocreatine-Tris, 0.050 mM Alexa-594 and brought to pH 7.25 (with dilute NaOH or HCl) and 292 mOsm (by addition of H_2O).

Animals were previously prepared with a cranial window, as described above. On the day of recording, animals were then anesthetized with FMM (to maximize stability during electrophysiological recordings) and the coverslip over the cortex was removed, and replaced with a coverslip that had been cut in half to allow access for the recording pipette. The mouse was transferred to the two-photon microscope stage, where it was head fixed. A ground wire was positioned in the immersion solution (cortex buffer, as above). Signals (sampled at 50 kHz and low pass filtered at 10 kHz) were recorded using a National Instruments Board connected to a Multiclamp 700B amplifier (Molecular Devices). All recordings were performed in darkness.

The whole-cell patch pipette, filled with red fluorescent dye, was then lowered through the opening in the coverslip under positive pressure (200 mbar). Once the dura was penetrated and dye from the pipette filled the extracellular space, the pressure was lowered (50-70 mbar) and the pipette was advanced diagonally either to the depth of the cell layer containing Rbp4-Cre positive neurons (450 – 520 μm) or to the depth of L2/3 (100 – 250 μm). RBP4-Cre positive neurons were visualized by their expression of GCaMP7s. L2/3PNs were visualized by the injection of dye into the extracellular space.

The pressure on the pipette was further reduced just before touching the membrane of the target neuron, and finally released to form a gigaohm seal under visual guidance. Slow and fast pipette capacitances were compensated, and whole-cell access was achieved by applying a negative pulse of pressure on the pipette. A subset of recordings was performed in a juxtacellular configuration, without a gigaohm seal.

QUANTIFICATION AND STATISTICAL ANALYSIS

Filtering of calcium traces

Two-photon recordings were imported as 3D matrices of the recorded activity within a spatial region in time. Motion in the imaging field during the recordings was stabilized through the use of the NoRMCorre algorithm, using the publicly available Matlab implementation (Pnevmatikakis and Giovannucci, 2017). Custom code (Matlab R2020a, Mathworks) was used for manual selection of elliptical regions of interest (ROIs) containing individual cells or dendrites. Raw activity traces were computed by taking the average of the pixels within the ROI at each time point. Within each imaging field, three separate regions of background expression were also selected.

For denoising, the raw traces were then converted to the Fourier domain. A threshold, fixed to 150% of the mean amplitude component of the trace, was then applied to the amplitude component across the entire frequency range. This reduces white noise across the frequency spectrum, without adding a bias to any specific frequency component. Additionally, we removed the amplitude at Nyquist frequency. For all recordings except for those with surface dendrites, the total power within the filtered frequency spectrum, averaged across the background ROIs, was used as a secondary threshold. If an ROI contained a power less than the mean over the background ROIs', the filtered trace was set to zero. In contrast, if an ROI contained power greater than the background ROIs' power, the filtered amplitude component was then inverted back to obtain a filtered trace in time. The $\Delta F/F$ trace was then computed by utilizing the mean amplitude across the entire recording as our estimate of f. Finally, a rolling mean with a time constant of approx. 62.5 s was then subtracted away from the filtered activity trace, to ensure that the baseline was stable across the recording length. This trace was then used for all further analyses, unless specifically detailed otherwise in the methods.

EEG analysis

All analysis on EEG recordings was performed using custom code in Matlab (R2020a, Mathworks). Each five minute recording was divided into consecutive 15 s intervals (Kohtoh et al., 2008). Each interval was then subdivided into five 3 s Hamming windows. Within each window, a fast Fourier Transform of the signal was computed. The amplitude of the frequency spectrum for each 15 s interval was defined as the average across all five Hamming windows. This amplitude spectrum was divided into frequency bands, and the average amplitude within each band was computed. In particular, the ratio of the amplitude within the θ (3.5 – 10 Hz) and δ (0.5 – 3 Hz) bands ("θ-δ EEG ratio") was used as a metric of the relative shift to lower frequencies during anesthesia (Pal et al., 2018). While awake and under steady state anesthesia, the value of the θ-δ EEG ratio was computed by averaging the value across all 15 s intervals. In contrast, during LOC and ROC recordings, θ-δ EEG ratios computed during each 15 s interval were compared against the distribution of θ-δ EEG ratios, across mice, during steady-state anesthesia. For each interval during either LOC or ROC, we computed the probability that the values of the θ-δ EEG ratio sampled during that interval, across all mice, were drawn from the distribution of θ-δ EEG ratios while awake or during steady state Iso anesthesia. We first Monte Carlo sampled values from a merged distribution during

steady state and the specific LOC or ROC interval to obtain a distribution of the difference of means of the sampled values relative to the mean of the entire steady state distribution. We then computed the probability that a difference of means of the merged distribution in the awake state is larger than or equal to the difference of means within each interval. Similarly, we computed the probability that a difference of means of the merged distribution in the anesthetized state is smaller than or equal to the difference of means within each interval. This yielded two curves describing the probability that the median instantaneous neuronal synchrony is drawn from the awake ("awake-probability curve") or the anesthetized steady state distributions ("anesthetized-probability curve") (as in Figures 3C and 3G).

Widefield image analysis

We extracted the phase maps for each motion direction by correlating the fluorescence signal in each pixel with a series of time-shifted gaussians spanning one cycle of the drifting bar. Phase maps from opposite directions were subtracted to reconstruct the absolute retinotopic map for the horizontal and vertical directions. Pixels with a correlation coefficient < 0.5 - after averaging peak Pearson correlation coefficients from the four directions and applying a 9x9 pixel median spatial filter - were considered unresponsive. Finally, the visual sign map was computed as the sign of the difference between the vertical and horizontal retinotopic gradients at each pixel. Patches of the visual sign map were automatically detected (Matlab 2020a, Mathworks), then manually registered to a reference sign map (derived from Garrett et al., 2014 and Zhuang et al., 2017) to identify the primary and higher visual cortices. Adjacent non-visual cortical areas were then labled, using the visual cortices as a reference (Fulcher et al., 2019; Madisen et al., 2015).

For the analysis of the relative delay between pixels during anesthesia compared to wakefulness, we obtained raw fluorescence traces per pixel in darkness at 10 Hz, with the monitor used for visual display turned off (i.e. in the absence of visual stimulation, in darkness). We down sampled the pixel density by a factor of 4 in each dimension, by averaging the values in 4x4 blocks of pixels, thereby reducing the recording noise. As with two-photon recordings, the NoRMCorre algorithm (Pnevmatikakis and Giovannucci, 2017) was used to reduce any movement during recordings. The activity in each block of pixels was then filtered by subtracting away a rolling mean of the activity with a time constant of 125 s, to ensure that the baseline was stable across the recording length.

To determine the relative delay between the activity of pixel blocks across the imaging window, we computed the cross correlation of the filtered traces from each block. The absolute value of the time lag of the peak in cross-correlation relative to zero was defined as the relative delay between the two pixel blocks. This analysis was performed for all pairs of pixel blocks throughout the imaging window, excluding pixels that were within the blood vessels, and within the reflective edge of the glass, which were masked out prior to any analysis. To obtain a representation of the delay with distance, we combined the relative delay of each pair of pixel blocks with the relative distance between the pixel blocks, and computed the distribution of delays for all pixel pairs a specific distance apart.

We defined the relative delay between the activity of individual cortical areas, within the imaging window, analogously to the delay between pixel blocks. The activity of each cortical area was defined as the mean activity across 100 2x2 blocks of pixels within the cortical area. Then, the relative delay was computed, between the activity traces of individual cortical areas, as for pixel blocks.

Filtering of voltage traces

Raw recorded voltage traces were imported for analysis using the publically (Matlab R2020a, Mathworks), and spiking activity was filtered from the subthreshold membrane voltage. Subthreshold membrane voltage was processed identically as with calcium signals (described above), with the noise threshold set to 100% of the mean amplitude spectrum, in the frequency domain. Following this, a rolling mean with a time constant of 12.5 s was subtracted from the ΔF/F trace.

Predicted calcium activity was generated from recorded spiking activity. To do so, we convolved the spiking activity with an alpha function representing the dynamics of the calcium indicator, with the form: $\tau_r\tau_d/(\tau_r - \tau_d)\cdot(e^{-\tau_d t} - e^{-\tau_r t})$, where the rise and decay time constants (τ_r and τ_d) were fit to rise and decay times previously reported for GCaMP7s (Dana et al., 2019). Simulated calcium traces were then filtered as with all recorded calcium traces, only with a threshold of 100% of the mean amplitude component of the Fourier transform.

Correlation analyses

To calculate the synchrony across a population of a specific cellular compartment (e.g. soma or dendrites) within a recording, we computed the pairwise Pearson correlation between activity within each individual region of interest containing a given compartment (filtered as described above) and the mean across the activity in all cellular compartments of the same type within a given recording, excluding the region of interest for which the synchrony is being computed (Matlab 2020a, Mathworks). Similarly, to obtain the relative synchrony between basal dendrites and the somas within each calcium imaging recording, we computed the Pearson correlation between the activity of each basal dendrite and the mean of the activity across all somatic ROIs. To determine the relative synchrony between apical dendrites and the soma, we computed the Pearson correlation between the mean of the activity of all apical dendrites, with both the predicted calcium activity at the soma (from the spiking activity recorded simultaneously in the soma) and the filtered subthreshold activity recorded simultaneously from the soma, where the predicted calcium activity and the subthreshold activity were down sampled to the frame rate of the calcium recording by averaging over the intervals when a calcium frame was being recorded. To determine the relative synchrony between L2/3 PNs and L5 PNs, we computed the Pearson correlation between filtered subthreshold activity recorded from each L2/3PN, with the mean of simultaneously recorded calcium activity across L5 PNs. As before, the subthreshold activity was down sampled to the frame rate of the calcium recording by averaging over the intervals

when a calcium frame was being recorded. In comparisons with membrane voltage, only cells that showed at least one spontaneous spike during recordings were included in the analysis. In addition, to obtain the average neuronal synchrony per mouse (Figure S6), we computed the median neuronal synchrony across all neurons measured in a given mouse.

For analyses of changing synchrony, during the induction and termination of anesthesia, we computed the synchrony within a rolling window with a length of 15 s (independent of the frame rate of each individual recording), sampled every three seconds during the course of the recording. We then compared the instantaneous distribution of synchrony in each window against the steady state distribution recorded during wakefulness, or during steady state Iso anesthesia. Specifically, we combined the instantaneous synchrony values recorded in each window with the synchrony values recorded from one steady state condition (awake or anesthetized) to generate a combined distribution. We then Monte Carlo sampled values from this combined distribution to obtain a new sample with the same size as the recorded instantaneous synchrony values, and created a distribution of the difference of medians of the sampled values relative to the median of the combined distribution. We computed the probability that a difference of medians of the combined distribution in the awake state is equal to or larger than the difference of median of the instantaneous distribution in each window. Similarly, we computed the probability that a difference of medians of the combined distribution in the anesthetized state is equal to or smaller than the difference of median of the instantaneous distribution in each window. This analysis yielded two curves, describing the probability that the median instantaneous neuronal synchrony is drawn from either the awake or the anesthetized steady state distributions (the ''awake-probability curve'': P(awake) and ''anesthetized-probability curve'': P(iso), as described in the text and labeled in Figures 3A, 3E, S4, and S5).

To provide alternative quantifications of synchrony (Figure S1), we used two different approaches. First, we computed the distribution of Pearson correlation coefficients between all pairs of neurons (Matlab 2020a, Mathworks). This is a standard description of the similarity of pairs of neurons, but it only provides an indirect indication of synchrony across a population. Second, we computed the normalized temporal variance of the population, as introduced in Golomb and Rinzel (1994) (termed the χ metric of neuronal coherence). In detail, we computed the variance of the amplitude of each individual neuron within the population. We, then, took the mean of the activity across the population, and calculated the variance of the amplitude of the mean, as a fraction of the mean of the variance of all individual neurons. This generated the quantification which we term the normalized temporal variance, which varies from 0 to 1, and characterizes the relative alignment of temporal activity traces across the population. However, this quantification provides a single metric for the entire population, and does not convey the variation of individual cells compared to the population. Therefore, we converged upon the correlation with the population mean (as discussed in the text) as our metric of neuronal synchrony.

Computing event-based statistics

The change in fluorescence intensity as a function of the mean fluorescence intensity within the ROI during the entire recording interval (defined as $\Delta F/F$), was computed from calcium activity traces derived from the summed pixel responses within each ROI. Individual events were identified within these $\Delta F/F$ traces by thresholding at 3% $\Delta F/F$ (for noise reduction), and detecting the frames where the activity is greater than this noise threshold. An event begins at the frame when the recorded trace increases above the threshold, and lasts until the trace returns to the threshold. The frequency of events in each ROI is computed by dividing the total number of events by the total time of the recording. The inter-event interval is defined as the time from the start of one event to the start of the next event. This choice includes the timing of the calcium decay from individual events, but it is chosen due to the asymmetric rise and decay time kinetics of the calcium indicator (Dana et al., 2019), such that the rise time is much faster than the decay time, and therefore better characterizes the true timing of an event.

Analysis of mean activity

As with event-based statistics, the mean activity within each recording was computed from the denoised $\Delta F/F$, such that the total activity greater than 3% $\Delta F/F$ was summed over the entire recording, and then normalized by the length of each recording. To quantify the distribution of the change in mean activity between each anesthetized condition and the awake state (Figure 4H), we computed the pairwise difference of mean spontaneous activity for every pair of recorded neurons.

Computing entropy

We computed the distribution of activity across the population within individual time bins, and then averaged across time. We defined this as the information entropy of the population of neurons within each recording. In detail, we first normalized the filtered activity of each neuron to the minimum and maximum of its own activity. In each bin of 250 ms, we computed the fraction of neurons whose normalized activity was within each of 4 bins (0 – 25 %, 25 – 50 %, 50 – 75 %, and 75 – 100 %). We then computed the entropy of the distribution, within each time bin, using the observed fractions, f_b, in each amplitude bin, such that entropy is equal to $-\sum_{bins} f_b \cdot \log_2 f_b$.

We averaged this value across all time bins, to obtain an estimate of the entropy for each recorded population (Figure 4G). To calculate the entropy within each individual neuron over time, we computed the fraction of time bins when the neuron demonstrated activity within each amplitude bin, and used this fraction to compute the entropy of each neuron. We then averaged this entropy across all neurons in the population (Figure S9).

To quantify the distribution of the change in entropy between each anesthetized condition and the awake state (Figures 4G and S9), for each cell type, we computed the pairwise difference in entropy between all pairs of recorded populations.

Statistical analyses

All statistical comparisons of distributions, except for those shown in Figures 3, 4I, 5D, 5E, 6D, S4, S5, S8, and S15 were performed using the two-sided Wilcoxon rank-sum test. The significance threshold, prior to Bonferroni correction, and the number of comparisons used to perform Bonferroni correction for each test is described in the figure legends. In summary, a 3σ threshold ($P < 0.003$) was used for all data from individual neurons (or dendrites), and a 2σ threshold ($P < 0.05$) was used for all data averaged across each recording, or mouse.

For Figures 3, 4I, S4A, S4B, S5, S8, and S15 statistical comparisons between two distributions were performed through Monte Carlo sampling. The combined distribution was resampled to obtain two samples, each with the same size as each of the original distributions. This Monte Carlo sampling was performed repeatedly, to obtain a distribution of possible resamples from the combined distribution. A comparison (e.g. the difference of the medians) was then computed between each pair of samples. Computing the same comparison for the observed distributions, the value of the comparison can be compared against the distribution of the comparison across the Monte Carlo samples using a Z-score. From this Z-Score, an associated p value can also be computed. In Figure 3, we utilize this approach to plot a curve of the changing P value for different instantaneous synchrony (and θ-δ EEG ratio) values, when compared to the awake and Iso anesthetized steady state distributions. In Figures 4I, S8A, and S15, we utilize this approach to compare the relative distance of the anesthetized distributions from the awake distribution, for different cortical cell types (plotting the Z score, directly).

For Figure 5D, to compare the cumulative probability distributions, we used the Kolmogorov-Smirnov test. For Figures 5E and S4D, because recordings were made from the same neurons in both awake and Iso anesthetized conditions, we used a paired test, the Wilcoxon signed rank test. For Figure 6D, we generated bootstrapped confidence intervals for the median of the relative time delays. We sampled with replacement from the original distribution, to obtain 1000 samples with the same size. We then computed the median across the samples and computed the standard deviation to obtain the confidence interval.

For Figure S4C, we calculated the Pearson correlation between the vector of transition times of neuronal synchrony, and transition times of motor behavior across the 13 mice, to obtain "r". We also computed the root mean squared error (RSME) between the two vectors, by computing the mean of the squared difference between the vector of transition times of neuronal synchrony and transition times of motor behavior, and then taking the square root of the result. This measure quantifies the average of the difference between each pair of transition times for each mouse, independent of the sign of the difference.

To generate Figure S8B, we performed a Bayesian estimation (Kruschke, 2013) of the probability that different beta (B) distributions, with varying parameter values (α and β), could generate the observed values. In detail, we chose to use a beta (B) distribution to model our observations because this distribution is defined on a limited interval (0 to 1), just like neuronal synchrony. We chose a flattened distribution for the prior distributions for both α and β, by multiplying the standard deviation observed in each condition and cell type by 5 and, since both parameter values must extend from 0 to $+\infty$, defining a gamma distribution with that adjusted standard deviation from which to sample α and β values. To sample from the beta (B) distributions, we utilized Gibbs sampling, a Markov Chain Monte Carlo (MCMC) algorithm, using publicly available code (Matlab Bayesian Estimation, Github) on Matlab (Mathworks, 2020a). We used 10 MCMC chains, with 10000 steps discarded as a burn-in. The convergence of the MCMC chains was assessed by calculating the effective sample size of the means, which was always > 85000 samples, and the standard error of each estimate, which was always $< 5 \cdot 10^{-5}$, for all cell types, and conditions. Hence, we obtain the posterior probability distribution function of the mean, underlying our observations, i.e. $P(\mu|\text{observation})$. Computing the same probability for our observed values of neuronal synchrony while awake or under each anesthetic, we computed the probability distribution function of $P(\mu_{anesthetized}\text{-}\mu_{awake}|\text{observations})$ (Figure S8B), which characterizes the most probable values of the difference in the neuronal synchrony between anesthesia and awake for each investigated cortical cell type.

Neuron, Volume *110*

Supplemental information

General anesthesia globally synchronizes activity selectively in layer 5 cortical pyramidal neurons

Arjun Bharioke, Martin Munz, Alexandra Brignall, Georg Kosche, Max Ferdinand Eizinger, Nicole Ledergerber, Daniel Hillier, Brigitte Gross-Scherf, Karl-Klaus Conzelmann, Emilie Macé, and Botond Roska

Inventory of Supplemental Information

Supplemental Figures S1 – S15

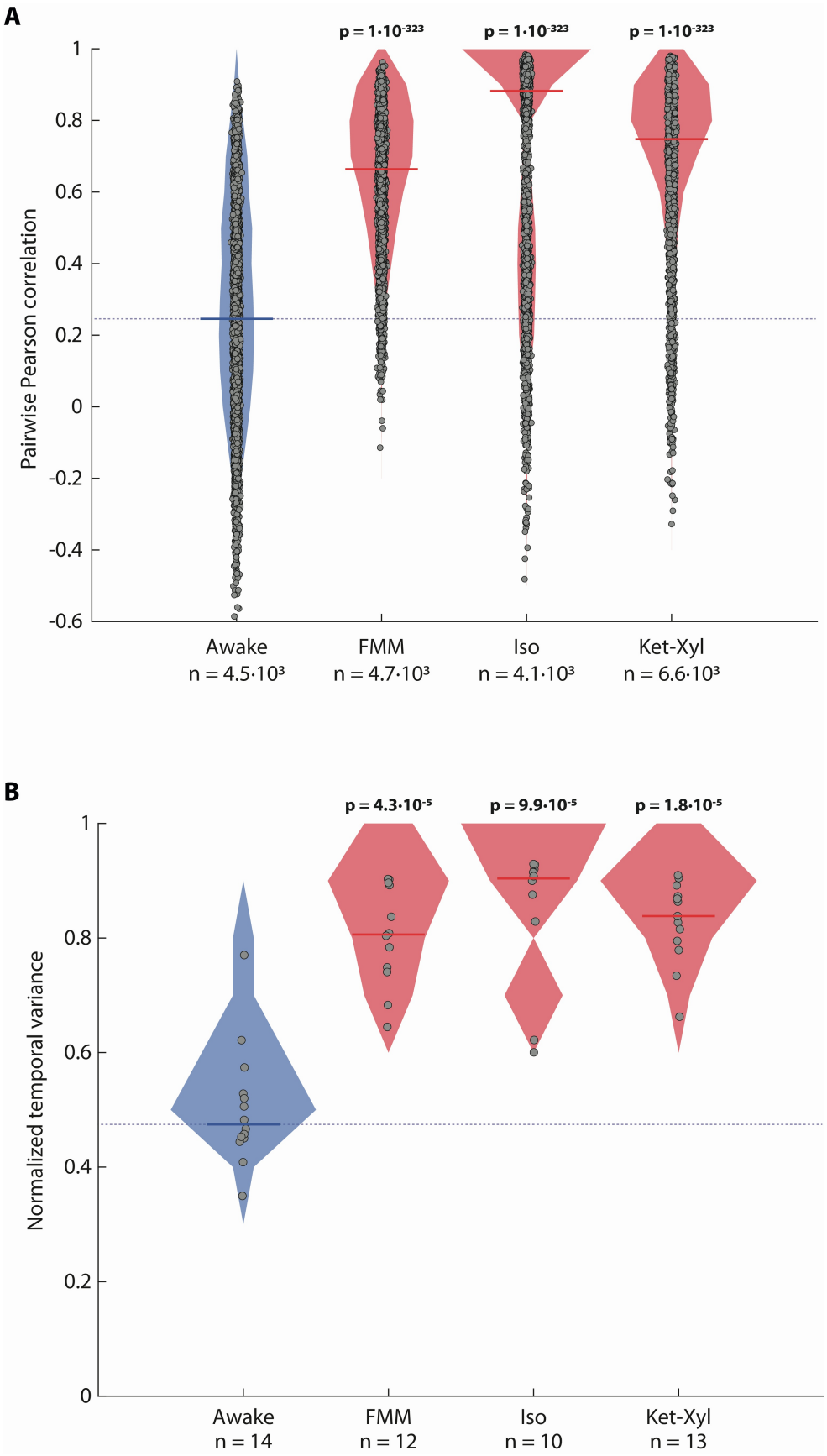
A
p = 1·10-323
p = 1·10-323
p = 1·10-323
Pairwise Pearson correlation
1
0.8
0.6
0.4
0.2
0
-0.2
-0.4
-0.6
Awake
n = 4.5·10³
FMM
n = 4.7·10³
Iso
n = 4.1·10³
Ket-Xyl
n = 6.6·10³
B
p = 4.3·10-5
p = 9.9·10-5
p = 1.8·10-5
Normalized temporal variance
1
0.8
0.6
0.4
0.2
0
Awake
n = 14
FMM
n = 12
Iso
n = 10
Ket-Xyl
n = 13

Figure S1. Alternative quantifications show increased temporal synchrony in layer 5 pyramidal neurons. Related to Figure 1.

Comparison of awake mice to mice anesthetized with FMM, Iso, or Ket-Xyl using the Pearson correlation (A) and normalized temporal variance (B) (Golomb and Rinzel, 1994). (A) Pearson correlation for all pairs of cells within each recording. Filled circles: correlation coefficient for each pair of cells (n = number of pairs); solid line: median; shading: distribution; dashed line: awake median. (B) Normalized temporal variance measures the variance of the mean population activity as a fraction of the mean variance across all cells individually. Filled circles: normalized temporal variance for each recording (n = number of recordings from different imaging fields); lines and shading as in (A). (A and B) Probability: Wilcoxon rank-sum test ($P < 0.003$, prior to Bonferroni correction for 3 comparisons; bold; significant); recordings in 9 Rbp4-Cre mice while awake, and 8 Rbp4-Cre mice while anesthetized.

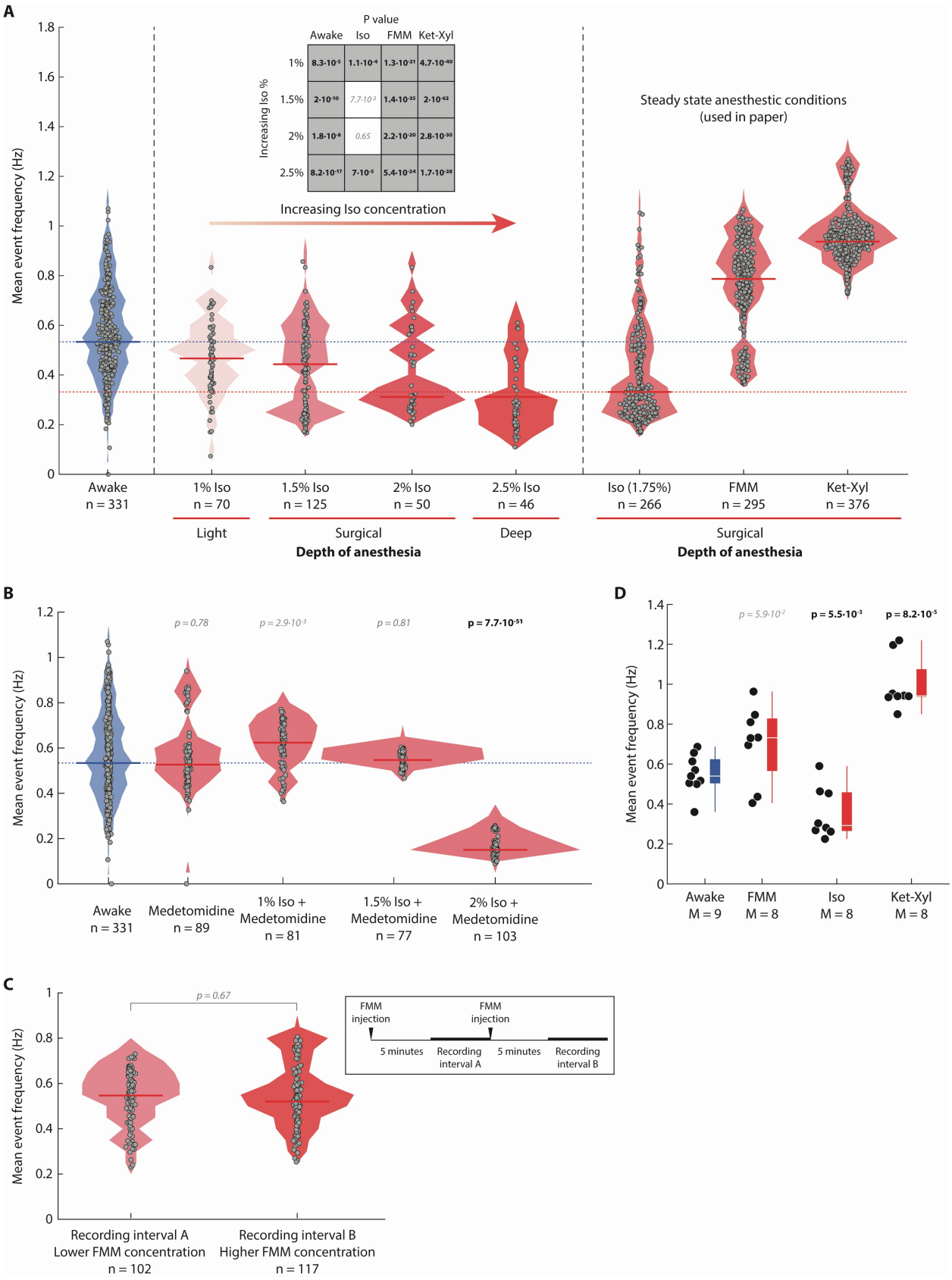
A
P value
Awake Iso FMM Ket-Xyl
1% 8.3·10⁻⁵ 1.1·10⁻⁴ 1.3·10⁻²¹ 4.7·10⁻⁴⁰
1.5% 2·10⁻¹⁰ 7.7·10⁻² 1.4·10⁻³⁵ 2·10⁻⁶²
2% 1.8·10⁻⁸ 0.65 2.2·10⁻²⁰ 2.8·10⁻³⁰
2.5% 8.2·10⁻¹⁷ 7·10⁻⁵ 5.4·10⁻²⁴ 1.7·10⁻²⁸
Increasing Iso %
Increasing Iso concentration
Steady state anesthestic conditions
(used in paper)
Mean event frequency (Hz)
Awake n = 331
1% Iso n = 70
1.5% Iso n = 125
2% Iso n = 50
2.5% Iso n = 46
Iso (1.75%) n = 266
FMM n = 295
Ket-Xyl n = 376
Light
Surgical
Deep
Surgical
Depth of anesthesia
Depth of anesthesia
B
p = 0.78
p = 2.9·10⁻³
p = 0.81
p = 7.7·10⁻⁵¹
Mean event frequency (Hz)
Awake n = 331
Medetomidine n = 89
1% Iso + Medetomidine n = 81
1.5% Iso + Medetomidine n = 77
2% Iso + Medetomidine n = 103
D
p = 5.9·10⁻²
p = 5.5·10⁻³
p = 8.2·10⁻⁵
Mean event frequency (Hz)
Awake M = 9
FMM M = 8
Iso M = 8
Ket-Xyl M = 8
C
p = 0.67
Mean event frequency (Hz)
FMM injection
FMM injection
5 minutes
Recording interval A
5 minutes
Recording interval B
Recording interval A
Lower FMM concentration
n = 102
Recording interval B
Higher FMM concentration
n = 117

Figure S2. Effect of varying concentrations of anesthetics on mean event frequency of activity in layer 5 pyramidal neurons. Related to Figure 2.

Mean event frequency for different doses of anesthetic, measured across each cell's activity trace, recorded when awake (blue) or anesthetized (red). Filled circles: mean event frequency for each cell; solid line: median; shading: distribution. (A) Layer 5 neurons show decreasing mean event frequency with increasing Iso anesthetic concentration. Mean event frequency during light (1% Iso), surgical (1.5 – 2% Iso) and deep (2.5% Iso) anesthesia was measured, and compared statistically to the frequency observed while awake, and the frequency observed while anesthetized either with steady state 1.75% Iso, FMM, or Ket-Xyl (data from Figure 2C). Increasing dosage of Iso results in the frequency decreasing from the frequency observed in awake. Independent of dose, the frequency is also significantly different from the frequency distribution observed in both FMM and Ket-Xyl. Dashed lines: median (blue: awake; red: 1.75% Iso). Probability: Wilcoxon rank-sum test ($P < 0.003$, prior to Bonferroni correction for 16 comparisons). Recordings in 9 Rbp4-Cre mice while awake, 8 Rbp4-Cre mice while anesthetized with 1.75% Iso, FMM, and Ket-Xyl, and 5 mice in each of the varying Iso conditions (1%, 1.5%, 2%, and 2.5% Iso). (B) Administering medetomidine does not result in a significant increase in the mean event frequency of activity in layer 5 pyramidal neurons, under varying concentrations of Iso anesthesia, compared to awake. Blue dashed line: awake median. Probability: Wilcoxon rank-sum test ($P < 0.003$, prior to Bonferroni correction for 4 comparisons). n = number of neurons from 9 Rbp4-Cre mice while awake, and 5 Rbp4-Cre mice in each of the medetomidine injection conditions. (C) Varying blood concentration of FMM does not result in a change in mean event frequency of activity in layer 5 pyramidal neurons. In mice already anesthetized with FMM, recordings were made in the 5 minutes prior to (Recording interval A), and 5 minutes following (Recording interval B) a second half-dose injection of FMM (inset), i.e. with higher blood concentration of FMM in Recording interval B compared to Recording interval A. Probability: Wilcoxon rank-sum test ($P < 0.003$). n = number of neurons from 5 Rbp4-Cre mice. (D) Mean event frequency measured across each cell's activity trace, recorded when awake (blue) or anesthetized (red). Filled circles: mean event frequency for all neurons recorded in one mouse; distributions shown as box (25-75 percentile) and whisker (5-95 percentile). Probability: Wilcoxon rank-sum test ($P < 0.05$, prior to Bonferroni correction for 4 comparisons); M = number of mice in each condition.

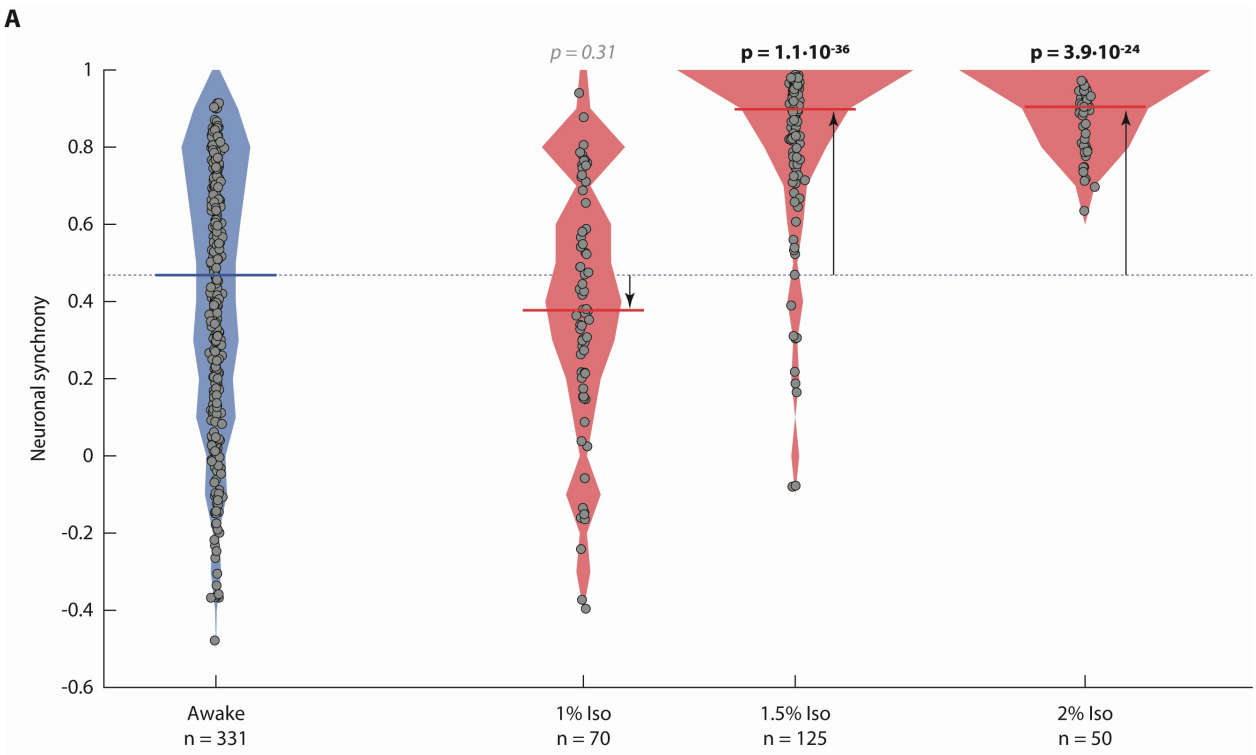
A
p = 0.31
p = 1.1·10-36
p = 3.9·10-24
Neuronal synchrony
1
0.8
0.6
0.4
0.2
0
-0.2
-0.4
-0.6
Awake
n = 331
1% Iso
n = 70
1.5% Iso
n = 125
2% Iso
n = 50

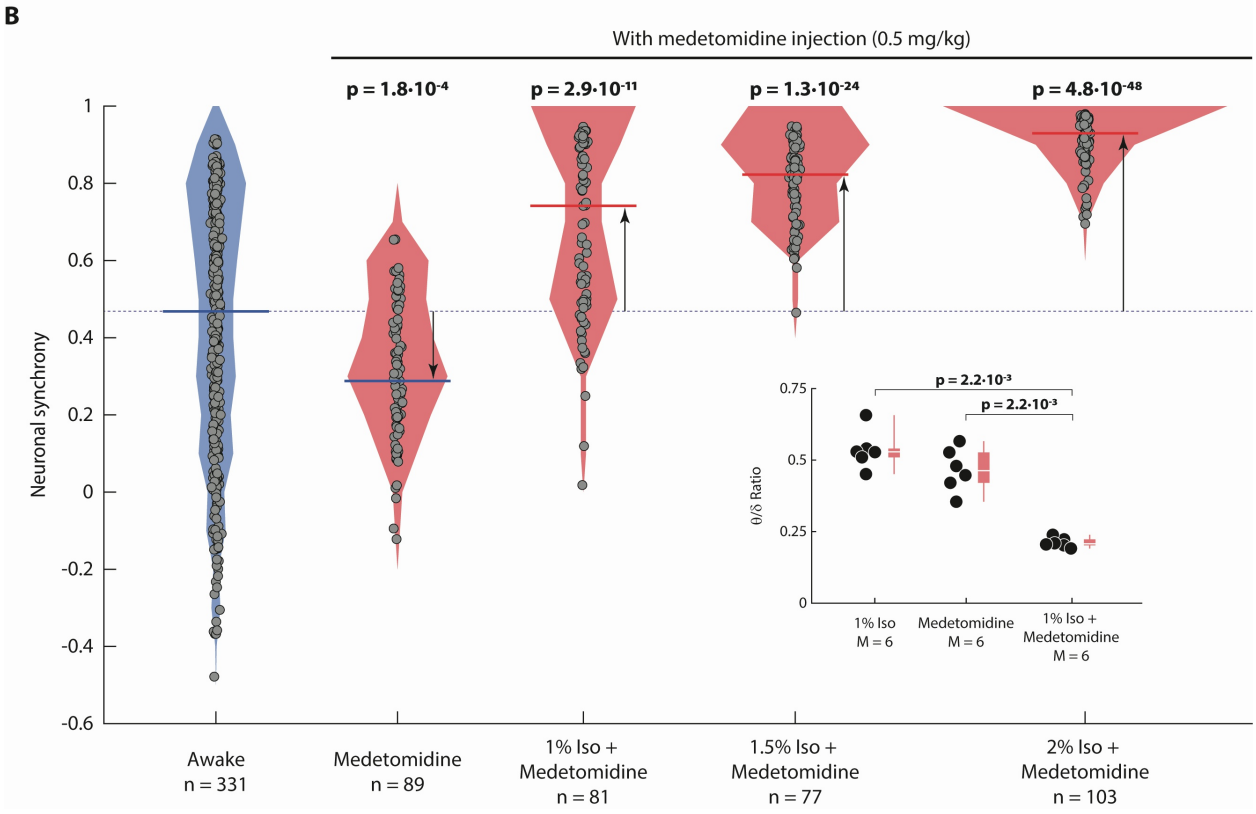
B
With medetomidine injection (0.5 mg/kg)
p = 1.8·10-4
p = 2.9·10-11
p = 1.3·10-24
p = 4.8·10-48
Neuronal synchrony
1
0.8
0.6
0.4
0.2
0
-0.2
-0.4
-0.6
p = 2.2·10-3
p = 2.2·10-3
θ/δ Ratio
0.75
0.5
0.25
0
1% Iso
M = 6
Medetomidine
M = 6
1% Iso +
Medetomidine
M = 6
Awake
n = 331
Medetomidine
n = 89
1% Iso +
Medetomidine
n = 81
1.5% Iso +
Medetomidine
n = 77
2% Iso +
Medetomidine
n = 103

Figure S3. Administering medetomidine results in an increase in neuronal synchrony at 1% Iso. Related to Figure 1.

Neuronal synchrony of layer 5 pyramidal neurons while awake or under varying concentrations of Iso anesthesia, in the absence of (A) and presence of (B) the anesthetic adjuvant, medetomidine. Filled circles: neuronal synchrony for each cell; solid line: median; shading: distribution; dashed line: awake median. (A) 1% Iso, inducing light anesthesia, does not show a significant change in neuronal synchrony from awake. Probability: Wilcoxon rank-sum test ($P < 0.003$, prior to Bonferroni correction for 3 comparisons; bold: significant; italic: not significant). (B) Administering medetomidine alone, resulting in a sedated state, does not show a significant change in neuronal synchrony from awake, while adding 1% Iso in the presence of medetomidine, which results in a surgical depth of anesthesia, results in a significant increase in neuronal synchrony from awake. Probability: Wilcoxon rank-sum test ($P < 0.003$, prior to Bonferroni correction for 4 comparisons; bold: significant). Inset: EEG spectral power for mice anesthetized with 1% Iso, injected with medetomidine alone, and anesthetized with 1% Iso following injection of medetomidine. Injecting medetomidine together with 1% Iso results in a significant decrease from both 1% Iso alone or medetomidine alone, reflecting the resulting loss of consciousness. 1% Iso alone induces light anesthesia, and medetomidine alone results in a sedated state but, in both cases, mice still display both a righting reflex and a paw withdrawal reflex (in response to a toe pinch). In contrast, 1% Iso in the presence of medetomidine results in mice that do not display both a righting reflex and a paw withdrawal reflex (in response to a toe pinch). n = number of neurons recorded in 9 Rbp-Cre mice while awake, 5 Rbp4-Cre mice in all manipulated conditions (A, B), and EEG recordings in 6 wildtype mice (inset in B).

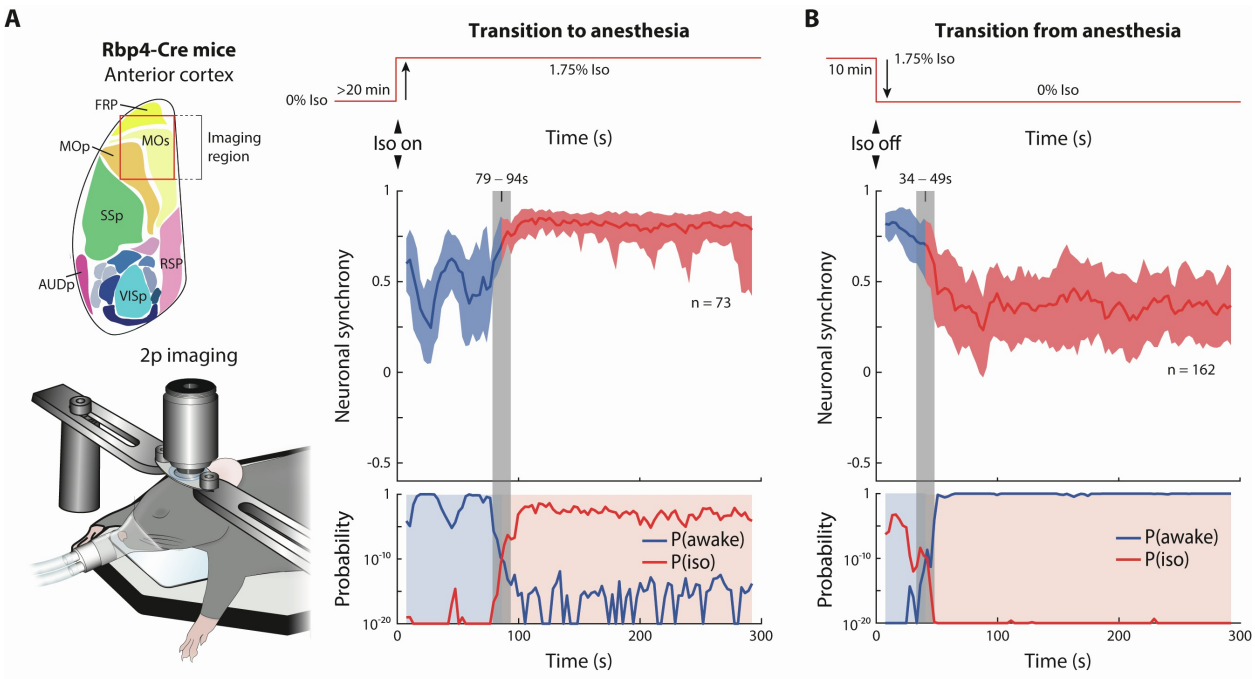

C

Transition time of neuronal synchrony

	Transition to anesthesia	Transition from anesthesia
Anterior Cortex	86.5 ± 7.5s	41.5 ± 7.5s
Posterior cortex (from Fig. 3)	82.5 ± 7.5s	39.5 ± 7.5s

Figure S4. Changes in neuronal synchrony in the anterior and posterior cortex coincide during both the transition to and from anesthesia. Related to Figure 3.

Rbp4-Cre (Gerfen et al., 2013; Gong et al., 2007) mice (expressing Cre in layer 5 pyramidal neurons throughout cortex) were injected with PHP.eB AAV (Chan et al., 2017) containing Cre-dependent GCamP7s (Dana et al., 2019), driving GCaMP expression in Cre-positive neurons. Mice were head fixed during the transition to and from anesthesia while being imaged under a two-photon microscope, in darkness. Imaging was performed in the anterior cortex (left, A). (A, B) Two-photon imaging of neuronal synchrony during transition to (A) and from Iso anesthesia (B). Upper panel: schematic of Iso anesthesia protocol. Middle panel: change in neuronal synchrony over time. Median neuronal synchrony of layer 5 neurons (shading: 25-75 percentile), computed in a rolling time window. Lower panel: probability that the observed median neuronal synchrony, in each time window, is sampled from the awake (P(awake): awake-probability curve; blue line) or the Iso (P(iso): anesthetized-probability curve; red line) distribution from Figure 1D. Blue shading when the blue line is higher than the red line; red shading when the red line is higher than the blue line. Gray vertical bar: crossing point of P(awake) and P(iso). Color of the shading in the middle panel is derived from the shaded regions in the lower panel. n = number of cells in 5 Rbp4-Cre mice (A) and 8 Rbp4-Cre mice (B). (C) Transition times of neuronal synchrony in anterior and posterior cortex, during both the transition to and from anesthesia.

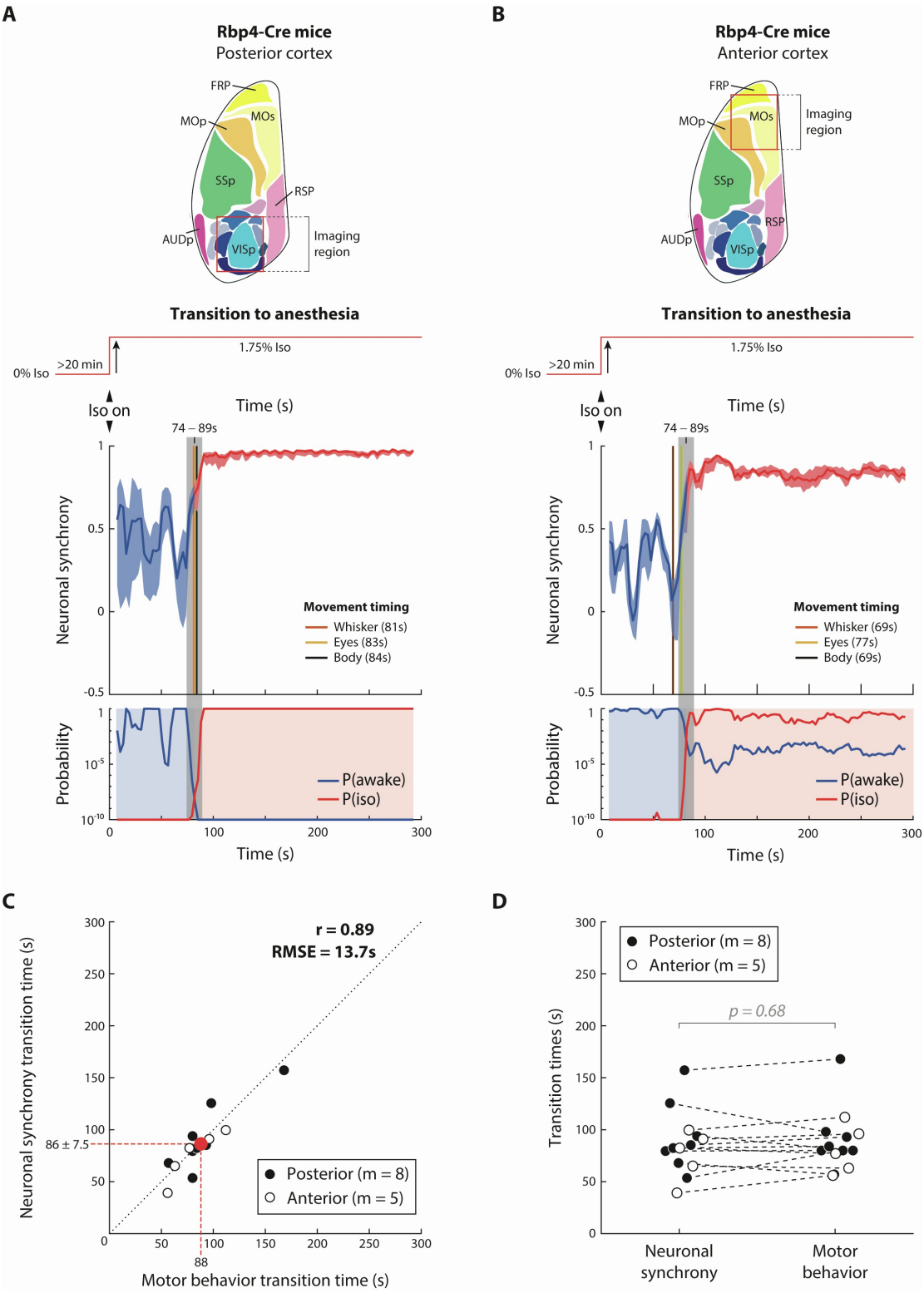
A
Rbp4-Cre mice
Posterior cortex
FRP
MOp
MOs
SSp
RSP
AUDp
VISp
Imaging region
Transition to anesthesia
0% Iso
>20 min
1.75% Iso
Iso on
Time (s)
74 – 89s
Neuronal synchrony
Movement timing
Whisker (81s)
Eyes (83s)
Body (84s)
Probability
P(awake)
P(iso)
Time (s)
B
Rbp4-Cre mice
Anterior cortex
FRP
MOp
MOs
Imaging region
SSp
RSP
AUDp
VISp
Transition to anesthesia
0% Iso
>20 min
1.75% Iso
Iso on
Time (s)
74 – 89s
Neuronal synchrony
Movement timing
Whisker (69s)
Eyes (77s)
Body (69s)
Probability
P(awake)
P(iso)
Time (s)
C
r = 0.89
RMSE = 13.7s
Neuronal synchrony transition time (s)
86 ± 7.5
88
Posterior (m = 8)
Anterior (m = 5)
Motor behavior transition time (s)
D
Posterior (m = 8)
Anterior (m = 5)
p = 0.68
Transition times (s)
Neuronal synchrony
Motor behavior

Figure S5. Changes in neuronal synchrony in the anterior and posterior cortex correlate with the termination of movement, in individual mice, during loss of consciousness. Related to Figure 3.

Rbp4-Cre (Gerfen et al., 2013; Gong et al., 2007) mice (expressing Cre in layer 5 pyramidal neurons throughout cortex) were injected with PHP.eB AAV (Chan et al., 2017) containing Cre-dependent GCamP7s (Dana et al., 2019), driving GCaMP expression in Cre-positive neurons. Mice were head fixed during the transition to anesthesia while being imaged under a two-photon microscope, in darkness, with an infrared camera to simultaneously record the termination of motor behavior. (A, B) Two-photon imaging of neuronal synchrony in two individual mice during transition to Iso anesthesia (examples for C, D). Upper panel: Imaging was performed from a window centered over either the posterior (A) or anterior cortex (B). Schematic of Iso anesthesia protocol. Middle panel: change in neuronal synchrony over time. Median neuronal synchrony of layer 5 neurons in a single mouse (shading: 25-75 percentile), computed in a rolling time window. Lower panel: probability that the observed median neuronal synchrony, in each time window, is sampled from the awake (P(awake): awake-probability curve; blue line) or the Iso (P(iso): anesthetized-probability curve; red line) distribution from Figure 1D. Blue shading when the blue line is higher than the red line; red shading when the red line is higher than the blue line. Gray vertical bar: crossing point of P(awake) and P(iso); defined as transition time of neuronal synchrony. Vertical lines: last point at which movements of the whisker (orange), eye or eyelid (yellow), and body (black) were observed (times labeled in inset). Color of the shading in the middle panel is derived from the shaded regions in the lower panel. (C) Transition time in neuronal synchrony and transition time of motor behaviors (defined as the time at which the last motor behavior was observed, during the transition to anesthesia) for 13 mice (8 mice where neuronal synchrony was recorded in the posterior cortex (as in A) and 5 mice where neuronal synchrony was recorded in the anterior cortex (as in B)). r: Pearson correlation; RSME: root mean squared error, defined as the average amplitude of difference between the transition times of neuronal synchrony and motor behavior. (D) Transition times of neuronal synchrony and motor behavior do not show a consistent difference across 13 mice. Probability: Wilcoxon signed-rank test ($P < 0.05$).

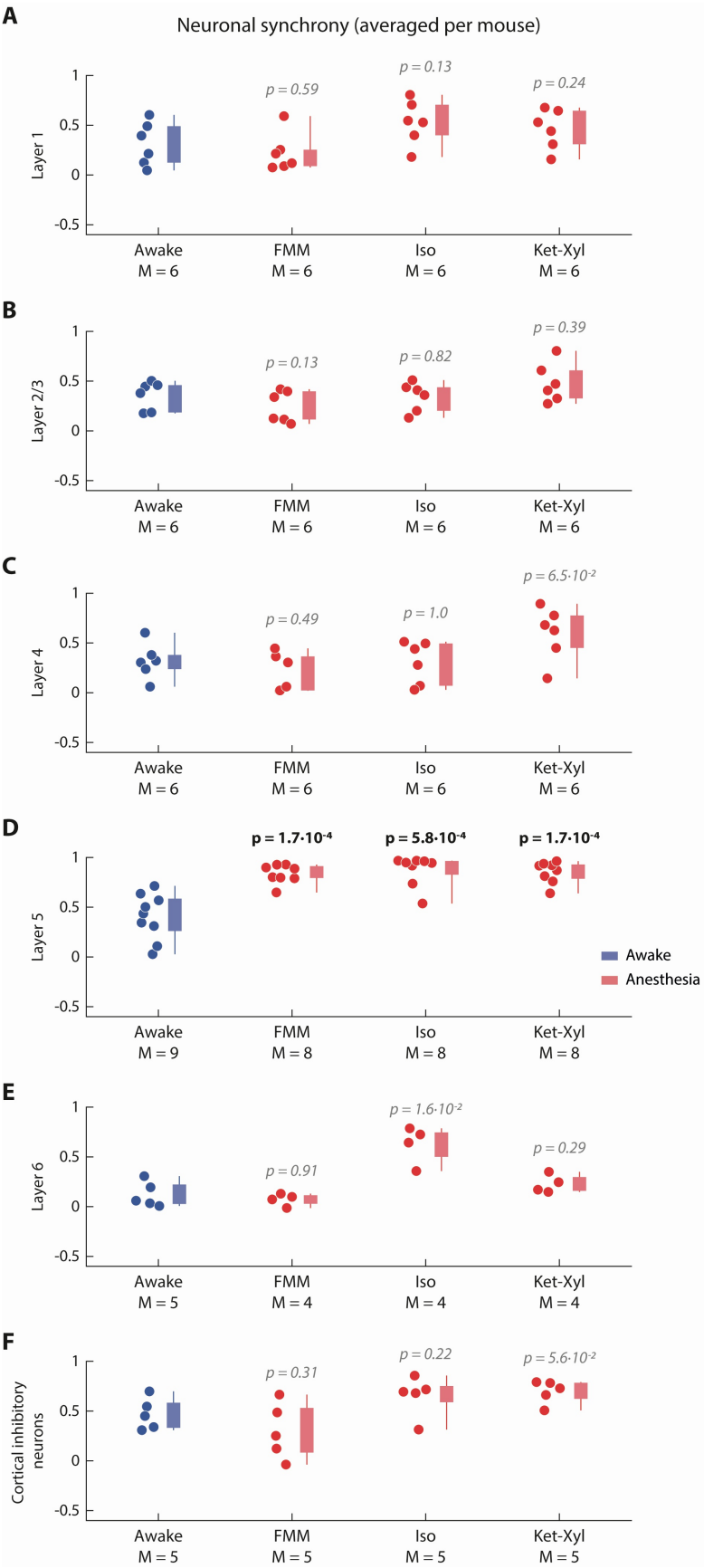
A
Neuronal synchrony (averaged per mouse)
Layer 1
p = 0.59
p = 0.13
p = 0.24
B
Layer 2/3
p = 0.13
p = 0.82
p = 0.39
C
Layer 4
p = 0.49
p = 1.0
p = 6.5·10⁻²
D
Layer 5
p = 1.7·10⁻⁴
p = 5.8·10⁻⁴
p = 1.7·10⁻⁴
Awake
Anesthesia
E
Layer 6
p = 0.91
p = 1.6·10⁻²
p = 0.29
F
Cortical inhibitory neurons
p = 0.31
p = 0.22
p = 5.6·10⁻²
1
0.5
0
-0.5
Awake M = 6
FMM M = 6
Iso M = 6
Ket-Xyl M = 6
Awake M = 9
FMM M = 8
Iso M = 8
Ket-Xyl M = 8
Awake M = 5
FMM M = 4
Iso M = 4
Ket-Xyl M = 4
Awake M = 5
FMM M = 5
Iso M = 5
Ket-Xyl M = 5

Figure S6. Only layer 5 pyramidal neurons show increased neuronal synchrony, across mice. Related to Figures 1 and 4.

Distribution of median neuronal synchrony, across mice, compared while awake (blue), and anesthetized (red) under all conditions in all investigated cell types: Layer 1 (A), Layer 2/3 (B), Layer 4 (C), Layer 5 (D), Layer 6 (E), and in cortical inhibitory neurons (F). Filled circles: median of the neuronal synchrony for all neurons recorded in one mouse; distributions shown as box (25-75 percentile) and whisker (5-95 percentile). Probability: Wilcoxon rank-sum test ($P < 0.05$, prior to Bonferroni correction for 18 comparisons); M = number of mice in each condition.

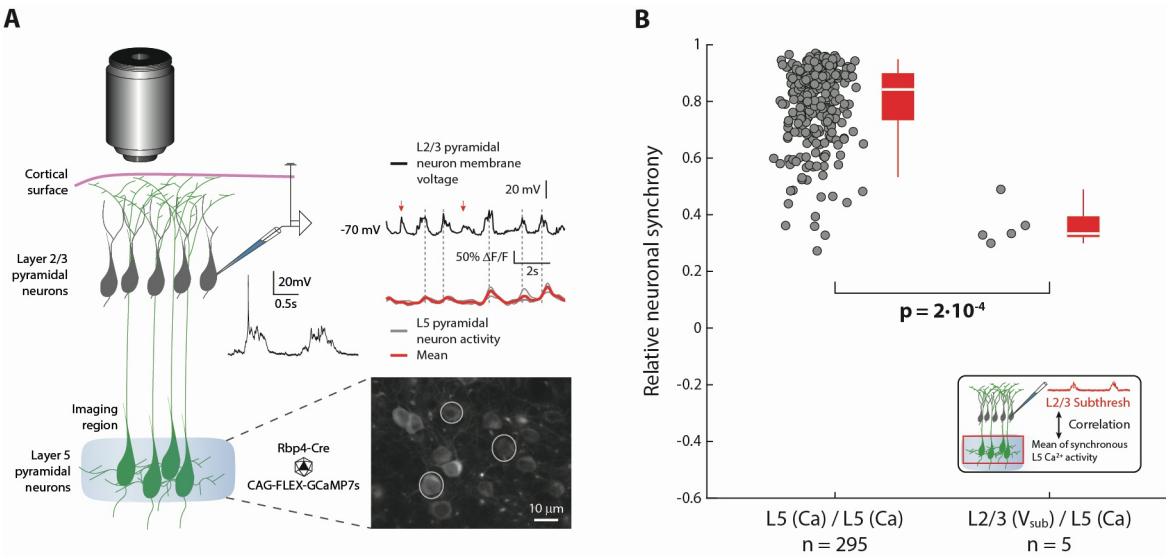

Figure S7. Simultaneous patch clamp recordings from layer 2/3 pyramidal neurons and imaging from layer 5 pyramidal neurons. Related to Figure 4.

(A) Left: Experimental design. Rbp4-Cre mice (Gerfen et al., 2013; Gong et al., 2007) were injected with PHP.eB AAV-CAG-FLEX-GCaMP7s (Chan et al., 2017; Dana et al., 2019), driving GCaMP expression in layer 5 pyramidal neurons. Simultaneous patch-clamp recordings of layer 2/3 pyramidal neuron somas and two-photon imaging from GCaMP-expressing layer 5 pyramidal neurons' somas was performed under FMM anesthesia, in head-fixed mice, in darkness. Example voltage recording of a spike and associated subthreshold membrane voltage, from a layer 2/3 pyramidal neuron is shown. See also Figure S14. Right: Imaging field of view showing GCaMP7s-expressing Rbp4-Cre neurons (bottom). The activity (gray lines) of three example neurons (gray ellipses) and their mean (red) is compared to subthreshold membrane voltage (black line) of a layer 2/3 pyramidal neuron recorded simultaneously. Events in the layer 2/3 voltage recording either correspond to events in mean layer 5 neuronal activity (gray dashed lines marking the maximum voltage recorded in each event) or show no corresponding event in mean layer 5 neuronal activity (red arrows). (B) Neuronal synchrony measured within layer 5 pyramidal neurons (data from Figure 1D), is significantly higher than relative synchrony between layer 2/3 and layer 5 neurons, defined as the correlation between the subthreshold voltage of individual layer 2/3 pyramidal neurons (L2/3 (V_{sub})) and the mean activity across layer 5 neurons (L5 (Ca)) (diagrammed in inset, bottom right). All recordings under FMM anesthesia. Filled circles: neuronal synchrony (left) and relative synchrony (right) for each cell (distributions shown as box (25-75 percentile) and whisker (5-95 percentile); white line: median). Inset: red line: subthreshold voltage from layer 2/3 pyramidal neuron; red box: imaged layer 5 pyramidal neurons providing mean activity for correlation; blue shading: imaging region. n = number of neurons (calcium imaging or patch clamp recordings). Probability: Wilcoxon rank-sum test ($P < 0.003$; bold: significant). Two photon imaging of layer 5 pyramidal neurons only from 8 Rbp4-Cre mice; simultaneous two photon imaging of layer 5 pyramidal neurons and electrophysiological recordings from 5 layer 2/3 pyramidal neurons in 3 Rbp4-Cre mice.

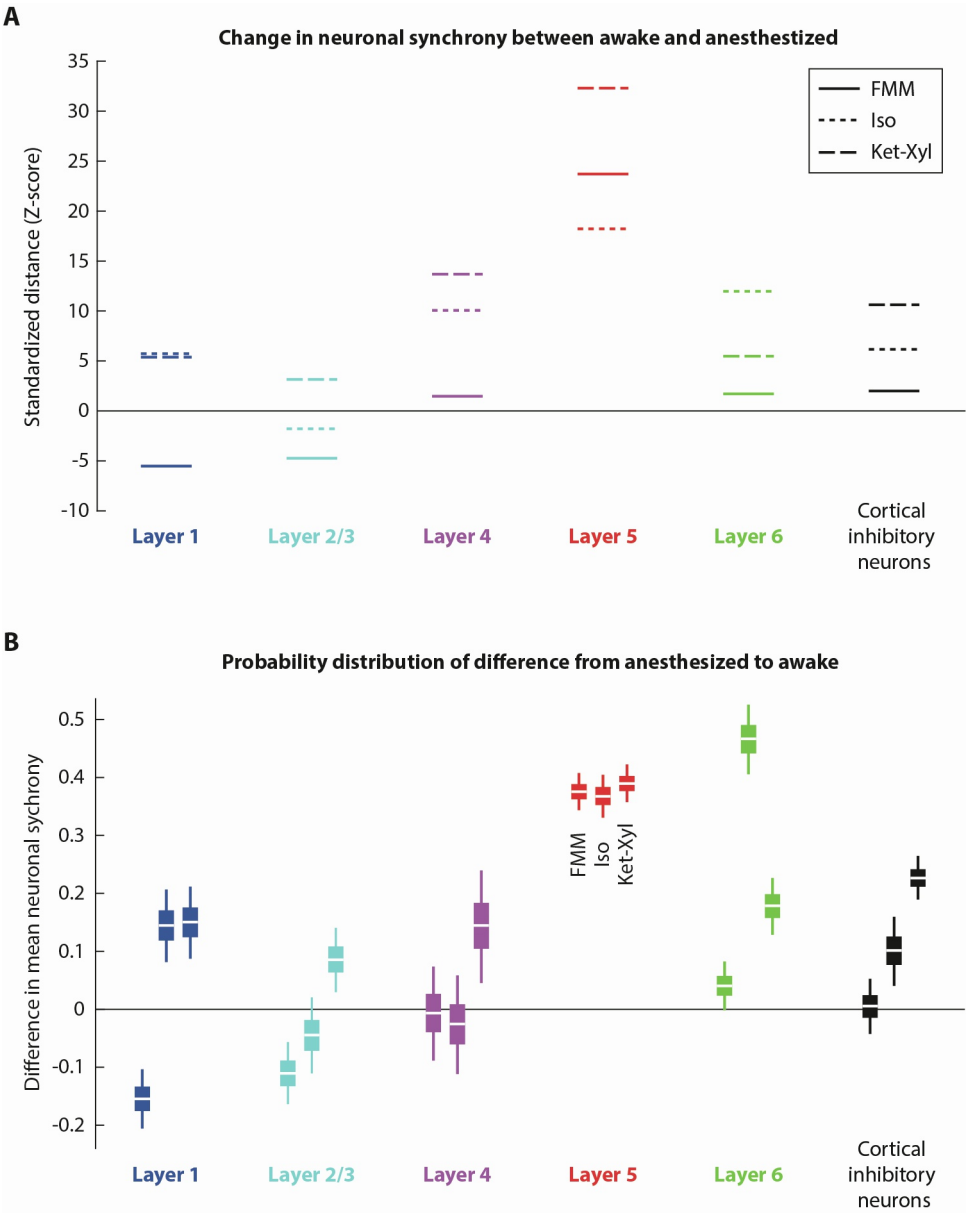

Figure S8. Layer 5 pyramidal neurons show the greatest standardized distance of neuronal synchrony between each anesthetized condition and awake, and are the only cell type to show a consistent increase in neuronal synchrony. Related to Figure 4.

(A) Standardized distance, between each anesthetic condition (FMM, Iso, or Ket-Xyl) and awake, of observed neuronal synchrony (data from Figure 1D and 4), measured as the probability that each anesthetic distribution is sampled from a combined distribution (combination of synchrony under each anesthetic and awake), as estimated using Monte Carlo sampling. Standardized distances are defined as the number of standard deviations above the mean (Z-score) for the observed distribution in each anesthetized condition. (B) Given the observed values of neuronal synchrony for each investigated cell type (data from Figure 1D and 4), Bayesian estimation is used to generate the probability distribution of the difference between the mean neuronal synchrony during each anesthetized condition and awake (distributions shown as box (25-75 percentile) and whisker (5-95 percentile); line: median).

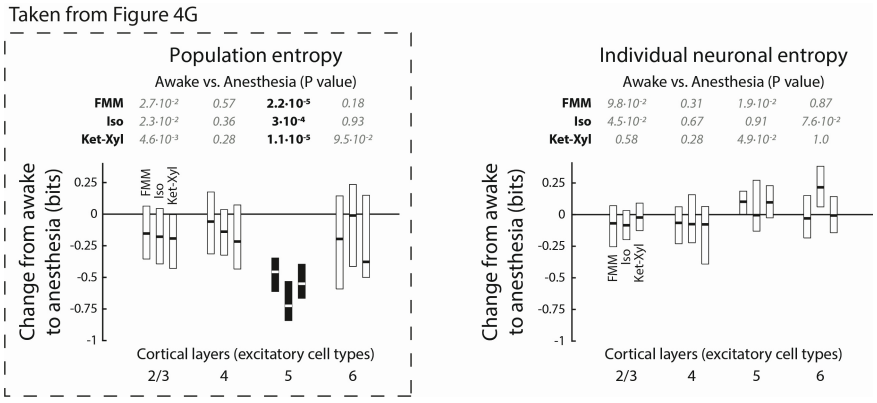

Figure S9. Changes in neuronal entropy during anesthesia compared to awake. Related to Figure 4.

Left: Change in population entropy in each anesthetized condition compared to awake (taken from Figure 4G). The information entropy of spontaneous activity within each recorded population of neurons (in each investigated excitatory cell type) averaged across bins of time. Right: Change in individual neuronal entropy in each anesthetized condition compared to awake. Information entropy of spontaneous activity within individual neurons, averaged across all neurons (within each investigated excitatory cell type). Probability: Wilcoxon rank-sum test ($P < 0.05$, prior to Bonferroni correction for 12 comparisons; black shading: significant; white shading: not significant).

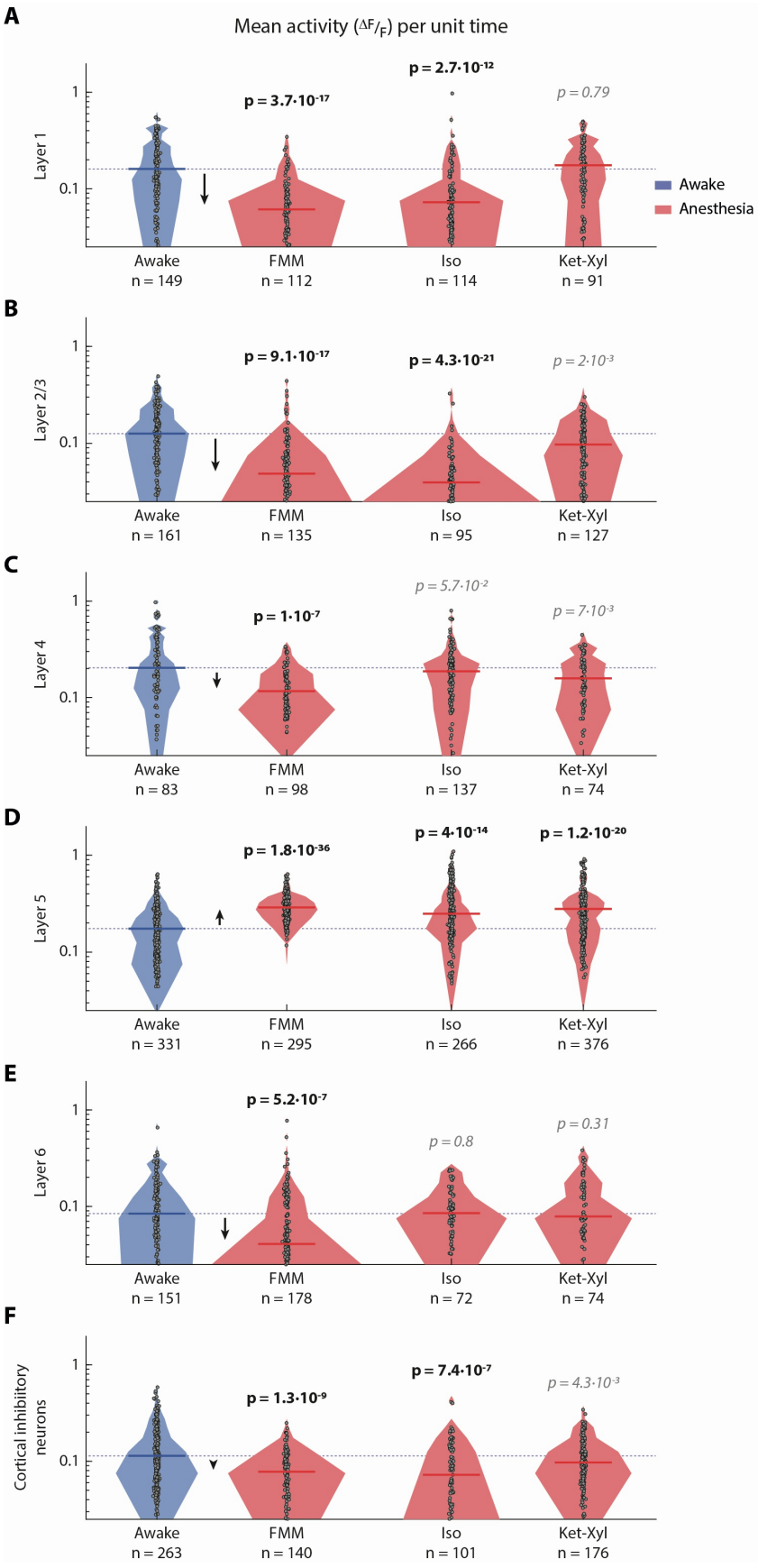
A
Mean activity (ΔF/F) per unit time
Layer 1
p = 3.7·10-17
p = 2.7·10-12
p = 0.79
Awake
Anesthesia
Awake n = 149
FMM n = 112
Iso n = 114
Ket-Xyl n = 91
B
Layer 2/3
p = 9.1·10-17
p = 4.3·10-21
p = 2·10-3
Awake n = 161
FMM n = 135
Iso n = 95
Ket-Xyl n = 127
C
Layer 4
p = 1·10-7
p = 5.7·10-2
p = 7·10-3
Awake n = 83
FMM n = 98
Iso n = 137
Ket-Xyl n = 74
D
Layer 5
p = 1.8·10-36
p = 4·10-14
p = 1.2·10-20
Awake n = 331
FMM n = 295
Iso n = 266
Ket-Xyl n = 376
E
Layer 6
p = 5.2·10-7
p = 0.8
p = 0.31
Awake n = 151
FMM n = 178
Iso n = 72
Ket-Xyl n = 74
F
Cortical inhibitory neurons
p = 1.3·10-9
p = 7.4·10-7
p = 4.3·10-3
Awake n = 263
FMM n = 140
Iso n = 101
Ket-Xyl n = 176

Figure S10. Average spontaneous activity across cortical cell types. Related to Figure 4.

(A–F) Distribution of average activity (amplitude of spontaneous activity averaged across the recording interval) in individual cells from layer 1 (A), layer 2/3 (B), layer 4 (C), layer 5 (D), layer 6 (E), and in cortical inhibitory neurons (F), while awake (blue) or anesthetized (red) with FMM, Iso, or Ket-Xyl. Filled circles: mean event amplitude for each cell (n = number of neurons); solid line: median; shading: distribution; dashed line: awake median. Probability: Wilcoxon rank-sum test ($P < 0.003$, prior to Bonferroni correction for 18 comparisons). n = number of neurons; recordings in layer 1: 6 mice; layer 2/3: 6 mice; layer 4: 6 mice; layer 5: 9 mice while awake, and 8 mice in all anesthetic conditions; layer 6: 5 mice while awake, and 4 mice in all anesthetic conditions; cortical inhibitory neurons: 5 mice.

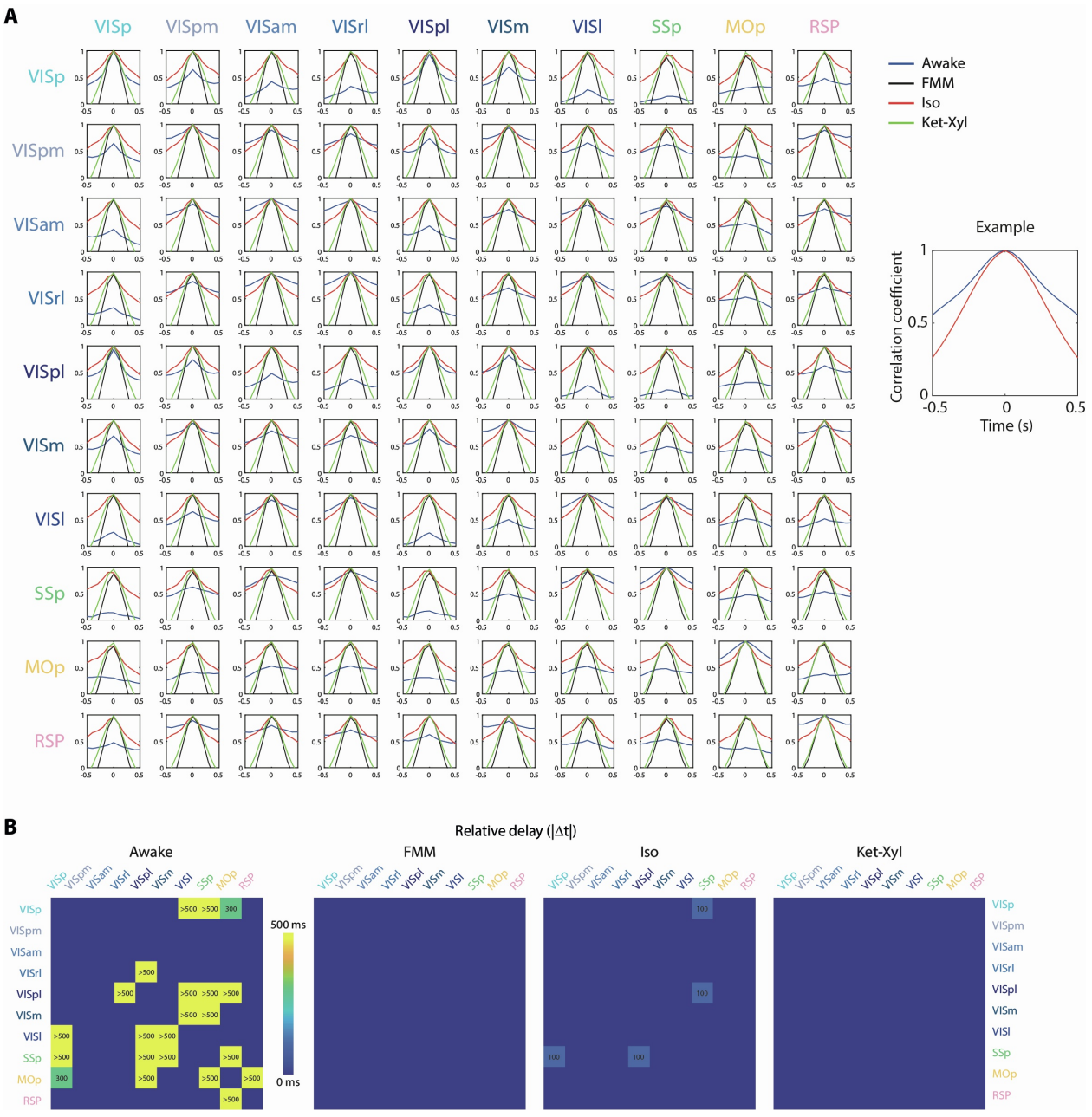

Figure S11. Relative delay between cortical areas. Related to Figure 6.

(A) Cross-correlation between pairs of cortical areas when awake (blue) or anesthetized under FMM (black), Iso (red), and Ket-Xyl (green) (VIS: visual areas; VISp: primary; VISpm: posteromedial; VISam: anteromedial; VISrl: rostrolateral; VISpl: posterolateral; VISm: medial; VISl: lateral; SSp: primary somatosensory area; MOp: primary motor area; RSP: retrosplenial area). Each comparison is labeled as in the example (right). (B) Relative delay (colored by amplitude; non-zero values labeled in ms, up to 500 ms; unlabeled values are all 0 ms) between cortical areas while awake and anesthetized under each anesthetic.

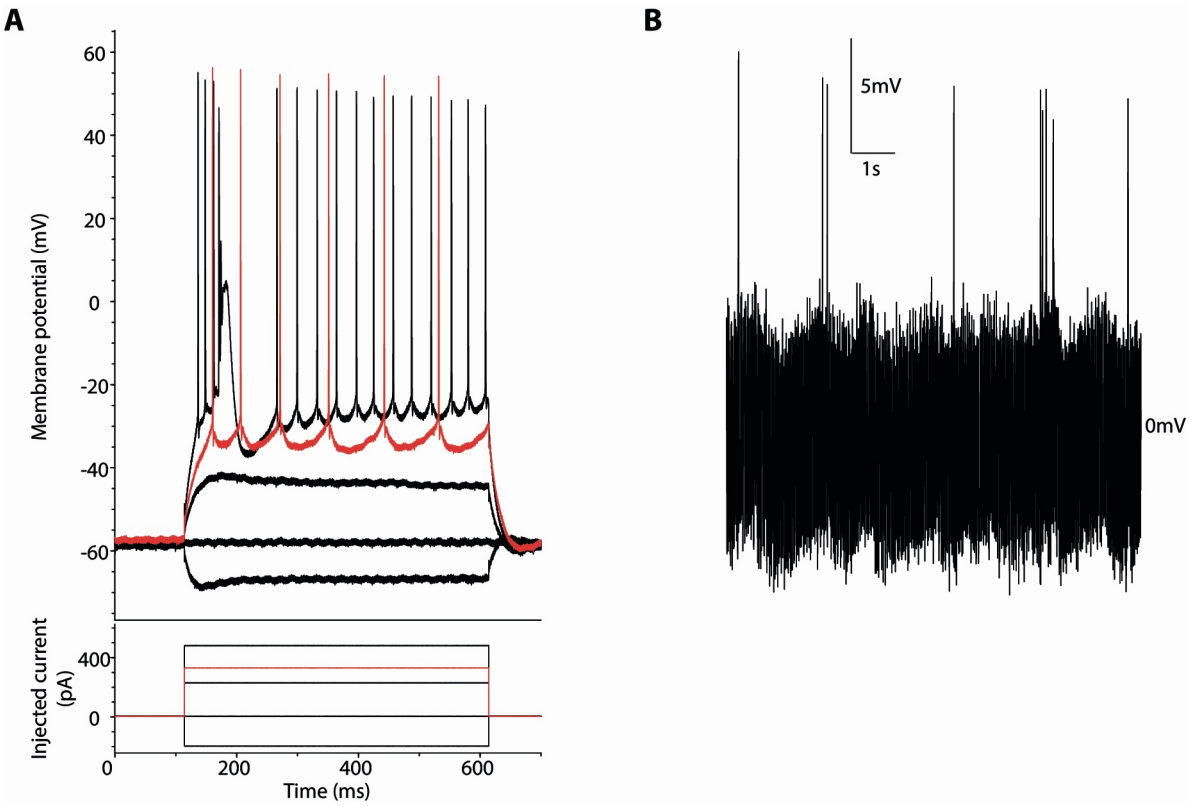

Figure S12. Layer 5 neurons spike under FMM anesthesia. Related to Figure 7.

(A**)** Two photon targeted patch clamp recording of an Rbp4-Cre positive neuron in a head-fixed mouse under anesthesia. Rbp4-Cre (Gerfen et al., 2013; Gong et al., 2007) mouse was injected with PHP.eB AAV-CAG-FLEX-GCaMP7s (Chan et al., 2017; Dana et al., 2019), driving GCaMP expression in layer 5 pyramidal neurons. Membrane potential recorded (top) for increasing current injections (bottom). (B) Targeted juxtacellular recording of GCaMP7s-expressing layer 5 pyramidal neuron shows spontaneous bursts of spikes.

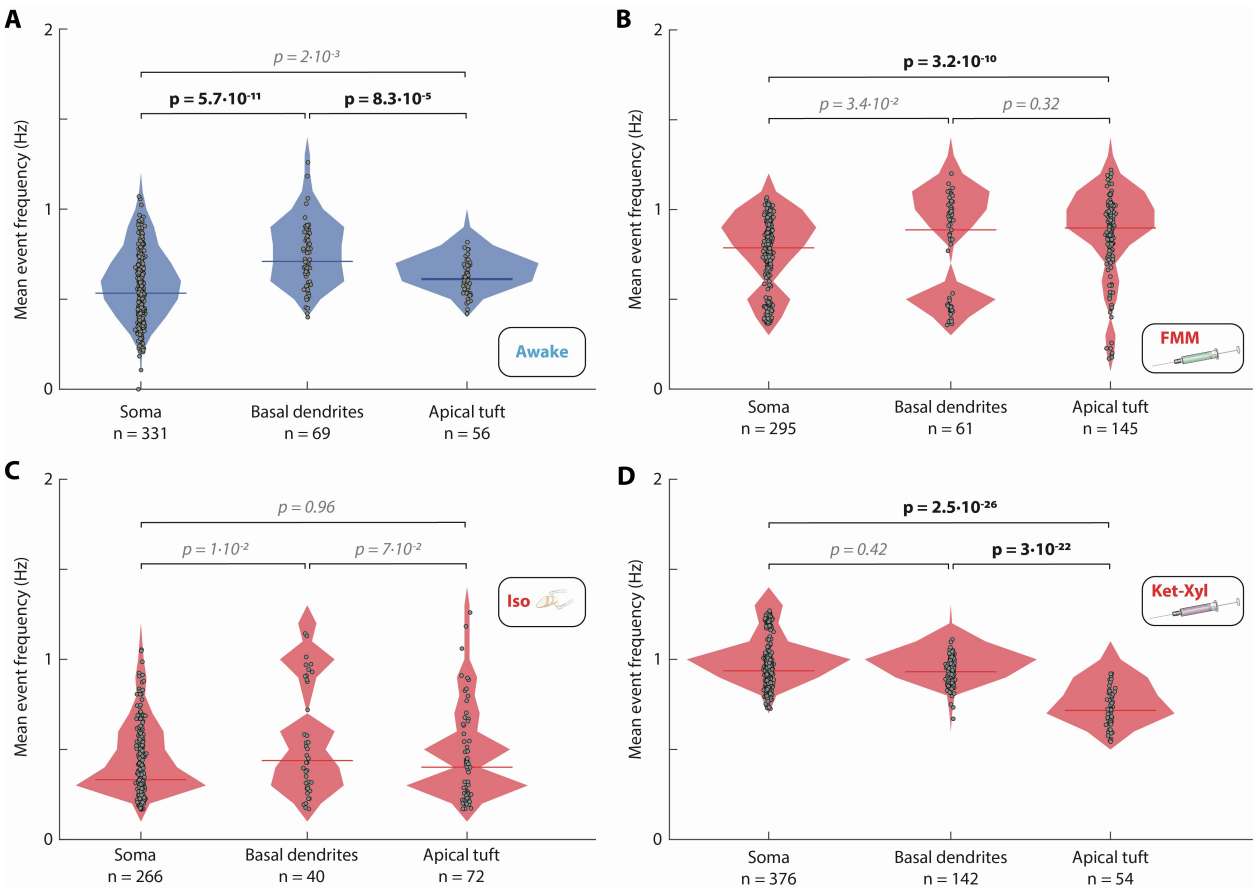

Figure S13. Mean event frequency within somas, basal dendrites, and apical tufts of layer 5 pyramidal neurons while awake and under all three anesthetics. Related to Figure 7.

(A – D) Mean event frequencies were computed from spontaneous calcium activity in each recorded compartment while awake (blue) (A) and anesthetized (red) with FMM (B), Iso (C), and Ket-Xyl (D). Filled circles: mean event frequency across compartments (n = number of compartments); solid line: median; shading: distribution. Probability: Wilcoxon rank-sum test ($P < 0.003$, prior to Bonferroni correction for 12 comparisons); recordings from 9 Rbp4-Cre mice while awake, and 8 Rbp4-Cre mice while anesthetized.

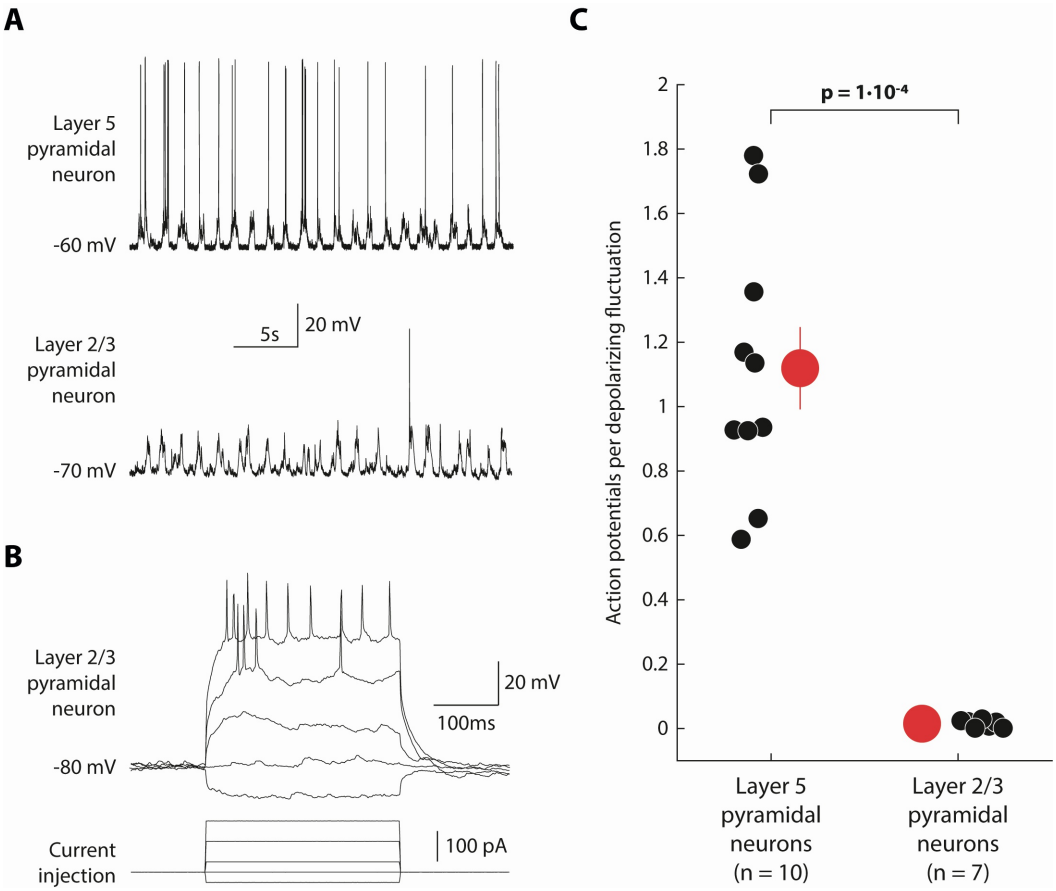

Figure S14. Average number of spikes per subthreshold fluctuation of membrane voltage in layer 5 compared to layer 2/3 pyramidal neurons, under FMM anesthesia. Related to Figure 8.

Rbp4-Cre (Gerfen et al., 2013; Gong et al., 2007) mice were injected with PHP.eB AAV-CAG-FLEX-GCaMP7s (Chan et al., 2017; Dana et al., 2019), driving GCaMP expression in layer 5 pyramidal neurons. (A) Patch clamp recordings in current clamp mode from a layer 5 pyramidal neuron (GCaMP-positive) and a layer 2/3 pyramidal neuron in a head-fixed mouse under FMM anesthesia (examples for C). (B) Membrane potential recorded (top) for increasing current injections (bottom) for a layer 2/3 pyramidal neuron. (C) Number of action potentials averaged per subthreshold fluctuation of membrane voltage is quantified for layer 5 pyramidal neurons and layer 2/3 pyramidal neurons. Layer 5 pyramidal neurons show significantly greater action potentials per subthreshold fluctuation than layer 2/3 neurons, during FMM anesthesia. Probability: Wilcoxon rank sum test ($P < 0.003$). n = number of recordings from 5 cells in 3 Rbp4-Cre mice (layer 5 pyramidal neurons), and 7 cells in 3 Rbp4-Cre mice (layer 2/3 pyramidal neurons).

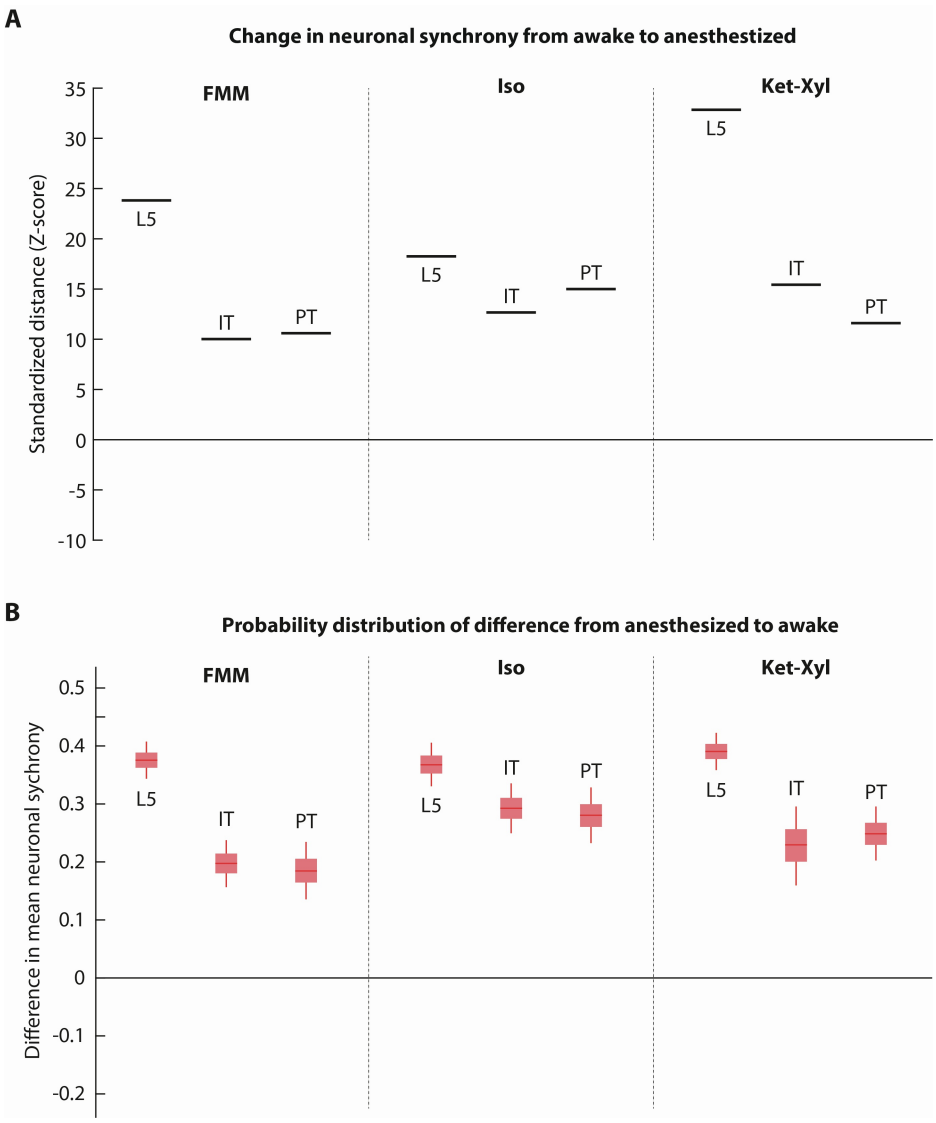

Figure S15. Differences in neuronal synchrony across all layer 5 pyramidal neurons and in layer 5 IT and PT subtypes. Related to Figure 8.

(A) Standardized distance, between each anesthetic condition and awake, of observed neuronal synchrony (data from Figure 1D and 8B, C), measured as the probability that each anesthetic distribution is sampled from a combined distribution (combination of synchrony under each anesthetic and awake), as estimated using Monte Carlo sampling. Standardized distances are defined as the number of standard deviations above the mean (Z-score) for the observed distribution in each anesthetized condition. (B) Difference between each anesthetized condition and awake, in the mean observed neuronal synchrony (data from Figure 1D and 8B, C). Bayesian estimation is used to generate the probability distribution of the difference (distributions shown as box (25-75 percentile) and whisker (5-95 percentile); line: median).